ABSTRACT

Title of Dissertation:	EXPERIMENTAL CHARACTERIZATION AND MODELING OF FLAME HEAT FEEDBACK AND OXIDATIVE PYROLYSIS FOR SIMULATION OF BENCH SCALE FIRE TESTS
	Conor Graham McCoy, Doctor of Philosophy, 2021
Dissertation directed by:	Professor, Stanislav Stoliarov, Mechanical Engineering

Two important bench scale fire tests, the cone calorimeter test and UL-94V, were characterized experimentally to allow for predictions using a numerical pyrolysis solver, ThermaKin2Ds with pyrolysis parameter sets. Flame heat feedback was measured in cone calorimeter tests for several polymers to develop a generalized flame model. Flame heat flux was measured in the center and near one side and was found to be 11–23 kW m^{-2} and 32–49 kW m^{-2}, respectively. Based on the difference in measured heat flux, a center zone and a side zone were defined and separate models developed. The final model was an area-weighted combination of the center and side zone simulations. Heat release rate data were predicted well by the final model. Ignition times for low irradiation were not predicted well initially but a correction was made to account for the effect of oxygen. The UL-94V test required characterization of the flame heat feedback but also of the burner flame (temperature, heat flux, and oxygen content). UL-94V tests were performed using polymers of different flammability

ratings to evaluate the model; some samples had insulated sides to investigate edge effects. Additional UL-94V tests performed with an embedded heat flux gauge served to measure polymer flame heat feedback. All UL-94V tests were recorded on video using a 900-nm narrow-band filter to focus on emissions from soot for tracking flame length over time. Flame heat fluxes of insulated PMMA samples confirmed a previously developed wall flame submodel, while non-insulated PMMA samples had significantly greater heat fluxes; the wall flame submodel was scaled accordingly. Burner flame oxygen content was measured to be about 5 vol% and was found to enhance decomposition of two materials; oxidation submodels were then developed accordingly. Overall, the model predicted flame spread on insulated UL-94V samples reasonably well but significantly underpredicted the results on non-insulated samples. Discrepancies were attributed to burning and spread on the edges which were not modeled explicitly. Finally, given the importance of oxidation on predictions of ignition time, oxidative pyrolysis was studied both in mg-scale and gram-scale pyrolysis experiments. Kinetic parameters were first developed based on inverse analysis of TGA tests in atmospheres of varied oxygen content. Two models were developed: a surface reaction model and a volumetric model. Mass flux data from gram-scale gasification tests were used to evaluate the models. The anaerobic model gave the best predictions of mass flux for 15 kW m^{-2} gasification tests, but the oxidative models gave better predictions for the 25 kW m^{-2} gasification tests. The volumetric model gives better predictions unless mass transport of oxygen is considered in which case, the surface model gives better predictions.

EXPERIMENTAL CHARACTERIZATION AND MODELING OF FLAME HEAT FEEDBACK AND OXIDATIVE PYROLYSIS FOR SIMULATION OF BENCH SCALE FIRE TESTS

by

Conor G. McCoy

Dissertation submitted to the Faculty of the Graduate School of the
University of Maryland, College Park, in partial fulfillment
of the requirements for the degree of
Doctor of Philosophy
2021

Advisory Committee:
Professor Stanislav I. Stoliarov, Chair
Professor Mohamad Al-Sheikhly, Dean's Representative
Dr. Richard E. Lyon
Professor Arnaud Trouvé
Professor Bao Yang

Acknowledgements

Although only my name is on this document, there are several people who have made it possible for me to do this. Mom, Dad, Evan, thank you for your love and support to keep me sane and motivated. Especially for listening to me when things were difficult. Thanks to Professor Al-Sheikhly, Professor Trouvé, Professor Yang, and Dr. Lyon for serving on my committee. Thanks to my many coworkers over the years: Yan, Josh, Greg, Chris, Ahmed, Lucas, Will, Hongen, Jacques, Dushyant, Isaac, Fernando for all your camaraderie and assistance. Finally, thank you, Dr. Stas, for everything. For your patience, your guidance, and for giving me the opportunity in the first place.

Table of Contents

List of Tables

List of Figures

Nomenclature

Symbols

A	pre-exponential factor [s^{-1} or kg^{-1} m^3 s^{-1} if second-order]
a	empirical coefficient for heat flux flame length expression [$cm^{1.66}$ $kW^{-0.66}$]
b	empirical constant for heat flux flame length expression [cm]
E	activation energy [J mol^{-1}]
C	pre-exponential factor for surface mass flux expression [g cm^{-2} s^{-1}]
c	heat capacity [J kg^{-1} K^{-1}]
D	activation energy for surface mass flux expression [kJ mol^{-1}]
Δh_c	heat of combustion [kJ g^{-1}]
H	heat of reaction [J kg^{-1}]
h	convective heat transfer coefficient [W m^{-2} K^{-1} or kW m^{-2} K^{-1}]
$\bar{h}$	spatially-averaged convective heat transfer coefficient [W m^{-2} K^{-1}]
h_b	heat transfer coefficient for UL-94V burner flame [kW m^{-2} K^{-1}]
h_f	heat transfer coefficient for laminar wall flame model [kW m^{-2} K^{-1}]
$h_{f,PMMA}$	heat transfer coefficient for PMMA flame on UL-94V sample [kW m^{-2} K^{-1}]
I_0	incident heat flux [W m^{-2}]
I_{ex}	radiant flux from an external source [W m^{-2}]
I_{rr}	re-radiated radiant flux [W m^{-2}]
I_T	transmitted radiant flux [W m^{-2}]

J	transported mass flux [kg m^{-2} s^{-1}] or [g cm^{-2} s^{-1}]
k	thermal conductivity [W m^{-1} K^{-1}]
l	distance from edge of cone calorimeter sample [m]
$\dot{m}''$	mass flux [kg m^{-2} s^{-1}]
N	number of components
N_r	number of reactions
P	pressure [Pa]
Pr	Prandtl number
p	empirical power for heat flux flame length expression
R	universal gas constant [J mol^{-1} K^{-1}]
r	rate of reaction [kg m^{-3} s^{-1}]
$\frac{dQ'}{dt}$	width-normalized heat release rate [kW cm^{-1}]
q	heat flux (in ThermaKin2Ds expressions) [W m^{-2}]
q''_{cone}	irradiation of the conical heater [kW m^{-2}]
q''_{flame}	flame heat flux, specifically, the polymer flame [kW m^{-2}]
q''_{loss}	radiative and convective losses between the sample surface and surroundings [kW m^{-2}]
q''_{total}	total heat flux measured [kW m^{-2}]
q''	heat flux [kW m^{-2}]
Sc	Schmidt number
T	temperature [K]

T_{burner}	UL-94V burner flame temperature [K]
T_f	flame temperature [K]
$T_{f,adiabatic}$	adiabatic flame temperature [K]
$T_{f,max}$	maximum flame temperature [K]
$T_{f,PMMA}$	temperature of PMMA flame on UL-94V sample [K]
T_{HFG}	temperature of the water-cooled heat flux gauge sensor [K]
T_p	ignition (pyrolysis) temperature [K]
T_s	surface temperature [K]
T_∞	ambient temperature [K]
t	time [s]
t_{ig}	ignition time [s]
x	cartesian coordinate, thickness direction of a sample. [m or cm]
y	cartesian coordinate, distance from bottom of sample [cm]
y_{eff}	distance from the bottom edge of flame [cm or m]
$y_{eff,tip}$	distance from bottom edge to tip of the flame, also known as IR flame length [m or cm]
y_f	heat flux flame length [m or cm]
y_0	flame heat feedback extension parameter [cm or m]
y^*	dimensionless length scale (for the laminar wall flame model)

α	thermal diffusivity [m^2 s^{-1}]
α_f	decay factor for the laminar wall flame model due to entrainment
δ	sample thickness [m]
Δ	difference of a quantity
ε	emissivity
η	fraction of absorbed irradiation
θ	mass-based stoichiometric coefficient
K	mass-transfer coefficient [m s^{-1}]
κ	radiation absorption coefficient [m^2 kg^{-1}]
λ	gas transfer coefficient [m^2 s^{-1}]
ν	kinematic viscosity [m^2 s^{-1}]
ξ	mass concentration [kg m^{-3}]
ρ	density [kg m^{-3}]
σ	Stefan-Boltzmann constant [W m^{-2} K^{-4}]
X	volume fraction

Acronyms

ABS	Acrylonitrile butadiene styrene
AHRR	Average Heat Release Rate
CAPA	Controlled Atmospheric Pyrolysis Apparatus
DEPAL	Aluminum Diethyl Phosphinate

DSC	Differential Scanning Calorimetry
DTA	Differential Thermal Analysis
FDS	Fire Dynamic Simulator
FPA	Fire Propagation Apparatus
GF	Glass Fiber
HB	Horizontal Burning Rating (passes UL-94 HB but not UL-94V)
HIPS	High-Impact Polystyrene
HRR	Heat Release Rate
HRR_0	Unforced Heat Release Rate
LOI	Limiting Oxygen Index
MCC	Microscale Combustion Calorimetry
MLR	Mass Loss Rate
NFPA	National Fire Protection Association
NIST	National Institute of Standards and Technology
NR	No Rating (UL-94V test outcome)
OSB	Oriented strand board
PBT	Polybutylene Terephthalate
PEI	Polyetherimide
PEEK	Poly(ether ketone)
PHRR	Peak Heat Release Rate
PMMA	Poly(methyl methacrylate)
POM	Polyoxymethylene

PVC	Poly(vinyl chloride)
TGA	Thermogravimetric Analysis
TRP	Thermal Response Parameter
UL-94V	UL-94 Vertical Burning Test

Chapter 1: Introduction

1.1 Background

1.1.1 The fire problem at home and the importance of fire testing

Fires are a continuing problem. According to the latest report on Fire Loss in the United States, published by the National Fire Protection Association (NFPA), fires in 2018 resulted in over 3600 deaths, over 15,000 injuries, and about 25.6 billion dollars lost in property damage [1]. The majority of fatalities (74%) occurred in fires at home occupancies [1]. From the report, although the number of fatalities due to fire has declined dramatically since 1978 (when the NFPA began documenting fire incidents annually), the death rate (fatalities per 1000 fires) has remained approximately constant. This implies that the reduction in number of fatalities is due largely to the reduction in the overall number of fire incidents rather than reduced risk. In light of this, the NFPA has identified five strategies for reducing the risk of fatal fires: improved public education on fire safety, working smoke alarm systems and escape plans, more residential sprinklers, additional protections for high-risk groups such as children and the elderly, and materials safer from fire [1]. Although a combination of these strategies is best for minimizing life lost to fires, from a design perspective, preventing ignition

and spread of fire beyond the origin is the ideal goal. Understanding the fire hazard of a material can be complex since there are many factors to consider including: ignitability, propensity for flame spread (horizontal or vertical), heat release rate, smoke production and toxicity all comprise material flammability. To accurately quantify the fire hazard of a material requires several different fire tests which can study each of these factors. The most common fire tests include the cone calorimeter, the Fire Propagation Apparatus (FPA), the Limiting Oxygen Index (LOI) test, and the UL-94 Vertical Burning test (UL-94V). Each test shall be briefly detailed in the following sections.

1.1.2 Cone calorimeter and Fire Propagation Apparatus (FPA)

The cone calorimeter, developed at the National Bureau of Standards [2], is a prominent tool in fire research. It is capable of simultaneous measurements of mass loss rate (MLR) and heat release rate (HRR) of burning material in response to controlled, radiant heating supplied by the conical heater (made of a wound electrical heater rod). The HRR is measured based on oxygen consumption calorimetry assuming 13.1 kJ g^{-1} of heat release per gram of oxygen consumed, true for a wide variety of fuels [2]. The HRR is an important quantity in fire safety science because of its large impact on tenability time, which governs the time available for safe egress [3,4]. The

cone calorimeter has also been used to study ignition [5], emissions [6], the effects of additives [7], charring [8], as well as other burning phenomena. Accurate modeling of cone calorimeter tests is of great interest because of the potential cost savings from reduced number of tests and the ability to obtain material properties through multi-parameter optimization [9]. The fire propagation apparatus (FPA) is a test quite similar to that of the cone calorimeter with the main differences being the tungsten-quartz lamps instead of the conical heater and the ability to control the composition of the gaseous environment surrounding the sample [10]. Samples are circular, but the diameter is roughly equal to the length of the side of the square cone calorimeter samples such that sample size is effectively the same. Many of the same quantities extracted in cone calorimeter tests can also be extracted from FPA tests.

1.1.3 Limiting Oxygen Index (LOI)

The Limiting Oxygen Index (LOI) also known as the critical oxygen index, seeks to determine the minimum volumetric concentration of oxygen that sustains a flame on plastics [11]. A small plastic sample is held in a glass chimney with a carefully controlled oxygen-nitrogen atmosphere. The test entails igniting the sample at the top and recording the time until the flame extinguishes and the distance traveled on the sample by the flame. If the flame lasts longer than 180 s after ignition or travels past

50 mm, the tested concentration is considered to be flammable. If the mixture was flammable, the oxygen concentration is lowered and then tested again. If the mixture was not flammable, the oxygen concentration is increased and then tested again. This process is repeated until a pass and a fail are measured for concentrations within 1% of another. The LOI is then found by a iterative procedure described in ASTM D2863 [11]. More flammable materials tend to have lower LOI values while low flammability materials tend to have higher LOI values.

1.1.4 UL-94 Vertical Burning test (UL-94V)

The UL-94 vertical burning test (UL-94V), or equivalently ASTM D3801 [12], is arguably the most widely used method for evaluation of flammability of polymeric solids. The test entails subjecting a small polymeric bar, suspended above a bed of cotton, to a Bunsen-burner-type flame for 10 s and recording the time the sample remains aflame after removing the burner; this quantity is known as the after-flame time. Based on the recorded times and whether the cotton ignites or not due to flammable drips, ratings are assigned. The best rating, V-0, is achieved when the flame ceases within 10 s after the burner is removed and the cotton does not ignite [12]. If the flame instead ceases within 30 s, a V-1 rating is assigned. In either case, a V-2 rating is assigned if the cotton ignites [12]. Materials that do not meet these criteria are given

either no rating (NR) or are tested in the horizontal burning (HB) configuration and may earn an HB rating if they pass it. UL-94V ratings are frequently used in flammability requirements.

1.2 Literature Review

1.2.1 Motivation and overview of the literature review

This work sought to focus on the two most frequently performed fire tests: the cone calorimeter test and the UL-94V test. Given the widespread use of the cone calorimeter and UL-94V tests, a quantitative understanding of the physical and chemical phenomena that determine their outcomes is important. Greater understanding would enable predictions of the tests' dynamics through modeling. Such models could be used to relate the performance of a material in these tests to one another or potentially other fire scenarios. It could also help guide the design of fire-resistant materials, by reducing the time and materials cost of repeated fire tests. Finally, models of these tests can help better understand what exactly is being measured in these fire tests.

The literature was reviewed to better understand previous work quantifying and modeling the cone calorimeter and UL-94V tests. The review revealed that early studies focused on relating quantities or ratings of these tests to each other or to other fire tests.

Later studies sought to quantify the conditions of these tests and explicitly model them rather than correlate results. The literature was also reviewed to better understand the effect of oxygen on the pyrolysis of polymers. The impact of oxygen on pyrolysis is not usually considered when modeling fire tests because for most of the test, pyrolysis occurs in inert conditions due to the presence of a diffusion flame, preventing oxygen from reaching the pyrolyzing solid; oxygen concentration measurements on burning PMMA slabs have confirmed the absence of oxygen [13]. However, oxygen can affect pyrolysis prior to ignition and it can also affect smoldering combustion of char after flame extinction [14]. Results from this work indicated that the presence of oxygen can impact the pyrolysis of polymers in the cone calorimeter and UL-94V tests and rudimentary models were developed to account for this impact. The findings of the literature review shall be grouped into these topics.

1.2.2 Early attempts to relate cone calorimetry and UL-94V to other fire tests

Hong et al. [15] and Lyon and Janssens [16] experimentally investigated the performance of several polymers of varied UL-94V ratings in other fire tests such as the LOI and the cone calorimeter. Weil et al. [17] reviewed the literature to correlate LOI test results with the results of other fire tests including UL-94V. All three studies found that materials with better UL-94V ratings tended to have higher LOI values;

however, all three studies also found much overlap in LOI values among the UL-94V classes such that knowledge of a material's LOI did not enable prediction of the UL-94V rating. For comparative purposes, we compiled the LOI values and UL-94V ratings for several materials from the work of Hong et al. [15] and Lyon and Janssens [16] and plotted the results in Fig. 1a (V-0 and V-1 rated materials) and Fig. 1b (V-2 and HB rated materials). The plots illustrate the previous findings: The LOI values are generally higher for V-0 and V-1 materials than for V-2 and HB materials. An average LOI was found to be 37.1 vol% for V-0 and V-1 materials and 20.4 vol% for V-2 and HB materials, showing that LOI can roughly distinguish these two groups of materials. However, within these groups there is much overlap, preventing prediction of UL-94V rating from knowledge of a material's LOI.

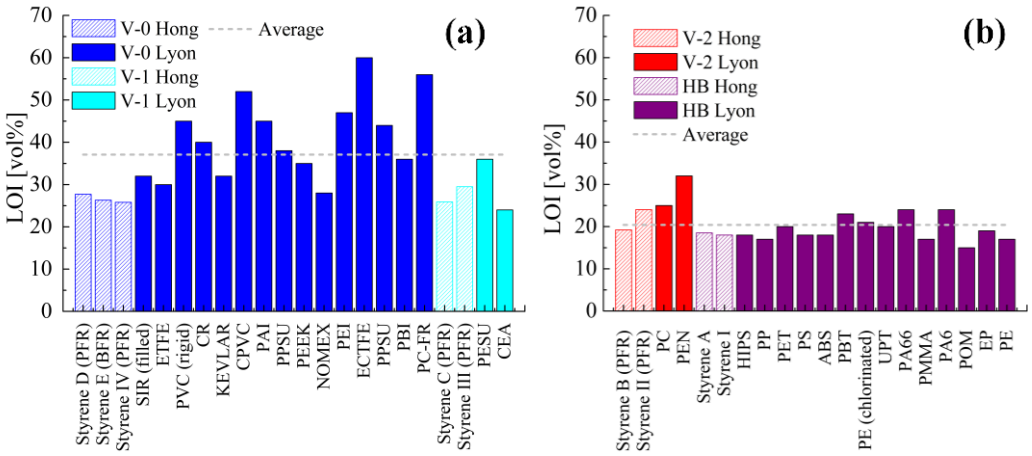

Fig. 1. Comparison of published LOI values for several polymers of different UL-94V ratings. Bars with shading correspond to data taken from Hong et al. [14] while solid bars correspond to data taken from Lyon and Janssens [16]. See [15,16] for full material names / composition.

Several studies have examined the relationship between cone calorimeter data and UL-94V ratings. Multiple exploratory properties such as time to ignition, total heat released, peak heat release rate, average heat release rate, and unforced heat release rate (HRR_0) have all been investigated for their ability to predict UL-94V ratings [15,16,18–20]. Most variables did not show any significant relationship but HRR_0 did show some correlation. HRR_0 is the theoretical heat release rate (HRR) of the material in a free-burning case (no external heat flux). HRR_0 is obtained from extrapolation of HRR data, usually the average HRR, taken at multiple incident heat fluxes. Much like the LOI, studies found overlap in HRR_0 among the UL-94V classes [16,18–20]. Multiple studies point out that physical differences such as geometry, ignition source, heat flux, and the

influence of dripping may prevent correlation between the cone calorimeter and the UL-94V test [18–20].

For comparative purposes, HRR_0 data from the study of Schartel et al. [18] and Lyon and Janssens [16] were plotted in Fig. 2a and Fig. 2b. The HRR_0 data of Morgan and Bundy [19,20] were excluded from this analysis because they used peak HRR, while the rest used average HRR. Fig. 2a and Fig. 2b support the previous findings that materials with the same HRR_0 can have significantly different UL-94V ratings, especially in the range of $90 \leq HRR_0 \leq 160$ kW m^{-2}. Fig. 2a and Fig. 2b show that HRR_0 is an accurate predictor of UL-94V rating only for the extreme cases of $HRR_0 < 50$ kW m^{-2} which corresponds to a V-0 rating for likely all materials and $HRR_0 > 150$ kW m^{-2} which corresponds to an HB rating (or worse) with few exceptions. Otherwise, there is too much overlap in ratings to predict a material's UL-94V result solely from HRR_0.

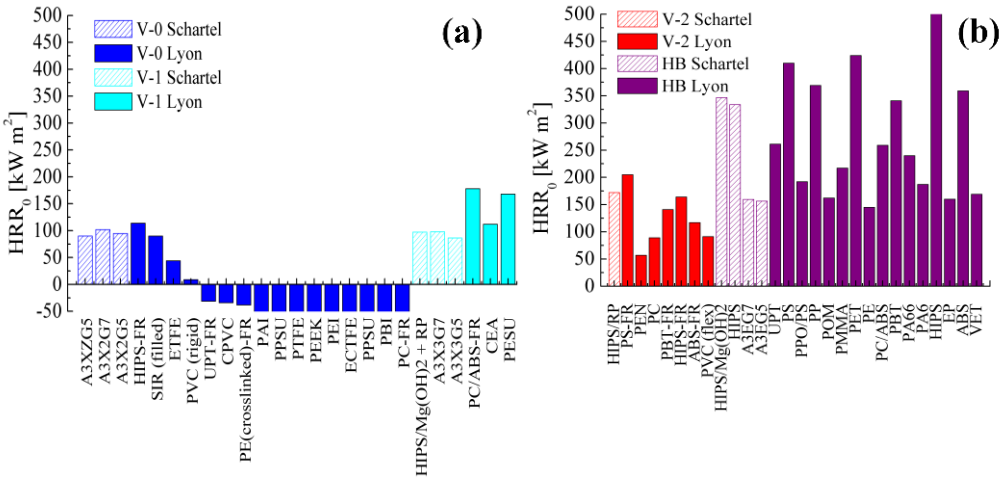

Fig. 2. Comparison of published HRR_0 values for several polymers of different UL-94V ratings. Bars with shading correspond to data taken from Schartel et al. [18] while solid bars correspond to data taken from Lyon and Janssens [16]. Fig. 2a is cut off at -50 kW m^{-2} even though some of the materials have lower HRR_0. See [16,18] for full material names / composition.

1.2.3 Quantification and modeling of cone calorimetry (or similar tests)

Early modeling of the cone calorimeter by Rhodes and Quintiere [5] concerned developing a simple thermally thick model for the transient burning rate of poly(methyl methacrylate) (PMMA) as a function of thermal transport properties and transient incoming heat flux. They recognized that flame heat feedback was critical and sought to include it in their model. Flame heat flux for PMMA was not measured directly because of the difficulties involved in direct heat flux measurements, but instead approximated to be 37 kW m^{-2} using a previously developed analytical model for the

convective flame heat flux of PMMA pool fires [21] and by calculating the flame radiative flux via an assumed temperature and computed emissivity for PMMA flame [5]. Rhodes and Quintiere subsequently extended their analysis to nylon, polyethylene, and polypropylene with estimated flame heat fluxes between 14–30 kW m^{-2} [22].

More advanced modeling efforts utilized pyrolysis models coupled with empirical models of flame heat feedback or with computational fluid dynamics (CFD) gas-phase combustion models. Concerning work with empirical flame models, Stoliarov et al. [23] conducted cone calorimetry tests on PMMA, high-impact polystyrene (HIPS), and high-density polyethylene (HDPE) for various thicknesses and various irradiation settings. In this study [23], tests were modeled using the pyrolysis solver, ThermaKin [24,25]. The interaction between the flame and the sample surface in the model was characterized by adding a 12–24 kW m^{-2} radiative heat flux source term once ignition occurs. This heat flux term was not measured directly but determined by inverse analysis wherein the flame heat flux was adjusted until it provided the best agreement between the HRR predicted by the model and the HRR data for a single thickness and a single irradiation setting (49 kW m^{-2} irradiation and 8.5 ± 0.8 mm thick samples) [23]; flame heat flux was determined for each material. The derived flame heat fluxes were then used to predict the HRR at other test conditions. The consistent performance of the model for different incident heat fluxes

and different thicknesses supported the assumption that flame heat flux is relatively independent of material thickness and irradiation. Overall, peak heat release rate (PHRR) and time to PHRR were predicted well by the simulations, but average HRR (AHRR) was not predicted well for thin samples. The same analysis was later extended to charring materials such as bisphenol A (BPA) polycarbonate and poly(vinyl chloride) (PVC), but the model used a new value for flame heat flux (15 kW m^{-2}) [26] which was an average of the flame heat flux derived in their previous work and values published in the literature [27].

Snegirev et al. [28] also employed a pyrolysis solver (Pyropolis [28]) coupled with an empirical flame model to simulate cone calorimetry of several materials: HIPS, BPA polycarbonate, and fiber-reinforced resin composite. Flame heat flux was assumed to be constant (20 kW m^{-2}) for all materials and was based on measurements reported for black PMMA [27]. Snegirev et al. sought to evaluate their model against published cone calorimeter experimental data for HIPS [23], BPA polycarbonate [26], and the composite material [29]. Overall, their model successfully predicted time to ignition, time to PHRR, and PHRR, but consistently underpredicted AHRR.

Concerning work that explicitly modeled the gas-phase flame with CFD, Linteris et al. [30] conducted simulations of black PMMA using the National Institute of Standards and Technology (NIST) Fire Dynamic Simulator (FDS) [31]. Cone

calorimeter experiments were conducted to validate the model. From the experiments, topography measurements showed that the samples do not burn uniformly over the surface, especially for lower levels of irradiation, indicating the non-uniformity in flame heat feedback across the sample [30]. Values for flame heat feedback were not reported. The simulations overpredicted the AHRR of the experiments for low irradiation and underpredicted the AHRR for high irradiation.

Kacem et al. [32] studied the burning of square PMMA slabs of 10, 20, and 40 cm side lengths. The smallest size corresponds to that of the cone calorimeter. Similar to the cone calorimeter, the sample was subjected to irradiation (40 kW m^{-2}) using a radiant panel; however, the panel was removed once ignition occurred. MLR, sample topography, and flame heat flux were recorded; HRR was not measured. Flame heat flux was measured using a water-cooled total heat flux gauge. Flame heat flux measured in the sample center for the smallest size was 19–28 kW m^{-2} [32]. Flame heat flux was also measured in a corner of a 20 cm side slab and found to be 8 kW m^{-2} smaller than the measurement in the center. Smaller flame heat flux near the sides than in the center contradicts previous findings [30], perhaps due to differences in scale. Simulations were conducted using the CFD code, ISIS, developed by ISRN [33]. The simulation for 10 cm size overpredicted the experimental burning rate except towards the end of the test.

Boyer (Boyer, 2017) conducted simulations of cone calorimetry using a pyrolysis model coupled with the CFD code, ISIS [33]. Boyer studied PMMA, HIPS, and HDPE. The pyrolysis model was an updated version of that used by Kacem et al. [32], utilizing pyrolysis parameter sets provided by Stoliarov et al. [23]. For validation, simulations were compared against cone calorimeter experimental results conducted by Stoliarov et al. [23]. Relative error in predicted AHRR was on average 17, 41, and 24% for PMMA, HIPS, and HDPE, respectively. Relative error in predicted PHRR was on average 16, 34, and 21% for PMMA, HIPS, and HDPE, respectively. Experimental uncertainty was estimated to be 17% [34]. From the simulations, radial profiles of flame heat feedback to the surface were obtained. It was also found that the flame heat flux to the center is primarily radiative, while towards the edges of the sample, the total heat flux is larger and primarily convective. Simulated flame heat fluxes suggested that flame heat flux is material-specific and average values ranged from 5–12 kW m^{-2}, lower than previous values [27,32]. These heat fluxes, however, were to a burning surface rather than a cold sensor, which could explain why the values are lower.

Galgano et al. [35] conducted simulations of PMMA burning in the cone calorimeter using a 2D (radial and axial) CFD code (Ansys FLUENT) for the gas-phase coupled with a previously derived 1D pyrolysis model [36] evaluated in MATLAB. Flame heat flux was found to vary over the surface. A net flame heat flux of 18 kW m^{-}

^{2} was reported [35], which was close to previous experimental measurements (Beaulieu & Dembsey, 2008; Kacem, et al., 2016). Additionally, irradiation from the cone heater was found to have minimal effect on the flame heat flux. Simulations were evaluated against previous cone calorimeter experiments [6] . AHRR was well-predicted for irradiation of 30 kW m^{-2} and greater, but not for lower irradiation. PHRR was not predicted well overall.

Finally, Auth [37] studied the ability of a modified gas burner to emulate pool fires and condensed phase flames, the burning-rate emulator (BRE). The BRE emulates different fuels by using controlled mixtures of propane, ethylene, or propylene mixed with nitrogen gas. Mixture composition is designed to match the emulated material's heat of combustion. Flame heat feedback was measured both at the center and near the side of the burner and at one intermediate point. Measured heat fluxes to the sample surface from the flame (when emulating condensed phase burning) were significantly higher near the sides than in the center; the intermediate point had heat fluxes lying between the two measured extremes. Since the burner is significantly smaller (only 25 mm diameter), no further comparison will be made but it does supply additional evidence that flame heat feedback is likely non-uniform across the surface of a burning sample in cone calorimetry given the similarity in flames: laminar, buoyant, and in horizontal geometry.

1.2.4 Quantification and modeling of UL-94V

Downey and Quintiere conducted measurements of the UL-94V test to relate test performance to material properties [38,39]. Heat flux of the burner was measured with a water-cooled heat flux gauge embedded in an insulation piece shaped like a UL-94V specimen. Heat flux measurements were either 0.5 or 1 cm from the bottom of the sample and were found to be 57–65 kW m^{-2}. Predictions of ignition times were made using the burner heat flux data, but predictions far exceeded 10 s, even for HB and V-2 rated materials. They also sought to estimate the heat flux and flame length of a diffusion flame characteristic of a burning polymer sample. This task was accomplished by closing the ventilation ports of the burner and attaching a slotted tip to create a diffusion flame which was impinged upon the insulation sample; flame heat flux and flame length were then measured with a heat flux gauge and ruler, respectively [38,39]. Using the flame length measurements, Downey and Quintiere derived a linear expression for flame length as a function of heat release rate per unit area. Heat fluxes of the diffusion flame were measured to be 50–65 kW m^{-2}. Using their measurements, critical HRR criteria for sustained burning (108 kW m^{-2}) and spread (300 kW m^{-2}) were developed. The criteria were compared with virtual HRR calculated for several materials based on the measured net heat fluxes multiplied by each material's heat release parameter. The extinction criteria showed no correlation with UL-94V ratings;

however, materials with a virtual HRR greater than 300 kW m^{-2} tended to fail the test, supporting the spread criterion.

Wang et al. conducted several studies on modeling ignition in UL-94V for several different polymers [40–43]. They began with the development of an ignition model based on local solid temperature, taking into account only heat transfer effects. Initially, the temperature of the burner flame was taken from published values for premixed flames and the convective coefficient was calculated from a correlation for a non-reacting hot gas jet; flame radiation effects were neglected given the nonluminous nature of the burner flame. Later, the heat flux of the burner flame was estimated via experimental measurements [41] using the temperature data from the copper-slug calibration of the burner (ASTM D5207 [44]) while invoking the lumped capacitance assumption. The convective coefficient, h_b, and flame temperature, T_b, of the burner were then determined using least-squares regression and were found to be $h_b = 54.3 \times 10^{-3}$ kW m^{-2} K^{-1} and $T_b = 2026$ K which yield an initial heat flux of ≈ 94 kW m^{-2} (to a room temperature slug). Ignition times were determined experimentally by iteration in exposure time of the burner. Experimentally, the flame always ignited near a corner or edge. Wang et al. simulated the UL-94V test with a varied number of faces heated (otherwise adiabatic); two faces (front and back), three faces (front, back, and bottom), four faces (bottom, front, back, one side), and five faces were considered for the

simulations [40–43]. Note that only the bottom 1 cm of the sample was considered to be heated by the burner flame. In the model, a greater number of faces reduced ignition times and maximum local temperatures occurred in the corners and edges. The simulations with four or more faces (three-dimensional) heated had the best predictions; however, the simulation with three faces (two-dimensional) also performed very well and, in some cases, had better predictions of ignition times [40–43]. They explained that multidimensional heating is responsible for these observations and termed this as edge effects. Further evidence of edge effects was found in burn marks on the edges of the samples.

Wang et al. then developed the ignition model into a flame spread model by including decomposition kinetics, a flame length submodel, and flame heat feedback [43]. UL-94V experiments were conducted using poly(methyl methacrylate) (PMMA) samples. Mass loss was measured using a balance supporting the sample and a digital camera was used to measure experimental flame length. The same parameters for the burner flame derived in their previous study [41] were used. The flame length expression developed by Downey and Quintiere [38,39] was used in their study. Flame heat feedback was assumed to be uniform within the calculated flame length and adiabatic above. PMMA flame heat flux was measured using a copper slug suspended above a burning PMMA bar following the same method done for the burner flame in

their previous study [41] to derive $h_{f,PMMA}$= 52.5 × 10^{-3} kW m^{-2} K^{-1} and $T_{f,PMMA}$ = 1725 K [43]. Decomposition was represented with a single-step Arrhenius expression. The UL-94V test was then simulated for several cases, including one case wherein both the burner heat flux and PMMA flame heat flux were fixed to 60 kW m^{-2} (they would normally be 76.9–94.0 kW m^{-2} and 58.6–74.9 kW m^{-2}, respectively). All simulations overpredicted mass loss rate (MLR) by a factor of ≈ 1.5–3. Additionally, flame lengths were initially underpredicted and rate of spread was overpredicted. Wang et al. then continued to study UL-94V but focused on dripping instead [45–48].

Kempel et al. developed a detailed multiphysics model for the UL-94V test. The materials studied were Polycarbonate/Acrylonitrile butadiene styrene blends with and without flame retardant bisphenol A bis(diphenyl phosphate) and with and without an anti-dripping agent, polytetrafluorethylene. UL-94V tests were conducted with the sample holder on a mass balance to monitor total mass loss. Decomposition kinetics, heats of reaction, heats of complete combustion of volatiles, and dynamic viscosities were all measured in small scale experiments to characterize the decomposition and melt flow of the materials for use in their model. The UL-94V test was simulated in 2D and 3D space using Particle Finite Element Method (PFEM) which combines finite element analysis to solve the mass, momentum, and energy conservation equations with particle-based movement of the nodes to capture melt flow. Heat flux from the burner

was assumed to be equal to the heat flux of a candle flame (150 kW m^{-2}, taken from literature) decaying in power-law fashion with increasing distance from the bottom. Heat flux from the polymer flame was assumed to be proportional to the HRR and also decreased with a power-law relation. Experimental behaviors were captured in the simulations. In 2D simulations without combustion, the model captured dripping behavior and predicted an effective reduction in decomposition due to heat loss. The 3D simulation with combustion predicted extinction times (within 3 s) and ratings well. Kempel et al. commented however, that the boundary conditions were somewhat arbitrary and better characterization of them is needed to improve the model as well as the use of temperature-dependent material properties. Additionally, it is unclear if total MLR (and subsequently flame spread) was predicted well in the 3D simulation with combustion since it was not shown.

For comparison, Table 1 summarizes the boundary conditions and modeling results for the UL-94V test found in the literature. There are discrepancies in the boundary conditions and only two studies report measurements of the burner heat flux.

Table 1. Comparative summary of boundary conditions and modeling results of the UL-94V test reported in previous studies.

Authors	Source	Burner heat flux [kW m^{-2}] to an object at 300 K	Sample flame heat flux [kW m^{-2}] to an object at 300 K	Successful predictions	Unsuccessful predictions
Downey and Quintiere et al.	[38,39]	57–65 Measured directly with water-cooled heat flux gauge (HFG)	50–65 Measured with a HFG heated by a modified methane burner	HB rating	Ignition times, differentiation of non-HB ratings
Wang et al.	[40,41,43]	≈ 94 Analysis of copper slug temperature measurement	≈ 75 Analysis of copper slug temperature measurement heated by burning PMMA	Ignition times	MLR, flame length
Kempel et al.	[49]	≈ 99 (average of first 1 cm) Assumed candle flame with 150 kW m^{-2} max and rapid decay	Not provided explicitly. Calculated from simulation's HRR.	Rating, Extinction times	Unknown if total MLR was predicted. Results not shown

1.2.5 Oxidative pyrolysis of polymers

The oxidative pyrolysis of PMMA has been studied extensively. Early work of Kashiwagi and Hirata et al. measured sample mass and molecular weight of pyrolyzing PMMA via isothermal thermogravimetry and gel permeation chromatograph,

respectively, in nitrogen and air to study the effect of oxygen on its decomposition [50–53]. Samples lost mass and were reduced in molecular weight more rapidly when tested in air than in nitrogen. Molecular weight was reduced more rapidly in samples tests in air than in nitrogen. They found that oxygen primarily acts at the surface of the sample as evidenced by comparing the results using 0.2 mm thick samples and 0.9 mm thick samples; thicker samples showed greater polydispersity than thinner samples until after about 100 minutes. This suggests that the rate of diffusion of oxygen through the sample is much slower than the rate of oxidative degradation. They explained that oxygen acts mostly by random chain scission to enhance decomposition. Evidence supporting this is based on the large and rapid reduction in molecular weight.

Dakka performed thermogravimetric analysis (TGA), differential thermal analysis (DTA), and mass spectrometry to better understand the nature (exothermic or endothermic) and magnitude of the heats of reaction associated with oxidative degradation of PMMA [54]. The samples were relatively large shavings, 90 mg in mass and 0.5 mm diameter, as a heating rate of 4 K min^{-1}. Tests were performed using 0 (pure N_2), 5, 7.5, 10, 15 and 21 vol% oxygen concentrations. The DTA showed multiple peaks only one of which was associated with a peak in the TGA data; the peak associated with mass loss was endothermic but the other peaks were exothermic. Like

other studies, Dakka also saw that the presence of oxygen resulted in decomposition at lower temperatures.

Senneca et al. studied the thermal and thermal-oxidative degradation of polytheylene (PE) and Polyethylene terephthalate (PET) via TGA experiments for 0 (pure N_2), 5, 10, and 21 vol% oxygen concentrations (balance nitrogen) and heating rates of 5, 10, 20 K min^{-1} [55]. Much like other studies of other polymers, the mass loss curves were shifted to lower temperatures in oxygen. However, PE showed an increasing shift to lower temperatures with increased oxygen concentration while PET did not see such an effect (but the rate of degradation was increased). Senneca also used the Kissinger method to obtain kinetic parameters, based on the normalized mass data, while also accounting for the dependence on oxygen concentration; note that this analysis assumes oxygen is available throughout the sample volume and not just the surface. No analysis was performed regarding the effect of surface area. The reaction order for the dependence on oxygen concentration was 0.6 for PET and 0.35 for PE.

Several other studies were less experiment-driven but instead provided in-depth analysis on proposed reaction mechanisms of thermal and oxidative degradation for PMMA [56] as well as other polymers such as polystyrene, polyethylene, and polypropylene [57,58].

1.3 Research objectives

Flame heat flux in the cone calorimeter has been studied substantially; however, the definition of flame heat flux has varied amongst previous works, leading to disparities in reported values. These disparities cannot be reconciled without making assumptions, introducing uncertainties into any comparison. The quality of predictions of cone calorimetry can be improved as well. Furthermore, the dependence of flame heat flux on variables such as position across the sample, sample material, irradiation, burning rate, and the nature of the flame heat flux (radiative or convective), remains unclear and merits further investigation.

Comparative analysis of the literature has found that UL-94V ratings have only weak correlation with the results of other fire tests. The LOI is not a good predictor due to large overlap between V-0 and V-1 rated materials. HRR_0 is only a good predictor for very low and very high HRR_0. There are limited measurements characterizing the UL-94V test and significant discrepancies in the definition of the boundary conditions. Only one study has produced a model that could reasonably predict the outcome of the UL-94V test [49]; however, the boundary conditions used in the model were not experimentally validated. Additionally, no study has successfully predicted the flame spread on a UL-94V sample. It is also unclear if the UL-94V test can be modeled two-dimensionally or if three-dimensional effects must be considered.

Finally, although the mechanisms of oxidative pyrolysis have been well studied for polymers, there remains several concepts not yet well understood. Only one study investigated the dependence of oxidative kinetics as a function of oxygen concentration. Additionally, although several studies point out that oxidation acts primarily at the surface, suggesting that gasification due to oxidative pyrolysis would scale with surface area, none have confirmed this relationship at a larger scale. As this work found, accurate modeling of oxidative pyrolysis is critical for prediction of ignition in simulations of the cone calorimeter and UL-94V tests.

Based on the findings of the literature and the goals of this work, there are four overall objectives.

1. Develop quantitative understanding of the key phenomena of the cone calorimeter and UL-94V tests via experimental measurements.
2. Develop empirical submodels for these phenomena for numerical simulation of the cone calorimeter and UL-94V tests.
3. Further investigate the dependence of oxidative pyrolysis on oxygen concentration and surface area.
4. Develop and validate empirical models for oxidative pyrolysis.

1.4 Dissertation outline

The remainder of this dissertation is structured in the following manner. First, in Chapter 2 is a description of the previous development of pyrolysis models. This description is included because the pyrolysis models are an integral part of the model and represent a significant effort. Chapter 3 concerns the quantification and modeling of the cone calorimeter test. Chapter 4 concerns the quantification and modeling of the UL-94V test using poly(methyl methacrylate) (PMMA) while chapter 5 represents the extension of the model to other polymers and compares the results. Chapter 6 concerns the oxidative pyrolysis. Chapter 7 summarizes the conclusions of this work.

Chapter 2: Previous development of comprehensive pyrolysis models

This work represents an extension from pyrolysis modeling to fire test modeling by quantifying the conditions of standard fire tests, including flame heat feedback. Although the development of the pyrolysis models is not the focus of this dissertation, the pyrolysis models are integral to this work's modeling and thus will be discussed briefly.

2.1 Overview of development process

Comprehensive pyrolysis models have been developed using a hierarchical approach based upon inverse analysis of milligram and gram scale experiments. The hierarchical approach isolates the processes of pyrolysis and the resulting model increases in complexity with each step. First, milligram-scale tests including thermogravimetric analysis, differential scanning calorimetry, and microscale combustion calorimetry are performed to determine the reaction kinetics, thermodynamics, and energetics. By using milligram-scale samples, heat and mass transfer effects can be neglected and sample temperatures are uniform and well-defined. Then, gram-scale gasification tests and radiation absorption coefficient

measurements are performed to determine transport properties and to validate the model. A more detailed overview of pyrolysis modeling and development can be found elsewhere [59–61].

2.2 ThermaKin2Ds modeling tool

Models were evaluated in ThermaKin2Ds, which is a numerical pyrolysis solver that solves mass and energy conservation expressions to compute the rate of gasification and temperature distribution of a pyrolyzing solid in response to external heating [24]. In ThermaKin2Ds, materials are represented by elements containing mixtures of one or more components. Each component is categorized as a solid, liquid, or gas and is defined by a set of temperature dependent properties. Components may undergo reactions to capture physical and chemical changes. Up to 50 components may be defined. ThermaKin2Ds can simulate in 1D, 2D (Cartesian), or 2D axisymmetric geometries. 1D and 2D simulations were conducted for this work so the description shall focus on the equations for Cartesian coordinates. Objects in 2D are defined in x and y space where $x = 0$ is the back boundary and $y = 0$ is the bottom boundary. The top and bottom boundaries are impermeable to mass or heat flow while the front and back boundaries may allow for mass and heat transfer. 1D objects only have a top and bottom boundary and are defined using x only. The initial state of the material is

described by the user in terms of material length, material thickness, temperature, and composition. These quantities do not have to be uniform, allowing ThermaKin2Ds to simulate several materials and scenarios. The key expressions of the Cartesian model in ThermaKin2Ds are summarized as follows:

$$\frac{\partial \xi_j}{\partial t} = \sum_{i=1}^{N_r} \theta_i^j r_i - \frac{\partial J_j^x}{\partial x} - \frac{\partial J_j^y}{\partial y} + \frac{\partial}{\partial x}\left(\xi_j \int_0^x \frac{1}{\rho}\frac{\partial \rho}{\partial t} dx\right) \quad (1)$$

$$r_i = A_i \exp\left(-\frac{E_i}{RT}\right) \xi_k \xi_l \quad (2)$$

$$J_g^x = -\rho_g \lambda \frac{\partial(\xi_g/\rho_g)}{\partial x} \quad (3)$$

$$\sum_{j=1}^{N} \xi_j c_j \frac{\partial T}{\partial t} = \quad (4)$$

$$\sum_{i=1}^{N_r} H_i r_i - \frac{\partial q_x}{\partial x} - \frac{\partial q_y}{\partial y} - \frac{\partial I_{ex}}{\partial x} + \frac{\partial I_{rr}}{\partial x} - \sum_{g=1}^{N_g} c_g \left(J_g^x \frac{\partial T}{\partial x} + J_g^y \frac{\partial T}{\partial y}\right) + c\rho \frac{\partial T}{\partial x} \int_0^x \frac{1}{\rho}\frac{\partial \rho}{\partial t} dx$$

$$q_x = -k \frac{\partial T}{\partial x} \quad (5)$$

$$\frac{\partial I_{ex}}{\partial x} = -I_{ex} \sum_{j=1}^{N} \alpha_j \xi_j \quad (6)$$

$$\frac{\partial I_{rr}}{\partial x} = \frac{\varepsilon \sigma T^4}{I_{ex}^0} \frac{\partial I_{ex}}{\partial x} \quad (7)$$

Equation (1) represents the conservation of mass expression for a component, j, written in terms of concentration, ξ_j [kg m^{-3}], which is defined as mass per unit

volume in a given element. On the right are the processes which affect ξ_j including production or consumption due to a chemical reaction (term 1), mass flow in or out of the element in the x and y directions (terms 2 and 3) – note that only gaseous components are mobile – and mass transfer due to expansion or contraction of the material (term 4). Term 1 of Equation (1) constitutes a mass-based stoichiometric coefficient for component, θ, multiplied by a rate of reaction, r_i [kg m^{-3} s^{-1}], governed by an Arrhenius expression shown in Equation (2). θ is positive if the component is being produced by the reaction and negative if it is being consumed. Arrhenius parameters are prescribed by the user and are often determined from inverse-analysis of milligram-scale thermogravimetric experiments. ξ_k and ξ_l are the concentrations of the reactants. If there is only one reactant, ξ_l is set equal to one. Equation (3) describes the mass flux of a gaseous species based upon the gradient of its volumetric concentration. Equation (4) describes the conservation of energy. On the left is the rate change of sensible heat of the element. On the right are the relevant processes including: heat associated with the chemical reactions (term 1); heat transfer in or out due to conduction in the x and y directions (terms 2 and 3); in-depth radiation absorption from an external source (term 4); re-radiation to the surroundings (term 5); convection due to mass flow of gases (term 6); and changes in sensible heat due to expansion or contraction of the material (term 7). Expansion and contraction terms are

included since ThermaKin2Ds uses an Eulerian description for fluid flow. Note that several of these terms are defined further in equations (5) through (7). Equation (5) describes heat conduction based on Fourier's law. Equation (6) represents the absorption of thermal radiation based on the Beer-Lambert law. Equation (7) describes thermal re-radiation of the material to the surroundings based on the Stefan-Boltzmann law.

The symbols of equations (1) through (7) are the following: t is time [s]; N_r is the number of reactions occurring within an element; ρ is density [kg m^{-3}]; c is the heat capacity [J kg^{-1} K^{-1}]; N is the number of components in the element; H is the heat of reaction (positive if exothermic) [J kg^{-1}] ; A [s^{-1} or kg^{-1} m^3 s^{-1} if second-order] and E [J mol^{-1}] are the Arrhenius parameters; R is the molar gas constant [J mol^{-1} K^{-1}]; λ is the gas transfer coefficient [m^2 s^{-1}]; k is the thermal conductivity [W m^{-1} K^{-1}]; α is the radiation absorption coefficient [m^2 kg^{-1}]; ε is the emissivity; σ is the Stefan-Boltzmann constant [W m^{-2} K^{-4}]; I_{ex} is the external radiation through an object boundary that was not reflected [W m^{-2}]; and I_{rr} is the re-radiation to the environment [W m^{-2}]. Properties with subscripts belong to an individual component while properties without a subscript are a property of the mixture within an element, such as ρ. The density of a mixture is defined by one divided by the sum of the mass fractions, normalized by density, of each component; the contribution of gases is weighted by a factor to control the degree to

which swelling is considered. The specific heat of a mixture is based on the sum of the product of the components' individual mass fractions and specific heats. Concentrations and temperatures of the elements are determined over time by integration in very small timesteps. Explicit integration is used in the y dimension while integration in the x dimension uses a more stable Crank-Nicolson scheme since the temperature and concentration gradients are greater in this dimension and since it is the dimension associated with radiation heat transport. Further information on ThermaKin2Ds, including syntax, can be found elsewhere [24,62]. Finally, ThermaKin2Ds allows the user to carefully prescribe mass and heat transfer boundary conditions, enabling ThermaKin2Ds to simulate a wide range of pyrolysis and fire scenarios. In this work, this feature was used to develop and evaluate flame heat feedback submodels, as described later in chapters 3 and 4.

2.3 Milligram-scale measurements

2.3.1 Thermogravimetric Analysis and Differential Scanning Calorimetry

Thermogravimetric analysis (TGA) and Differential Scanning Calorimetry (DSC) were performed using a Netzsch 449 F3 Jupiter Simultaneous Thermal Analyzer. Tests were conducted at 10 K min^{-1} for model development and later at 5 K min^{-1} and 20 K min^{-1} for validation [59,62–64]. All tests were performed in nitrogen

because once ignition occurs, the presence of flame prevents oxygen from reaching the solid's surface such that solid decomposition occurs in inert conditions. Platinum-Rhodium crucibles were used for their high temperature capabilities and sensitivity to heat flow. Sample masses were 4-7 mg to be thermally thin. Although the TGA and DSC data were recorded simultaneously, the TGA data are first used in inverse analysis. The mass and mass loss rate data from TGA were used to develop reaction schemes and obtain kinetic parameters (activation energies and pre-exponential factors) for said schemes. The heat flow data from the DSC was used to obtain material specific heats and heats of reaction.

2.3.2 Microscale combustion calorimetry

Once the kinetics and thermodynamics were determined, microscale combustion calorimeter (MCC) tests [65] were performed to obtain heats of complete combustion of gasesous volatiles. The MCC consists mainly of the pyrolyzer and the combustor portions. In the pyrolyzer portion, a milligram-scale sample in a ceramic crucible is heated at a rate of 10 K min^{-1} in a flow of nitrogen gas to produce gaseous volatiles. The volatiles are carried by the nitrogen flow to the combustor portion wherein the gases are mixed with excess oxygen to ensure complete combustion. Heat release rate was then calculated based on the principle of oxygen consumption much

like the cone calorimeter [2]. The HRR data was then used with the decomposition model in ThermaKin2Ds to determine the heats of combustion (Δh_c) of the gaseous component(s) via inverse analysis until simulated HRR agrees with experimental HRR.

2.4 Gram-scale measurements

2.4.1 Radiation absorption coefficient measurements

Radiation absorption coefficients were measured by subjecting a thin polymer sample, 0.1 cm thick, to a well-defined radiant heat flux from a conical heater and comparing the incident heat flux (usually ~45 kW m^{-2}) with the radiative heat flux transmitted through the sample measured via a Schmidt-Boelter heat flux gauge. Incident heat flux was known by measurement without the sample in place. Heat flux data transmitted through the sample were collected in a very short interval to ensure that the gauge does not capture heat flux due to conduction. This process was repeated for several samples. Once sufficient data were collected, the absorption coefficient, κ , can be calculated from $\kappa = \left(2\ln(\varepsilon) - \ln(I_T/I_0)\right)/\rho\delta$ where ε is the emissivity of the polymer (usually found from the literature), ρ is the material density, δ is the thickness, I_T is the transmitted heat flux and I_0 is the incident heat flux without the polymer sample in place. Further details on this process can be found elsewhere [60].

2.4.2 Controlled Atmospheric Pyrolysis Apparatus

The Controlled Atmospheric Pyrolysis Apparatus (CAPA or CAPA II, the most recent version) is an apparatus that pyrolyzes samples in a manner quite similar to that of the cone calorimeter but in a much more controlled fashion; a schematic of CAPA is depicted in Fig. 3. Samples were discs typically 7 cm in diameter and are heated by a conical heater identical to those used in a cone calorimeter. However, unlike the cone calorimeter, the sample pyrolyzes in a nitrogen environment to avoid ignition and to avoid oxidative effects. Additionally, the walls of the sample holder are water-cooled to ensure well defined conditions at the edges and to minimize re-radiation to the sample. The heat flux of the heater was previously categorized in several positions and several angles so that the incident heat flux was well understood even for swelling samples. The bottom of the sample was adhered to copper foil and temperature was recorded via an IR camera to monitor the bottom surface temperature of the sample in a non-invasive matter. Bottom surface temperatures are used in inverse-analysis to obtain thermal conductivities of the components via inverse analysis using ThermaKin2Ds with either 1D or 2D axisymmetric geometries; 2D axisymmetric geometry is used to model materials which swell significantly and non-uniformly (in the radial direction). Sample shape was recorded via a camera looking through an observation window; such data were used to determine densities of intermediate

components. Finally, sample mass loss rate (gasification rate) was recorded via a load cell and mass loss rate data were later used to validate the pyrolysis model. Further details on this process can be found elsewhere [60].

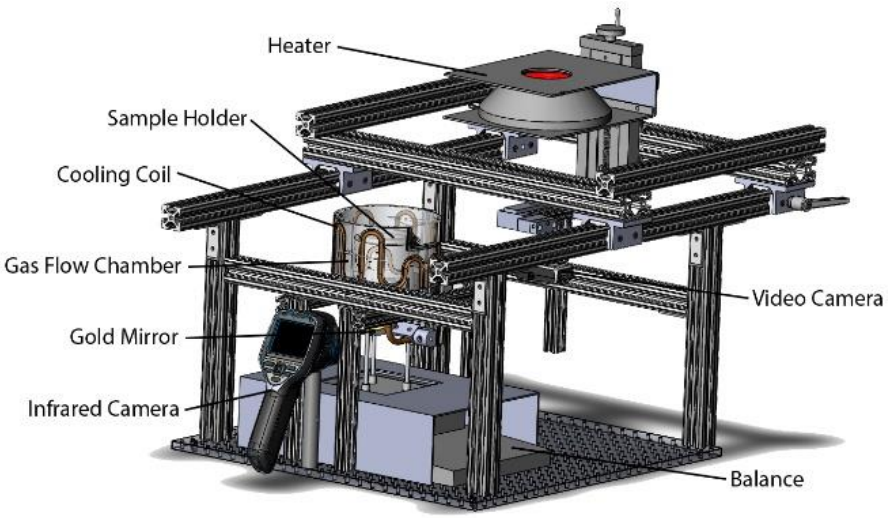

Fig. 3. Schematic of CAPA II apparatus.

2.5 Example summary of pyrolysis model

As an example, the pyrolysis model for clear, extruded PMMA is described below in Tables 2-5. Details of other pyrolysis models are provided in the Appendix A. Overall, pyrolysis models of the materials used in this study were able to predict gasification rates within 14%, on average [59,62–64].

Table 2. PMMA reaction scheme [64]

#	Reaction
1	PMMA → PMMA_Glass
2	PMMA_Glass → 0.015 PMMA_Res1 + 0.985 PMMA_Gas1

Table 3. PMMA reaction kinetics and heats of reaction. Endothermic heats of reaction are marked as positive [64]

#	A [s^{-1} or m^3 kg^{-1} s^{-1}]	E [J mol^{-1}]	H [J kg^{-1}]
1	1	0	0
2	8.6×10^{12}	1.88×10^5	8.46×10^5

Table 4. PMMA component properties [64]

Component	ρ [kg m^{-3}]	ε	κ [m^2 kg^{-1}]	k [W m^{-1} K^{-1}]	c [J kg^{-1} K^{-1}]
PMMA	1155	0.95	1.94	0.45 -3.8 × 10^{-4} T	601 + 3.63 T
PMMA_Glass	1155	0.95	1.94	0.27 - 2.4 × 10^{-4} T	601 + 3.63 T
PMMA_Res1	1155	0.95	1.94	0.27 - 2.4 × 10^{-4} T	601 + 3.63 T

Table 5. PMMA gaseous heats of combustion

Component	MCC ([65]) Δh_c [kJ kg^{-1}]
PMMA_Gas1	24.5

Chapter 3: Cone calorimetry quantification and modeling

The goal of this work is to quantify the conditions of standard fire tests such as the cone calorimeter. Flame heat feedback is a key quantity since it affects HRR and was measured directly in cone calorimeter tests for multiple polymers. The measurements were used to determine expressions for use in simulations. Simulations of the cone calorimeter test were performed and then compared with experimental HRR. A blind comparison with cone calorimetry of a wood-based product was also performed for further validation.

3.1 Materials and sample preparation

The materials utilized were high-impact polystyrene (HIPS), clear, extruded poly(methyl methacrylate) (PMMA), poly(oxymethylene) (POM), and glass-fiber reinforced (25 wt.%) poly(butylene terephthalate) (PBT/GF) with and without 16 wt.% of aluminum diethyl phosphinate (DEPAL) in the form of extruded sheets as well as Blue Ribbon PS2-10-compliant oriented strand board (OSB), a commercial wood product. HIPS, PMMA, and POM were 0.6, 0.6, and 0.635 cm thick, respectively. Both PBT/GF and PBT/GF/DEPAL were 0.56 cm thick. The OSB was 1.08 cm thick. The materials were manufactured by Spartech Plastics, Evonik Industries, Ensinger, BASF, and Georgia-Pacific, respectively. Glass fiber is an inert filler and aluminum diethyl

phosphinate is a phosphorous-based flame retardant that acts in the gas phase and, to a lesser degree, in the condensed phase [66]. HIPS, PMMA, and POM were selected because they do not exhibit complex swelling behavior, represent a wide range of chemical structure, and because comprehensive pyrolysis models had been developed previously for these materials [64]. PBT/GF with and without DEPAL was chosen to determine what effect, if any, a gas-phase-active flame retardant has on flame heat flux; it was also chosen because a comprehensive pyrolysis model had been previously developed for it [67]. These materials were used for measurements of flame heat feedback and to parameterize a model for simulation of cone calorimetry. OSB was not used in the parametrization and but served as a separate validation exercise (see section 3.9). For all materials, samples were squares with sides of 10 ± 0.2 cm. All samples were dried in a desiccator for a minimum of 48 hours. The same materials used in the pyrolysis model development [64,67–69] were used for all tests.

3.2 Cone calorimeter tests and heat flux measurement

Cone calorimeter tests were conducted in accordance with ASTM E1354 [70]. Prior to testing, calibration of the gas analyzers, load cell, and C-factor (the orifice coefficient in the heat release rate measurement) were performed. Gas analyzers were calibrated by flowing nitrogen (to obtain a zero point) and CO/CO_2 gases. Load cell

calibration entailed a zero point as well as a span point using a calibration weight placed on top. The C-factor was calibrated via a 5 kW methane burner, in accordance with ASTM E1354 [70]. Then, a preliminary test using black, extruded poly(methyl methacrylate), 0.6 cm thick, under 50 kW m^{-2} irradiation, was conducted to verify the calibration. If the measured heat of combustion was not within the uncertainty of the theoretical value for PMMA, then the calibration process was redone. Cone calorimeter tests were conducted in the horizontal orientation. Three sheets of 0.64 cm thick Kaowool PM were utilized for insulative backing. The bottom and side surfaces of the samples were wrapped with aluminum foil. The top surface of the sample was placed 2.54 cm below the bottom of the conical heater. Ignition was accomplished by a spark igniter at 1.3 ± 0.2 cm above the sample surface. The edge frame was not used. All tests were videotaped. The irradiation was set using the cone calorimeter's reference Schmidt-Boelter water-cooled heat flux gauge. Two types of data were collected from tests, HRR or heat flux, but not both simultaneously.

The HRR measurements were conducted first and were used later for model validation. For the polymers, set irradiation levels were 20 and 50 kW m^{-2}. However, these values were found to be 20.6 and 51.5 kW m^{-2} after checking and correcting the calibration of the cone calorimeter's reference gauge against a NIST-traceable reference. For OSB, set irradiation levels were 25 and 50 kW m^{-2} to match the level of

irradiation used in the pyrolysis model development; the heat flux calibration was confirmed to be correct. Cone calorimeter tests were conducted in triplicate for both irradiation levels for HIPS, PMMA, and POM and in duplicate at 51.5 kW m^{-2} for PBT/GF and PBT/GF/DEPAL; PBT/GF and PBT/GF/DEPAL were not tested under low irradiation (20.6 kW m^{-2}) because a preliminary test showed they do not sustain burning at this setting. Tests of OSB were conducted in triplicate for 25 kW m^{-2} and in duplicate for 50 kW m^{-2} since these results showed high repeatability.

Two Medtherm, 0.95 cm diameter water-cooled, 180° viewing angle, Schmidt-Boelter gauges were used to measure flame heat flux and held at a constant temperature of 291 K; these measurements were performed on all polymers but not OSB which serves only for validation. 0.96 cm diameter holes were drilled into samples and insulative backing in the center and 1.37 cm inwards from one edge to allow for the insertion of heat flux gauges. The gauge surfaces were positioned 0.2 cm above the initial sample surface to account for sample swelling during the test. High temperature optical black coating with emissivity of 0.94 was used to paint the gauges. Once painted, the gauges were individually calibrated 2.54 cm below the base of the conical heater, in the center, against multiple incident heat fluxes measured by the cone calorimeter's reference heat flux gauge after its calibration had been corrected. Heat flux gauges were cleaned, re-painted, and re-calibrated before every test. Heat flux was

recorded by a data acquisition module at a rate of 1 Hz. To be consistent with the HRR measurements, set irradiation levels were 20.6 and 51.5 kW m^{-2}. Flame heat flux measurements were repeated thrice for tests under low irradiation and twice for tests under high irradiation because higher irradiation results were more reproducible. Fig. 4 depicts the geometry of the sample, specimen holder, and heat flux gauges. In addition, supplementary tests were conducted on PMMA and HIPS under 20.6 kW m^{-2} irradiation wherein caps made of copper tube stuffed with Kaowool PM insulation covered the top surfaces of the heat flux gauges until 145 ± 10 s after ignition [71], after which the caps were removed. Heat fluxes recorded after the removal of the caps agreed with the heat fluxes recorded in the tests without caps, verifying that, within the relevant time frame, gauge surface deposits did not affect the accuracy of the readings.

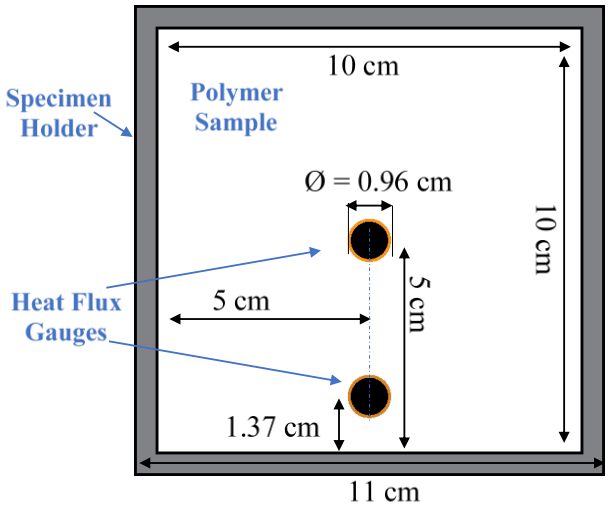

Fig. 4. Illustration of the specimen holder, sample, and heat flux gauge placement.

3.3 ThermaKin2Ds cone calorimetry simulations

Simulations of cone calorimetry consisted of a single layer of sample material (HIPS, PMMA, POM, PBT/GF, PBT/GF/DEPAL, OSB) on top of a layer of Kaowool PM 1.9 cm thick under 20.6, 25, 50, or 51.5 kW m^{-2} irradiation, as appropriate. Although OSB is known to have layers of varied density, previous simulations of CAPA II experiments showed that a uniform density assumption provides equally accurate predictions [69] and thus, a uniform density profile was assumed. 1.9% water content (mass-based) of OSB was also considered in the simulation. Spatial discretization was 0.005 cm and time step size was 0.01 s. Decreasing these parameters by a factor of ten had negligible impact, demonstrating convergence. The top boundary conditions for cone calorimetry modeling are described later in sections 3.6.1 and 3.6.2. The Kaowool PM insulation underneath the sample was explicitly modeled. Its density was 256 kg m^{-3}; heat capacity was 1070 J kg^{-1} K^{-1}; and its thermal conductivity [W m^{-1} K^{-1}] was defined as $k_{insulation} = 0.052 - 4 \times 10^{-5}\, T + 1 \times 10^{-7}\, T^2$, where T is the temperature of the insulation [K].; these properties were taken from the manufacturer's data sheet [72] which had been confirmed in a separate study [73]. The radiation absorption coefficient was set high so that it was non-transparent. It was assumed that no gas was transported through the Kaowool PM (due to the presence of aluminum foil). The bottom boundary of the insulation was treated as adiabatic. For the polymers,

simulated HRR was calculated by multiplying the simulation's total mass loss rate by the effective heat of combustion measured in the cone calorimeter experiments, see section 3.5.1, to best emulate the experiments. For OSB, simulated HRR was calculated by multiplying the mass production rate of each gaseous component by its heat of combustion measured in MCC experiments [68] and then summing; this is done because the evolution of OSB pyrolyzate gases is complex and their heats of combustion vary greatly.

3.4 TGA for oxidation effects in air

In cone calorimeter tests, prior to ignition, the presence of oxygen in the air near the sample surface can enhance solid decomposition and potentially affect the time of ignition, as discussed in section 1.2. This is more relevant when testing at low levels of irradiation since ignition times are longer (on the order of minutes) allowing more time for oxygen to act but less so for high levels of irradiation for which ignition times are short. To investigate the effects of oxygen on the decomposition of the tested polymers, supplementary TGA tests were conducted using a Netzsch 449 F3 Jupiter Simultaneous Thermal Analyzer. TGA tests were not conducted for PBT/GF, PBT/GF/DEPAL, and OSB because these materials ignited quickly in all cone calorimeter tests and were thus exposed to oxygen only momentarily. Two tests, one in nitrogen and one in an aerobic

environment (21 vol% O_2, balance N_2), were conducted each for HIPS, PMMA, and POM with initial masses of 4–7 mg. Samples were small solid pieces; sample surface area was not controlled since these tests were a preliminary investigation. In the later UL-94V study, the sample surface area was better controlled. The nitrogen flow rate was always fixed at 50 mL min^{-1}, but for the tests in the aerobic environment, an additional 13 mL min^{-1} flow of oxygen was added. The sample was held in a platinum-rhodium crucible without a lid. The heating rate was set to 10 K min^{-1}. Sample mass was recorded as a function of time and temperature.

3.5 Experimental results

The experimental results of section 3.5 pertain to the polymers while the experimental results of OSB can be found in section 3.9.

3.5.1 Cone calorimetry: HRR & heats of combustion

Heat release rate (HRR) and mass loss data were obtained from cone calorimeter tests. Fig. 5 shows the HRR results under 21.6 kW m^{-2} irradiation and Fig. 6 shows the HRR results under 51.5 kW m^{-2} irradiation; the shaded areas represent the scatter of the experimental data ± 5%, as to account for the 5% systematic uncertainty in the orifice coefficient [74]. As the figures show, when the irradiation is increased, time to ignition and burning duration decrease while HRR increases. At both levels of

irradiation, HIPS and PMMA have the greatest HRR (comparable to one another). PBT/GF has the next greatest HRR then POM and then PBT/GF/DEPAL, highlighting the effectiveness of DEPAL in reducing HRR. All materials except for the PBT-based blends show simple burning behavior: ignition followed by a steady increase in burning, a plateau of peak HRR, and then a decrease in burning until extinction. PBT/GF shows a large initial peak and then a smaller plateau of steady HRR. PBT/GF/DEPAL also shows an initial peak in HRR and then a smaller plateau. Experimentally, adding DEPAL reduced average HRR by 39% and peak HRR by 50%, the calculation of both of which is described later in section 3.7.

Effective heat of combustion values were calculated by numerically integrating the HRR data for the whole test and dividing by volatilized mass. All polymer samples, except those with glass fiber, left little to no residue. The effective heats of combustion were averaged from tests at both irradiation conditions (with the exception of PBT/GF and PBT/GF/DEPAL which have only a single condition). The uncertainties in the effective heats of combustion are taken as two standard deviations of the mean plus the 5% systematic uncertainty in HRR measurement. Table 6 summarizes the effective heat of combustions values calculated in this work and the effective heat of combustion measured by Leventon et al. who used the same configuration [75]. The effective heats of combustion measured in this work are on average, within 6% of the values reported

by Leventon et al. which is within the uncertainty of this work. Additionally, although DEPAL reduces HRR by about 39%, the effective heat of combustion is only reduced by 10%. This can be explained by how the HRR curve for PBT/GF/DEPAL is slightly wider (burns longer) and that less mass was burned.

Table 6. Comparison of effective heats of combustion determined in this work and a previous study using cone calorimetry [75]**.**

	Effective heat of combustion [kJ g^{-1}]	
Material	**This work**	**Leventon** [75]
HIPS	30.1 ± 2.1	27.9 ± 0.7
PBT/GF	19.9 ± 1.0	21.6 ± 0.3
PBT/GF/DEPAL	18.1 ± 0.9	–
PMMA	25.5 ± 1.8	23.8 ± 0.2
POM	15.3 ± 1.1	14.9 ± 0.2

Additionally, the instantaneous heats of combustion were calculated by dividing the average HRR by the average MLR for each material. Plots of the instantaneous heat of combustion can be found in section A2.1 of the Appendix. The instantaneous heats of combustion were found to be constant for those materials with a single gaseous product in its pyrolysis model (HIPS, PMMA, and POM) and agreed well with the effective heats of combustion determined by integration. Thus, the HRR and MLR are effectively equivalent and can be used interchangeably for these materials. The instantaneous heats of combustion of the PBT-based blends were not constant, but that was expected since multiple gas species with differing heats of

combustion are produced, as was found via MCC experiments [67]; unlike the cone calorimeter, the MCC is capable of distinguishing the heats of combustion of the individual gases evolved since MCC data can be coupled directly with TGA data since the experimental conditions (heating rate, sample mass, and atmosphere) are identical in the pyrolyzer section of the MCC. For consistency, the HRR will be used as the target variable for the PBT-based materials as well. HRR is also the preferred variable because it is the variable used in previous studies for evaluating cone calorimetry models [23,26,28,34] and thus allows for the most direct comparison with past work.

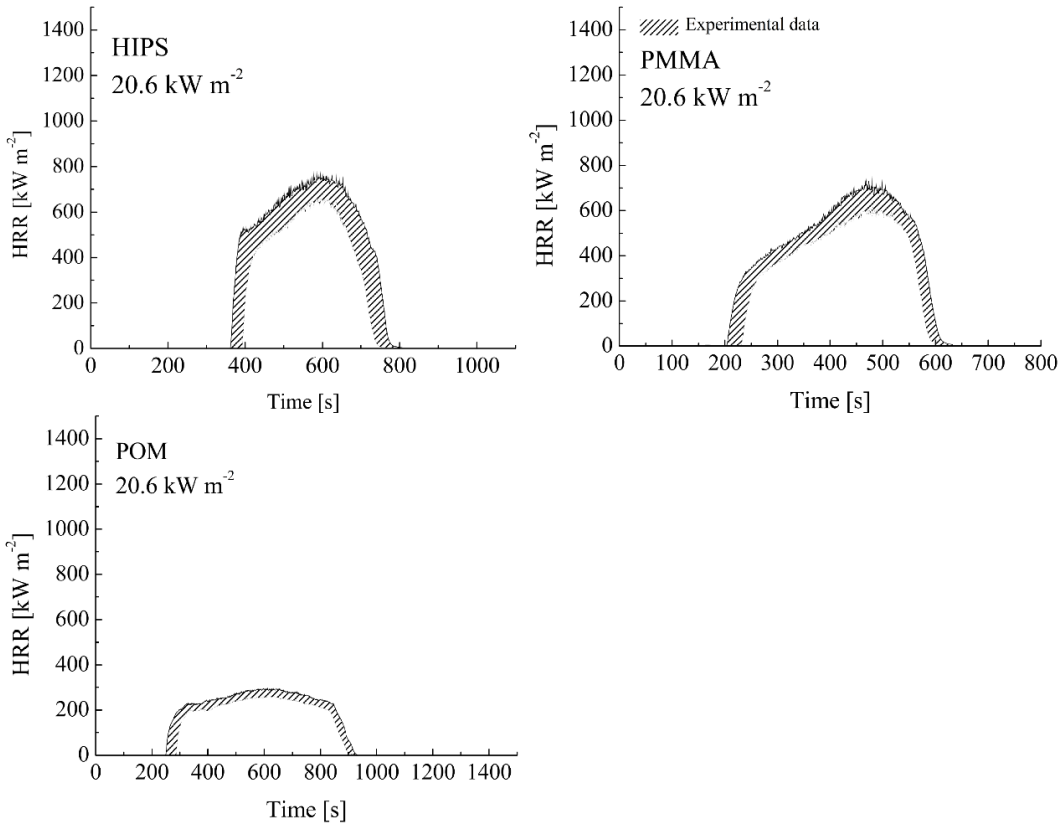

Fig. 5. Experimental HRR measurements for HIPS, PMMA, and POM conducted at 20.6 kW m^{-2} irradiation.

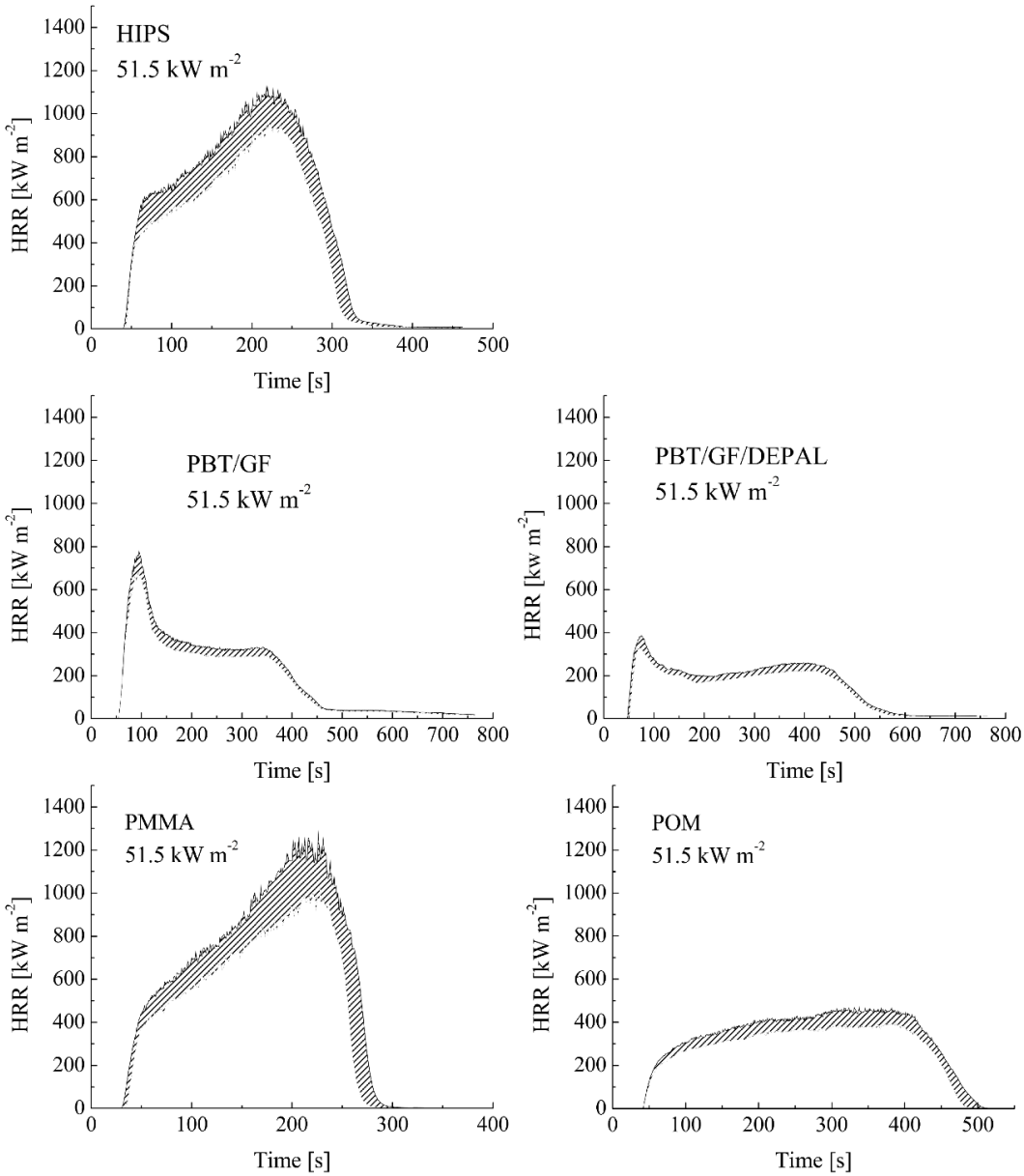

Fig. 6. Experimental HRR measurements for all materials tested under 51.5 kW m^{-2} irradiation.

3.5.2 Images of flames during full surface burning

Images of full surface burning are shown in Fig. 7. Images were taken 6–25 s after ignition, equivalently, the first 3-7% of burning time. Full surface burning was defined as the presence of flame across the entire top surface and was identified by visual observation from the video recording. As shown in Fig. 7, the flames are bell-shaped with the base of the flame much closer to the sample surface near the edges of the sample than in the center. The PMMA and POM images show that irradiation has little effect on the base of the flame. PBT/GF/DEPAL flame appears broken up and variegated in comparison to the uniform flame sheet of the other materials. It is unclear whether this is due to condensed-phase or gas-phase activity.

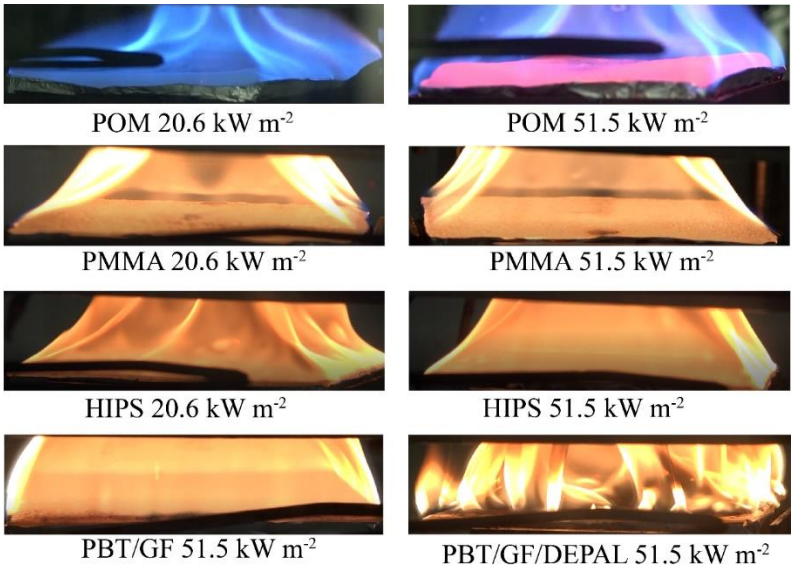

Fig. 7. Images of full surface burning in cone calorimeter tests. The black shadow in the foreground of the POM images is the spark igniter.

3.5.3 Flame heat fluxes in cone calorimeter

Total heat flux to the water-cooled heat flux gauge includes contributions from the conical heater and the flame. For the materials tested, their flames may or may not significantly absorb irradiation from the heater. To evaluate this possibility, the amount of irradiation absorbed by the flame was estimated for each material. The heat flux measured at the sensor is given by $q''_{total} = q''_{flame} + (1-\eta)q''_{cone}$ where q''_{total} is the total heat flux measured [kW m^{-2}], q''_{flame} is the flame heat flux [kW m^{-2}], q''_{cone} is the irradiation of the conical heater [kW m^{-2}], and η is the fraction of irradiation absorbed by the flame [–]. If neither q''_{flame} nor η depend strongly on the irradiation of the heater, which is supported by observations of an unchanged flame structure from low to higher irradiation, then by comparing total heat flux measurements at two different levels of irradiation, the q''_{flame} term can be eliminated and η can be determined. η was computed for multiple tests and averaged together for each material. Effectively zero absorption was calculated for PMMA and POM. For HIPS, the absorption at low irradiation was estimated to be comparable to the uncertainties of the total heat flux measurements. This was not the case however, for high irradiation where the absorption was estimated to be significantly larger than the uncertainties. Consequently, no analysis was performed for the heat flux measurements of HIPS at 51.5 kW m^{-2}

irradiation. The absorption of irradiation could not be directly computed for PBT/GF and PBT/GF/DEPAL because these tests were only performed at 51.5 kW m^{-2} since they do not burn at lower irradiation. However, based on the other experimental results, it is likely PBT/GF was impacted by the absorption of irradiation while PBT/GF/DEPAL was likely not. Regarding PBT/GF, its flame heat flux measurements resembled those of HIPS at 51.5 kW m^{-2} irradiation with the calculated flame heat flux starting high and then quickly approaching zero. Additionally, images of the PBT/GF flame show that it is a sooty, thick flame much like burning HIPS at 51.5 kW m^{-2}. Thus, given the similarity to HIPS at 51.5 kW m^{-2}, it is likely that the PBT/GF flame significantly absorbed the irradiation of the heater, prohibiting determination of the flame heat flux. Regarding PBT/GF/DEPAL, its heat flux measurements behaved more like PMMA and POM, with a clear plateau of steady measurement as shown later in Fig. 8. Additionally, images of burning PBT/GF/DEPAL show the flame is broken and thinner. Thus, it will be assumed that absorption of the irradiation does not have to be considered for PBT/GF/DEPAL and further analysis will be performed.

Flame heat flux (relative to the cold gauge) was thus determined from total heat flux by subtracting the irradiation of the heater. The average irradiation of the heater was determined for each test by taking the average of the total heat flux 100 s before ignition for the 20.6 kW m^{-2} irradiation and 30 s before ignition for the 51.5 kW m^{-2}

irradiation. Ignition was based on visual observation of a sustained flame and the cessation of flashing. The heat flux measurements showed that the side region receives about 95% of the heater irradiation that the center receives, in agreement with previous measurements [76,77]. Fig. 8 shows total heat flux measurements for PMMA under 51.5 kW m^{-2} irradiation, after ignition, as an example. For use in modeling, flame heat flux was averaged for an interval in time. Flame heat flux was averaged from the start of full surface burning, which was determined visually from the video recording, to the point when 50% of the sample was burned or to when a significant drop in heat flux was seen, whichever occurs first. It was assumed that the drop in heat flux was due to the formation of deposits (soot and condensed pyrolyzate) which were found covering the heat flux gauge surface after the conclusion of tests. Additional measurements using protective caps, briefly discussed in section 3.2, indicated that during the time periods selected to obtain the flame heat flux data, the impact of the deposits was minor.

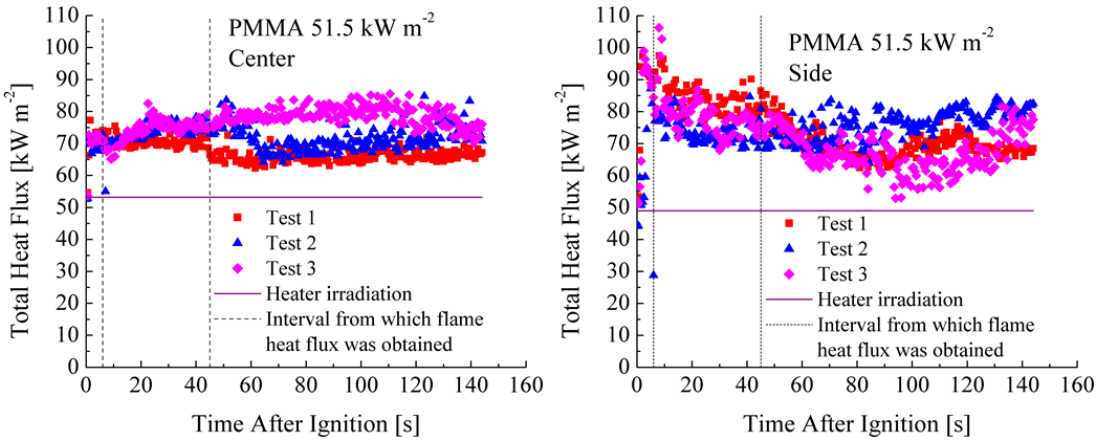

Fig. 8. Measured total heat flux in the center (left plot) and side (right plot) of PMMA samples under 51.5 kW m^{-2} irradiation. Shown is the irradiation of the heater as well as the interval from which flame heat flux was obtained. Notice that the irradiation for the side region is slightly lower than that of the center region.

Heat flux uncertainty was taken as two standard deviations of the mean plus the 3% systematic uncertainty of the heat flux gauge calibration. Fig. 9 gives the average flame heat flux for HIPS, PBT/GF/DEPAL, PMMA, and POM in both measured locations. For PMMA and POM, both high and low irradiation experiments yielded similar flame heat flux values, in agreement with past observations [5,23,27,35]. Video recording also showed that differences in irradiation did not significantly affect the structure of the base of the flame. Thus, flame heat flux measurements were averaged together from both irradiation conditions before further analysis.

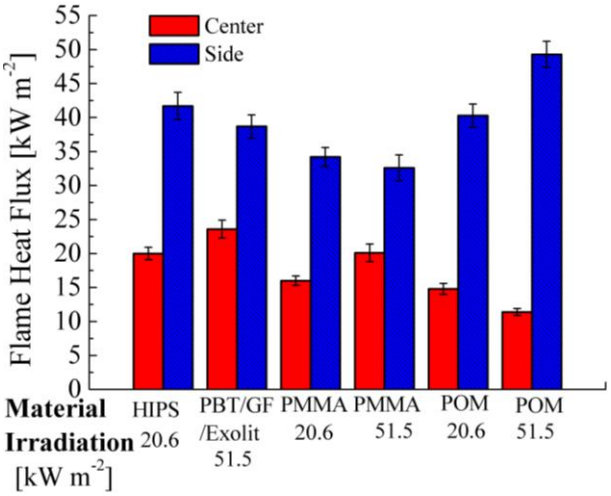

Fig. 9. Flame heat flux measurements for the two measurement locations: center (red) and side (blue) for HIPS, PBT/GF/DEPAL, PMMA, and POM.

Table 7 summarizes the flame heat flux values of this work and those found in the literature. Beaulieu et al. [27] measured flame heat flux in sample centers using water-cooled Schmidt-Boelter heat flux gauge during tests in the Advanced Flammability Apparatus (AFM) [27], which was similar to the cone calorimeter. Heat flux was measured for different environmental oxygen concentrations and sample diameters. This work's center measurements for PMMA and POM are reasonably close to the values of Beaulieu et al. [27] (for 20.9 vol% O_2 and 10 cm diameter) and Kacem et al. [32]. At the side of the sample, measured flame heat flux is significantly higher than in the center. Leventon et al. [75] studied laminar wall flames which, although of different orientation, are laminar diffusion flames of similar appearance to the flames seen along the sides of the sample in a cone calorimeter. Leventon et al.

measured flame heat flux at the top of slabs of various heights with a water-cooled Schmidt-Boelter heat flux gauge. When comparing the heat flux measurements for HIPS, PMMA, and POM slabs 5 cm tall [75] – equal to the distance between the center and edges of a cone calorimeter sample – values are within 10%. The flame heat flux values determined by Stoliarov et al. [23] for PMMA and HIPS seem to underestimate the contribution of the flame. The data of Boyer [34] is lower than other reported values, but this value is the heat flux to a hot, burning surface and not to a cooled gauge. If one accounts for the re-radiative losses of the burning surface, estimated to be 7.3–13.6 kW m^{-2} using a surface temperature of 600-700 K [23] and an emissivity of one, the flame heat fluxes align more closely with the other values. Similarly, Galgano et al. [35] reported an average flame heat flux relative to a burning surface; the flame heat flux was averaged for the inner part of the sample, excluding the edges. If one accounts for re-radiative losses for the value provided by Galgano et al. [35], the resulting flame heat flux lies between the current center and side measurements, reasonable since it was averaged across the surface.

Table 7. Comparison of flame heat flux [kW m^{-2}] values from the literature and this work

HIPS	PMMA	POM	PBT/GF/ DEPAL	Geometry	Heat flux relative to	Source
20.0 ± 0.9	16.9 ± 0.7	12.2 ± 1.3	23.6 ± 1.3	Center in Cone	Cold heat flux gauge	This work
24	12	–	–	Whole surface in Cone (averaged)	Cold heat flux gauge	[23]
–	20	11	–	Center in AFM	Cold heat flux gauge	[27]
–	23.5 ± 4.5	–	–	Center in Cone	Cold heat flux gauge	[32]
11-12	5-7	–	–	Whole surface in Cone (averaged)	Burning surface	[34]
–	17.5	–	–	Inner part in Cone (averaged)	Burning surface	[35]
41.7 ± 2.0	33.6 ± 1.2	47.1 ± 1.8	38.7 ± 1.7	Side in Cone	Cold heat flux gauge	This work
37	35	48	–	Vertical slab	Cold heat flux gauge	[75]

3.6 Analysis of cone calorimeter measurements

3.6.1 Flame heat feedback model of the two zones

As was shown in Fig. 9, the side flame heat fluxes are significantly greater than those measured in the center for all tested materials and all levels of irradiation. This agrees with previous findings for PMMA [30,34] and for HIPS [34]. Thus, flame heat flux must be treated separately for the center and the side regions of the sample. The

most straightforward approach is to define two zones, one for the center and one for the side, and to assume uniform conditions within each zone. The approach to divide the two zones will be discussed later in this section.

Equally important as the magnitude, is the nature of flame heat feedback, i.e. what portion is radiative and what portion is convective. Visual observations of HIPS, PMMA, and POM flames illustrate that the shape of the flame base does not depend significantly on material or irradiation. The base of the flame, not the tip, is most responsible for radiative exchange of the flame to the surface; thus, if the shape of the base of the flame is approximately constant, the only variable affecting radiative flame heat flux to the surface is the portion of the heat release in the form of radiation, which defines the radiative fraction. Therefore, it was hypothesized that the radiative flame heat flux would scale linearly with a material's radiative fraction. In this work, the radiative fraction was defined as the radiative heat release divided by the effective heat release and thus the values used may be larger than those which were reported per complete heat release. Further observations of the flames reveal that the flames are thin at the sides of the material; additionally, the view factor between the thicker flame in the center and the side of the material is small. It was hypothesized that the radiative flame heat flux is very small in the side zone. To evaluate these hypotheses, center and side flame heat flux measurements for HIPS, PMMA, and POM were plotted versus

radiative fraction [75] as shown in Fig. 10; PBT/GF/DEPAL was excluded since its radiative fraction is unknown. The data in Fig. 10 support both hypotheses. The flame heat flux at the side shows no dependence on radiative fraction, supporting the hypothesis that the flame is weakly radiative near the edges; this work assumed that the flame is wholly convective in the side zone. Flame heat flux was linearly related to radiative fraction for the center data. From the hypothesis, the product of the slope and radiative fraction gives the radiative flame heat flux. The intercept represents a convective flame heat flux because a radiative fraction of zero would imply zero heat release by radiation and by extension, zero radiative heat flux.

The flame temperature must also be determined for the creation of the models; this work assumed that the maximum temperature of the flame is the most appropriate choice. The flames in the cone calorimeter are non-stretched, laminar, diffusion flames whose maximum temperatures have been shown to be within 100–200 K of the adiabatic flame temperatures [78]. Thus, this work will approximate the maximum flame temperature as the adiabatic flame temperature. This assumption will be examined later in modeling. To generalize the model, the adiabatic flame temperatures for stoichiometric, fuel-air mixtures of pyrolyzates of eight different thermoplastics [75], which were calculated using heats of combustion measured in cone calorimetry, were averaged to determine the flame temperature, T_f = 2150 K.

To enable predictions, the convective and radiative flame heat fluxes determined for the materials were generalized such that the models can be applied to untested materials and materials with unknown radiative fraction. The radiative flame heat flux was generalized by assuming an average radiative fraction of 0.35, giving a generalized radiative flame heat flux of 9.5 kW m^{-2}. The convective flame heat flux was generalized in two steps. First, the side flame heat flux was averaged from the values for PMMA and HIPS, but excluding POM because its absence of soot can result in unusually higher heat flux measurements [75]. Second, convective heat transfer coefficients were determined for each zone by dividing the convective flame heat fluxes by the temperature difference between the flame and the heat flux gauge (291 K). Note that any blowing effect (reduction in convective heat transfer due to the outward flux of gaseous pyrolyzates of a burning surface) [79,80] was neglected because a previous study on flame heat feedback [81–83] of laminar flames on polymeric solids found it had only a minor impact on the heat transfer. Additionally, the study found that existing theory to correct for the blowing effect drastically overestimated its impact [81], so no correction was used in this work. Generalized convective flame heat flux was defined in terms of these convective heat transfer coefficients, the flame temperature, and a variable surface temperature, T_s.

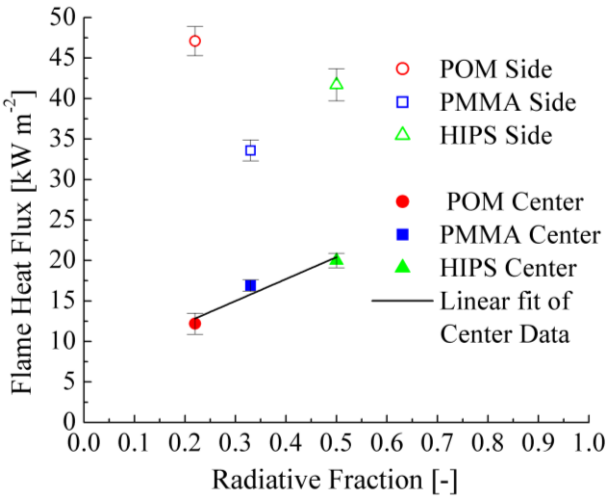

Fig. 10. Center (filled symbols) and side (open symbols) flame heat flux versus radiative fraction. The center data shows a linear relationship with radiative fraction while the side data does not.

Table 8 summarizes the flame heat flux models for the center and side. It is worth noting that when T_s is equal to a typical pyrolysis temperature (~700 K), the center flame model calculates radiation as 64% of the flame heat flux to the surface; this is reasonably close to previous measurements by Kacem et al. [32] who found ~80% radiation.

Table 8. Flame models for the center and side zones

	Center Zone	Side Zone
Radiative flame heat flux [kW m^{-2}]	9.5	0
Convective flame heat flux [kW m^{-2}]	$3.7 \times 10^{-3}\,(2150 - T_s)$	$20 \times 10^{-3}\,(2150 - T_s)$

Each zone now has its conditions, but the boundary dividing the zones has not yet been defined. With only two measurement points, the transition from side zone to

center zone is unknown experimentally. However, the transition can be determined by estimating the convective contribution of the flame across the sample using previously developed heat transfer correlations. The purpose of this analysis is to delineate where on the sample, the radiative flame heat flux is minor relative to the convective flame heat flux, as was observed for the side measurements.

Convective flame heat flux from the flame to the surface was approximated from the edge to the center assuming T_f = 2150 K, T_s = 700 K. The convective heat transfer coefficient, h [W m^{-2} K^{-1}], was computed for varied distance inward from the sample's edge, l [m]. A heat transfer correlation for natural convection above a horizontal, heated plate [84] was used to find the spatially-averaged convective heat transfer coefficient, $\bar{h}$, from which h can be determined by the relationship given in Equation (8). Equation (8) was computed numerically via a second order central difference scheme. The correlation [84], when simplified, is given by Equation (9). The characteristic length was defined as a ratio of area to perimeter [84]. Assuming square geometry, the characteristic length is *l/4*. Kinematic viscosity, ν [m^2 s^{-1}], thermal diffusivity, α [m^2 s^{-1}], and Prandtl number (Pr) were obtained through interpolation of tabulated values for air [85] at a mean temperature between T_f and T_∞ = 300 K. Thermal conductivity, k [W m^{-1} K^{-1}], was interpolated [85] for air at a mean

temperature between T_f and T_s. For verification, $\bar{h}$ was computed for the entire sample (l = 0.1 m) and found to be 10.5 W m^{-2} K^{-1}, which is within 5% of previous calculations [5,23,86].

$$h = \frac{d}{dl}\left(l\bar{h}\right) \tag{8}$$

$$\bar{h} = \frac{k}{l/4}\left[\left(1.4\left[ln\left(1+\frac{1.4\left[1+\left(\frac{0.492}{Pr}\right)^{\frac{9}{16}}\right]^{\frac{4}{9}}}{(0.835)(0.671)\left(\frac{g\left(T_f-T_\infty\right)\left(\frac{l}{4}\right)^3}{\frac{1}{2}\left(T_f+T_\infty\right)\upsilon\alpha}\right)^{\frac{1}{4}}}\right)\right]^{-1}\right)^{10} + \left(0.14\left(\frac{1+0.0107\,Pr}{1+0.01\,Pr}\right)\left(\frac{g\left(T_f-T_\infty\right)\left(\frac{l}{4}\right)^3}{\frac{1}{2}\left(T_f+T_\infty\right)\upsilon\alpha}\right)^{\frac{1}{3}}\right)^{10}\right]^{\frac{1}{10}} \tag{9}$$

Fig. 11 shows the estimated convective flame heat flux versus position as well as convective flame heat flux derived from the measurements described in Table 8. The convective flame heat flux computed based on the correlation underestimates the convective flame heat flux at the side and overestimates the convective flame heat flux in the center. The transition between zones was chosen to occur where the convective heat flux was twice that of the center radiative heat flux (9.5 kW m^{-2}). Such a conservative criterion was chosen because it is to define the zone where the radiative

flame heat flux can be neglected. The criterion estimates the side zone as 2.3 cm inwards on all sides, making the center zone a square with 5.4 cm sides, as illustrated in Fig. 12. In terms of fractional area, the center zone is 29.2% of the area and the side zone is 70.8%. Fig. 12 also shows that the placement of the heat flux gauges also lies roughly in the middle of the derived zones.

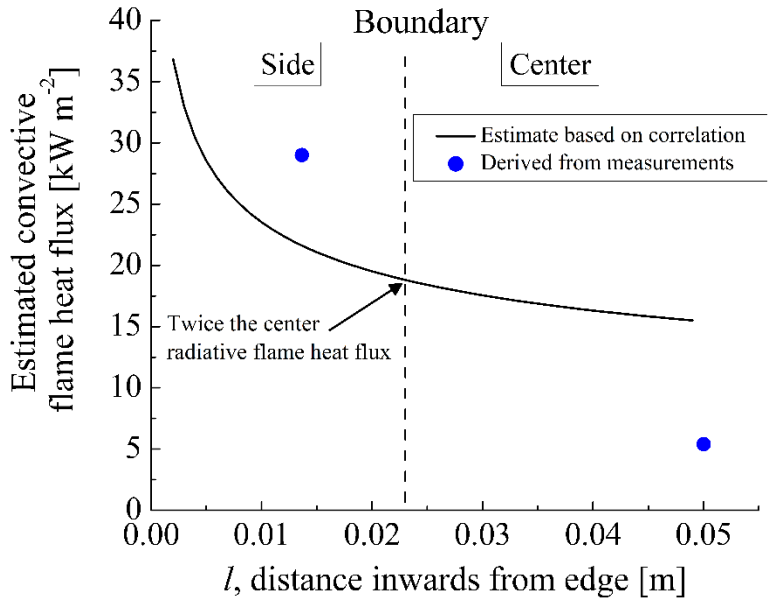

Fig. 11. Estimated convective flame heat flux as a function of distance from the edge.

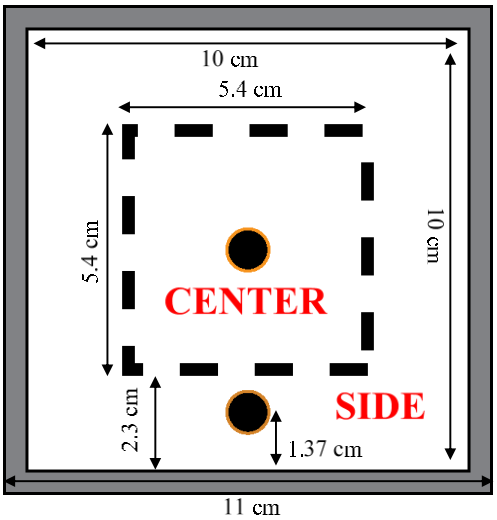

Fig. 12. Illustration of the two zones marked by the dashed boundary, determined based on the estimated convective flame heat flux relative to the center radiative flame heat flux. The heat flux gauges are seen to align in the middle of the hypothesized zones.

3.6.2 Boundary conditions for the two zones

The boundary conditions defining the flame heat fluxes were developed in section 3.6.1. Boundary conditions for the top surface prior to ignition need to be defined. Radiative boundary conditions are the irradiation from the conical heater, q''_{cone}. q''_{cone} was not reduced after ignition because absorption by the flame was not included for reasons discussed in section 3.5.3. Convective boundary conditions for the exchange between the heated sample surface and the cooler surrounding air assumed T_s = 500 K and T_∞ = 300 K, respectively. The convective heat transfer coefficient was found spatially using Equations (8) and (9), except T_f was replaced with T_s. Additionally, all fluid properties were interpolated for air [85] at a mean temperature

between T_s and T_∞. The convective heat transfer coefficient was averaged for each zone, giving $\bar{h}$ = 9.0 and $\bar{h}$ = 12.7 W m^{-2} K^{-1} for the center and side zone respectively. The calculated $\bar{h}$ values are supported by observations of the side igniting 3 ± 1 s later than the center [71]; reduced irradiation and increased convective losses would explain the delay in ignition. Table 9 summarizes the top boundary conditions for each zone before and after ignition. Note that in the model, T_s is not a prescribed value but is computed by the pyrolysis model (ThermaKin2DS).

Table 9. Top surface boundary conditions for each zone before and after ignition in ThermaKin2Ds modeling

Center zone (square with 5.4 cm sides)		**Side zone** (region outside central zone)	
	Before Ignition (non-flaming)	After Ignition (flaming)	Before Ignition (non-flaming)	After Ignition (flaming)
Convective [kW m^{-2}]	9.0×10^{-3} (T_s - 300)	3.7×10^{-3} (2150 - T_s)	12.7×10^{-3} (T_s - 300)	20.0×10^{-3} (2150 - T_s)
Radiative [kW m^{-2}]	q''_{cone}	q''_{cone} + 9.5	0.95 q''_{cone}	0.95 q''_{cone}

The criterion for ignition was based upon a virtual heat release rate. The virtual heat release rate is the product of a material's critical mass flux and its effective heat of combustion. Lyon et al. [87] found that the virtual heat release rate is a constant 21 ± 6 kW m^{-2} for a variety of solid fuels at flashpoint, based on calculations using published values. This was later confirmed experimentally by Lundström et al. [88]. Lundström et al. used a porous burner and measured critical mass flux at flash point for

fuel-inert gas mixtures with different heats of combustion, representing a range of solids. They also found a constant virtual heat release rate of 21 ± 3 kW m^{-2} [88]. Ignition in the simulation was defined to occur once the virtual heat release rate, calculated by summing up the mass flux of each gaseous pyrolyzate multiplied by its corresponding heat of combustion, was equal to or greater than 21 kW m^{-2}. For HIPS, PMMA, and POM, thermal decomposition of these materials is given by a simple single-step reaction [64] so only a single gas species was considered with its heat of combustion equal to its effective heat of combustion given in section 3.5.1. For PBT/GF, PBT/GF/DEPAL, and OSB, these produce multiple gas species whose heats of combustions are not necessarily equal to one another nor equal to the effective heat of combustion. Thus, for these materials, the heats of combustion were taken from past measurements using MCC experiments ([89] for PBT blends, [68] for OSB) which can determine individual gaseous pyrolyzate heat of combustion. Ignition of the side zone was prescribed to occur within 3 ± 1 s after center ignition to approximate flame spread over the material surface based on experimental observations [71]. Separate one-dimensional simulations were conducted for each zone.

3.7 ThermaKin2Ds simulation results and model validation

All materials and test conditions were simulated including even those which were likely impacted by absorption of irradiation from the heater by the polymer flame such as HIPS and PBT/GF under 51.5 kW m^{-2} irradiation. This was done to investigate the impact of neglecting the absorption of irradiation on predictions of HRR. Fig. 13 shows the experimental HRR, simulated center and side HRR curves, and the final model for PMMA under 20.6 kW m^{-2} irradiation. Also depicted is the final model corrected for oxygen effects, to be discussed in section 3.7 and 3.8. The side zone simulation tends to overpredict HRR while the center zone simulation underpredicts the HRR. The final model is a linear, area-weighted combination of the simulated HRR of each zone with a weight of 0.292 for the center and 0.708 for the side. The area-weights were based on the boundary for the two zones derived in section 3.6, not based on optimization. The final model better predicts HRR than either the center or side simulations separately.

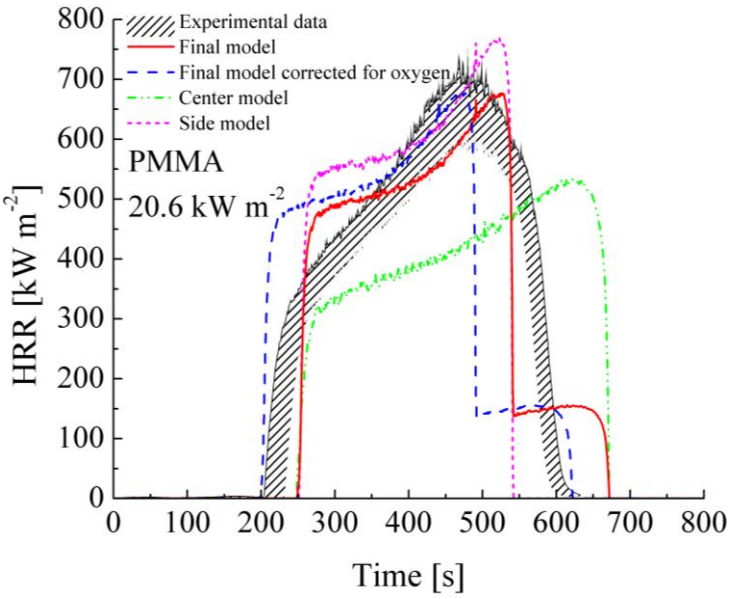

Fig. 13. Center and side simulated HRR compared with the final model and the experimental HRR for PMMA under 20.6 kW m^{-2} irradiation.

Therefore, only simulation results from the final model are given for the rest of the materials as shown in Fig. 14 for 20 kW m^{-2} irradiation results and Fig. 15 for 51.5 kW m^{-2} irradiation results; for comparative purposes, the same y-axis is used for all plots. The simulated HRR curves show qualitatively, good agreement with experimental results; the difference between the red and dashed, blue curves will be discussed later in section 3.8. The shape and width of the model curve (steady burning duration) also matches the experimental data reasonably well for all levels of irradiation and all materials. Additional simulations using PMMA were later conducted wherein the actual laminar flame temperature (1981 K [90]) and re-calculated convective heat

transfer coefficients were used in the flame models; differences in HRR from the simulations using adiabatic flame temperature were 4% or less, on average, justifying the approximation of the adiabatic flame temperature for the maximum flame temperature.

To quantify the ability of the model to predict experimental data, time to ignition, average heat release rate (AHRR) and peak heat release rate (PHRR) were determined for each test and for each simulation. The AHRR was determined by integrating the HRR via the trapezoidal method from ignition to extinction and dividing by this length of time. The PHRR was the maximum HRR value found after applying a 10 s moving average to reduce the effects of noise in the data. Table 10 summarizes the AHRR and PHRR determined experimentally (averaged from all trials) and from the model. The model predicted well both AHRR and PHRR for several materials. Error in predicted AHRR ranged 2.6–34.4% with an average error of 17.1%. Error in predicted PHRR, ranged 1.4–25.2% with an average error of 14.7%. When compared to Boyer, who also simulated cone calorimetry of PMMA and HIPS, error in predicted HRR for HIPS is improved and is comparable for PMMA [34]. Error in predicted AHRR is slightly larger in this work. Considering the simplicity of the model, the performance is quite good. Additionally, to the author's knowledge, no published model has performed as well for a range of materials and heat fluxes.

The results for HIPS, PBT/GF, and PBT/GF/DEPAL merit further discussion. Regarding HIPS, it is interesting to see that when absorption of the irradiation is ignored in the model at 51.5 kW m^{-2} irradiation, the error increases from 16.7% to 24.1% for AHRR and from 1.4% to 19.7% for PHRR. Thus, even when absorption is neglected the model performs reasonably well for HIPS. However, predictions at even higher levels of irradiation may be more problematic due to potentially increased absorption. The model significantly underpredicts HRR for PBT/GF. This is likely due to a deficiency of the pyrolysis model for PBT/GF at high levels of irradiation. The pyrolysis model underpredicted peak MLR by about 16% for CAPA experiments conducted under 60 kW m^{-2} irradiation; the model of this work underpredicts PHRR by about 22%, which is comparable. Additionally, the model does not fully capture the reduction in HRR when DEPAL is added. Experimentally, adding DEPAL reduced AHRR by 39% and PHRR by 50% while the model predicts a reduction of 22% and 21%, respectively. However, the model does not explicitly include the gas-phase effects of DEPAL [91,92]; it only considers the slight change to the gasification rate and the reduction in effective heat of combustion (which had been found to be only 10%, see section 3.5.1) which would explain why it underestimates the reduction.

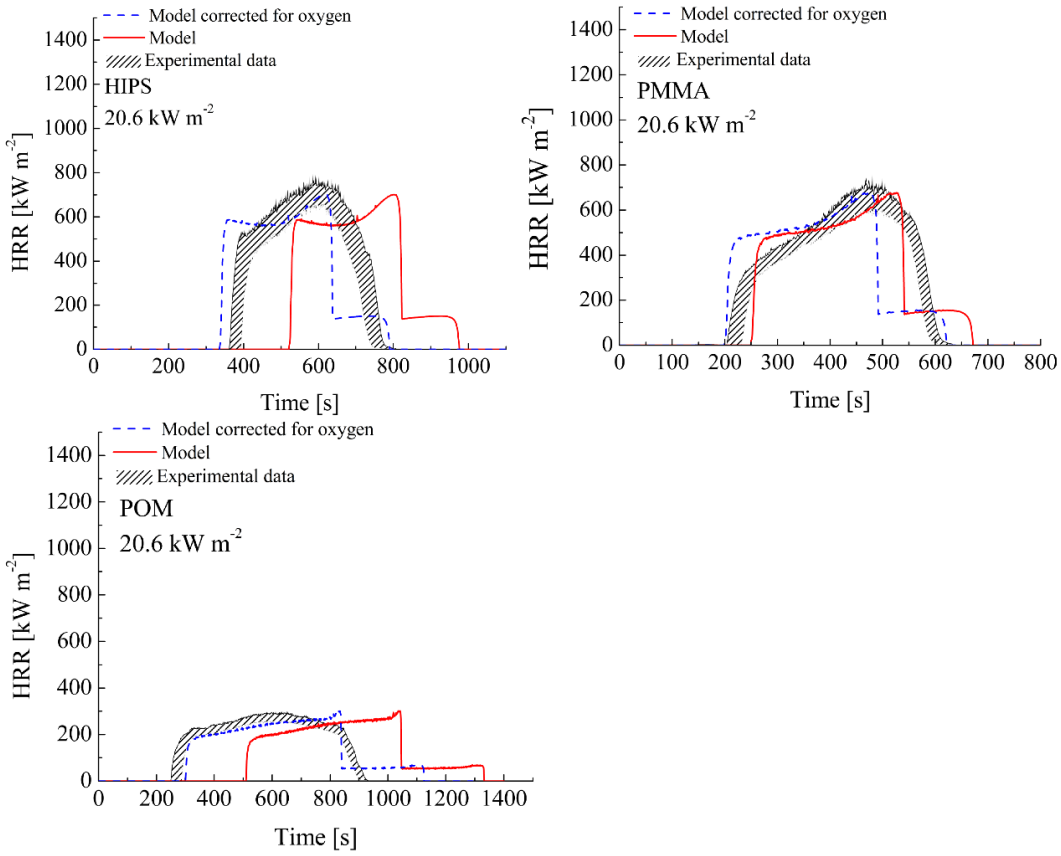

Fig. 14. HRR profiles of experiments and model for HIPS, PMMA, and POM under 20.6 kW m^{-2} irradiation. The blue, dashed curves are a correction to the ignition time for the effects of oxygen.

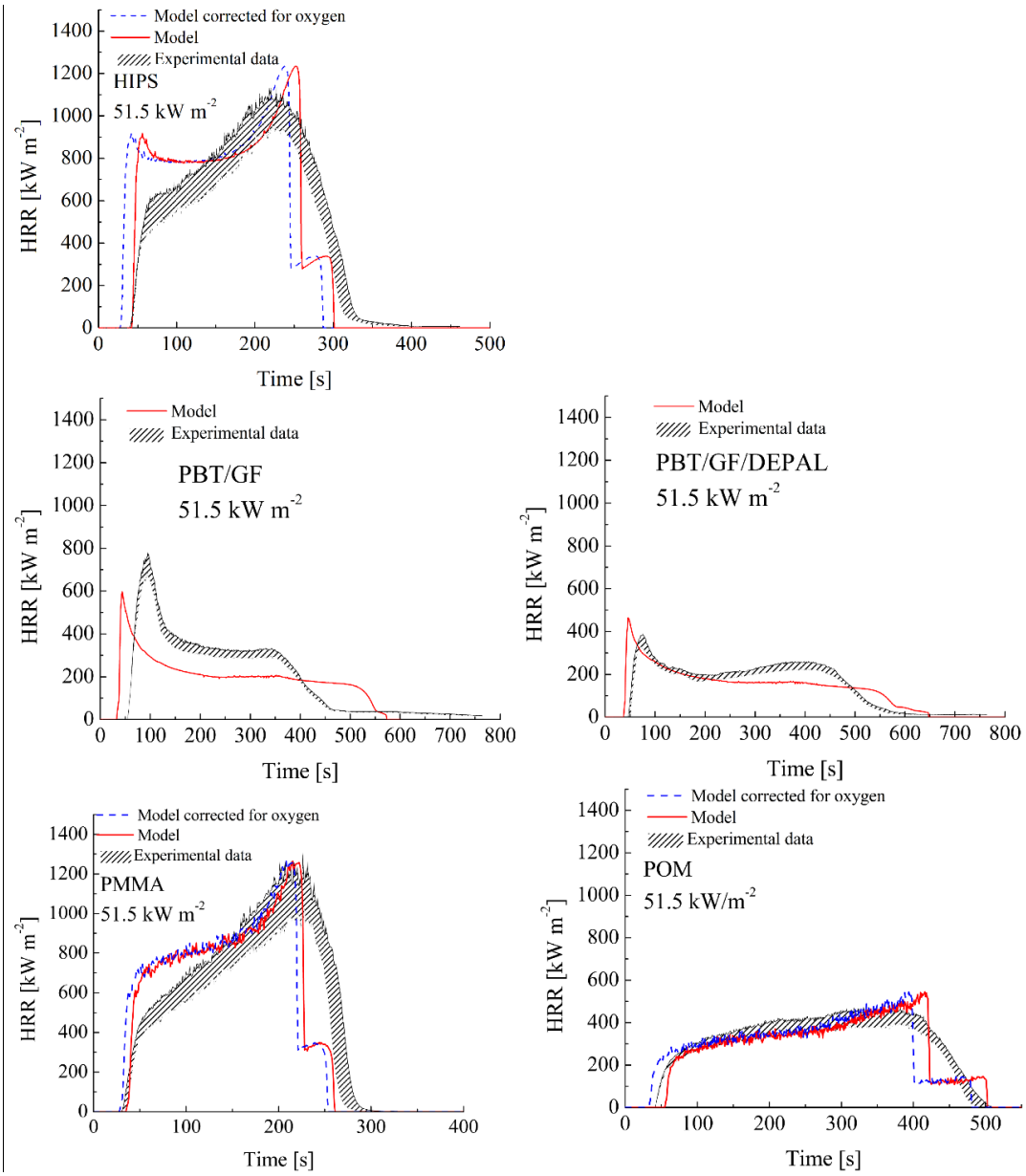

Fig. 15. HRR profiles of experiments and model for HIPS,PBT/GF with and without DEPAL, PMMA, and POM under 51.5 kW m^{-2} irradiation. The blue, dashed curves are a correction to the ignition time for the effects of oxygen.

Table 10. Comparison of experimental and modeled AHRR and PHRR

Material name	Irradiation [kW m^{-2}]	**AHRR [kW m^{-2}]**			**PHRR [kW m^{-2}]**		
		Exp	Model	Error [%]	Exp	Model	Error [%]
HIPS	20.6	525 ± 33	438	16.7	710 ± 47	700	1.4
	51.5	622 ± 50	773	24.1	1022 ± 70	1223	19.7
PBT/GF	51.5	321 ± 18	211	34.4	712 ± 49	554	22.2
PBT/GF/ DEPAL	51.5	196 ± 14	164	16.3	353 ± 28	435	23.4
PMMA	20.6	463 ± 36	413	10.8	656 ± 60	674	2.8
	51.5	702 ± 57	777	10.5	1089 ± 118	1248	14.6
POM	20.6	219 ± 15	172	21.3	276 ± 19	299	8.2
	51.5	328 ± 23	319	2.6	425 ± 32	532	25.2

Uncertainty in the experimental AHRR and PHRR was taken as half the range of the data plus the 5% systematic uncertainty in HRR measurement, giving 6–8% uncertainty for AHRR and 7–11% for PHRR. Thus, the model is almost within experimental uncertainty. There is also the small artifact at the end of the modeled HRR curves. The rapid drop is due to the difference in burning duration of the two zones since flame spread is not modeled explicitly. This artifact is tolerable for the simplicity of the model and savings in computational cost.

3.8 Oxygen effects on ignition in cone calorimetry simulations

As was shown by the red curves in Fig. 14, time to ignition at low irradiation was not successfully predicted, possibly because of surface oxidation. The oxygen present at the sample's surface prior to ignition might be sufficient to enhance decomposition of polymeric material, resulting in shorter ignition times; this behavior is not reflected in the pyrolysis parameters sets. The pyrolysis parameter sets [59,62–64,68,69] were developed for anaerobic conditions, which exist for most of the cone calorimeter test because the flame sheet prevents oxygen from reaching the surface.

TGA tests were conducted to explore the possibility of oxygen enhancing the decomposition and impacting the time to ignition for HIPS, PMMA, and POM; PBT/GF, PBT/GF/DEPAL, and OSB were excluded since they ignited quickly in all tests (see section 3.9 for OSB results) which allowed little time for oxygen to have an impact. TGA results in pure nitrogen and in air (21 vol% O_2) are given in Fig. 16. In the presence of oxygen, decomposition was enhanced and began at a lower temperature, as shown by a shift to the left by the tests in air relative to the tests in nitrogen.

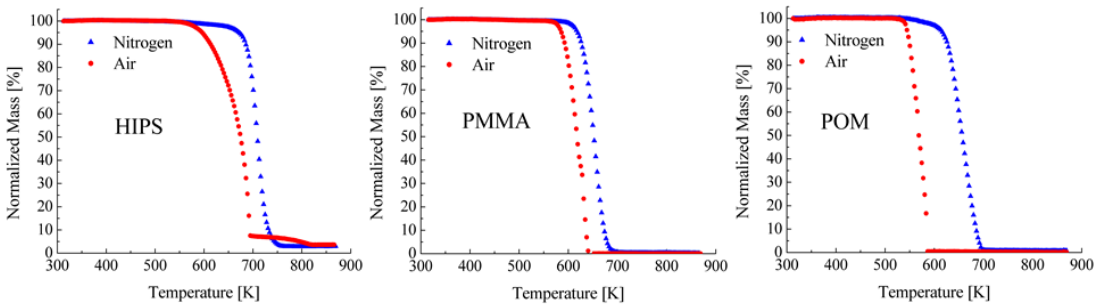

Fig. 16. Normalized mass curves versus temperature of HIPS, PMMA, and POM in nitrogen and air environments. The sample mass data were normalized by intial mass.

It was hypothesized that thermally thick ignition theory could relate the shift in decompostion temperature to a corresponding shift in ignition time, as a first order correction. The samples do not fully satisfy thermally thick assumption for low irradiation; however, when selecting between thermally thin and thermally thick, thermally thick theory is much more applicable. Equation (10) describes time to ignition for a thermally thick solid [93].

$$t_{ig}{}^{-0.5} = \left(\frac{4}{\pi}\right)^{0.5} \frac{q''_{cone} - q''_{loss}}{(k\rho c)^{0.5}(T_P - T_\infty)} = \left(\frac{4}{\pi}\right)^{0.5} \frac{1}{TRP}\left(q''_{cone} - q''_{loss}\right) \qquad (10)$$

Where t_{ig} is the ignition time [s], q''_{cone} is the irradiation from the heater [kW m^{-2}], q''_{loss} includes radiative and convective losses between the sample surface and surroundings [kW m^{-2}], $k\rho c$ is a material's thermal inertia [kW^2 s m^{-4} K^{-2}], a product of thermal conductivity, density, and specific heat. T_p is the ignition temperature [K], which was assumed to correspond to the temperature of 5% mass loss in the TGA tests.

The ignition temperature was determined to be 545, 583, 597 K in air ($T_{p,air}$) and 615, 619, 673 K in nitrogen ($T_{p,nitrogen}$) for HIPS, PMMA, and POM, respectively. It is worth noting that the ignition temperature is somewhat sensitive to the irradiation (Snegirev, Kuznetsov, & Markus, 2017) but such effect was neglected here. T_∞ is the ambient temperature, assumed to be 300 K.

By plotting ${t_{ig}}^{-0.5}$ determined from the simulations versus q''_{cone}, as shown in Fig. 17, the thermal response parameter for a nitrogen environment, $TRP_{nitrogen}$ [kW $s^{0.5}$ m^{-2}], and q''_{loss} were found from the slope and from the intercept, respectively, for each of the three materials analyzed. Subsequently, the thermal response parameter for an air environment, TRP_{air}, was calculated from Equation (11) using $TRP_{nitrogen}$ and the ignition temperatures.

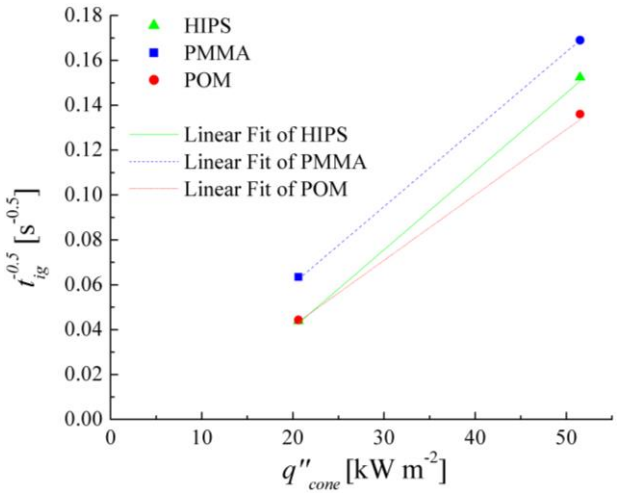

Fig. 17. Inverse-square of simulated ignition times versus irradiation to obtain thermal response parameter (slope) and heat losses (intercept).

$$\frac{TRP_{air}}{TRP_{nitrogen}} = \frac{T_{p,air} - T_\infty}{T_{p,nitrogen} - T_\infty} \tag{11}$$

Assuming that q''_{loss} is not significantly impacted by oxygen, the new ignition times were obtained by substituting TRP_{air} into Equation (10). The modeled HRR curves were shifted to these new ignition times and are shown as dashed, blue lines in Fig. 14 and Fig. 15. The correction successfully addresses the discrepancy in ignition times and strongly supports the hypothesis that surface oxidation is the cause. This correction provides a simple way to account for impact of oxygen on ignition without explicitly modeling the oxidation kinetics. Oxidation was investigated more rigorously in the following chapters.

3.9 Further validation of cone calorimeter model: Oriented strand board

To support other research efforts, cone calorimeter tests and simulations were performed for OSB. These results demonstrate the wider applicability of the empirical flame heat feedback model for simulating cone calorimetry. Cone calorimeter tests were performed in the manner described in Section 3.2. Tests were stopped 100 – 200 s after the cessation of flaming since smoldering was not a focus of this work. Simulations of cone calorimetry were performed in the manner described in section 3.3. The pyrolysis model was developed in a separate study [68,69]. The flame heat feedback parameters were assumed to be unchanged since the heat of combustion of OSB, ~13 kJ g^{-1} , is close to that of POM and the structure of the flame itself appeared similar to the polymer flames.

The experimental HRR and model predictions are shown in Fig. 18. The shaded area represents the range of the data plus 5% uncertainty. Interestingly, no correction had to be made to the ignition time predictions at the lower heat flux condition. Predictions are good overall for both heat fluxes. However, the first peak is overpredicted by the model. This may be due to incomplete combustion at early stages of the test. The heats of combustion, which are used to calculate HRR, were obtained from microscale combustion calorimetry which forces complete combustion [65]. Another possibility is that the experiment is that the HRR measurement is not

sufficiently fast to resolve the peak. The performance of the model suggests that it can be used in conjunction with pyrolysis models to predict the HRR of a wide range of materials, provided that the material's heat of combustion is sufficiently similar.

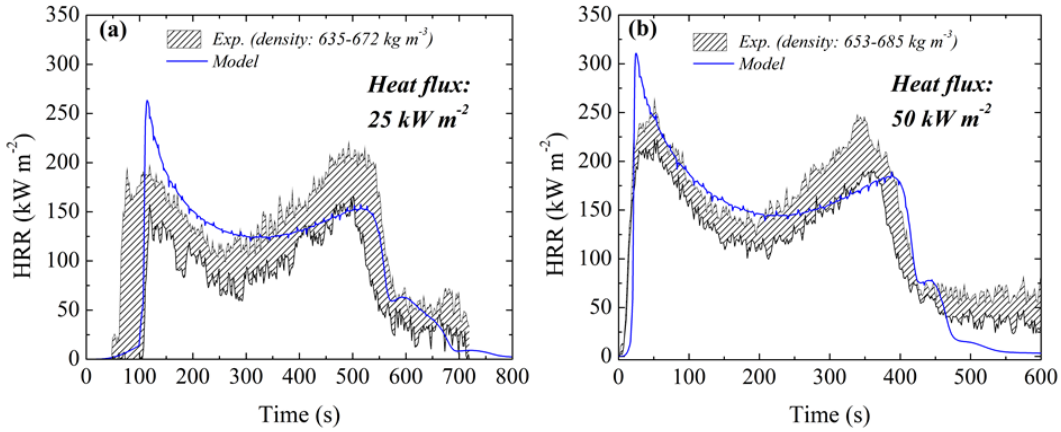

Fig. 18. Comparison between measured and simulated HRR of OSB in cone calorimeter tests performed at (a) 25 kW m^{-2} and (b) 50 kW m^{-2} of set radiant heat flux.

Chapter 4: UL-94V quantification and modeling using PMMA

The model's success in predicting HRR of cone calorimeter tests motivated investigation into another standard fire test, UL-94V. However, UL-94V is a more challenging scenario to quantify and model because of the spreading flame. Key quantities such at the temperature and heat flux of the burner flame as well as the heat feedback of the polymer flame were measured in UL-94V tests in several locations along the sample. A technique using an IR camera was developed to track the progression of flame spread. Simulations of the UL-94V test were performed and then compared with experimental flame length measurements.

4.1 Material and sample preparation

Clear, extruded poly(methyl methacrylate) (PMMA), 0.27 cm thick, was used to parametrize the UL-94V model; PMMA was selected for its well-defined pyrolysis properties [64] and because its flame heat feedback has been well characterized [75,83]. Rectangular bars with length of 12.5 ± 0.5 cm and width 1.3 ± 0.1 cm were cut from the polymer sheets in accordance with the UL-94V standard [12]. To investigate the edge effects, some of the rectangular bars were then insulated along the sides using pieces of Kaowool PM insulation board 0.32 cm thick glued on using small amounts of fast cure epoxy. The width of these insulation pieces was such that they were 0.05 ±

0.05 cm wider than the sample thickness. The insulation pieces are oriented so that the width of the insulation piece is in the same plane as the sample thickness direction. Some of the insulation was removed where the sample was clamped. Illustrations of representative samples are provided in Fig. 19. All samples were dried in a desiccator for a minimum of 24 hours before testing.

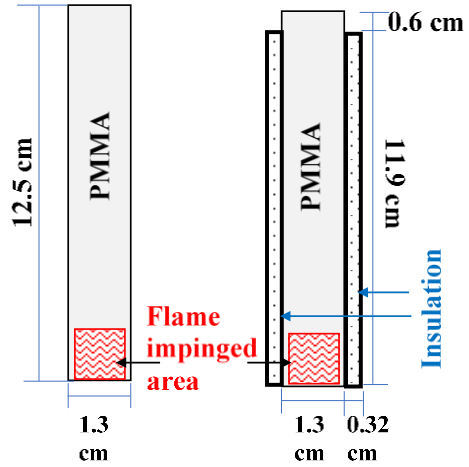

Fig. 19. Illustrations of a non-insulated PMMA sample (left) and an insulated PMMA sample (right). Illustrations are not to scale.

4.2 Test apparatus overview

An apparatus was constructed to conduct modified UL-94V (ASTM D3801 (E1354-16a, 2016)) tests and is depicted in Fig. 20. The burner is secured on a track for reproducible movement. The burner track and specimen holder are secured in place to a support table made of perforated steel sheet. Carbon fiber blankets on the sides ensure quiescent air. Laser sights are used to align the sample with respect to the burner.

Once aligned, the burner is moved away and ignited to produce a 20 mm tall methane-air premixed flame. Tests are then conducted in accordance with ASTM D3801 [12]. All UL-94V tests were filmed using a modified Nikon D800 DSLR camera with its internal infrared (IR) cut filter removed to expand its sensitivity into near IR and with an external 900 ± 10 nm bandpass filter in place. This wavelength was chosen to focus on emissions from soot [94] while also making the premixed burner flame effectively invisible to the camera so that only the flame fueled by the burning polymer is captured. The focal length of the lens was 18 mm, the aperture was f/3.5, the shutter speed was 1/30 s, the frame rate was 30 fps, the ISO was 125, and the focus mode was manual. The camera was positioned to provide a side view of the sample. A Sony Handycam HDR-CX199 camcorder was also used occasionally for observations of the sample front.

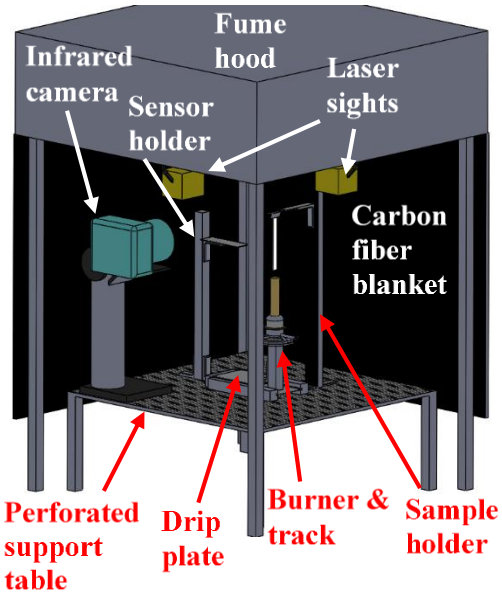

Fig. 20. Schematic of the apparatus used for UL-94V (ASTM D3801) tests.

4.2.1 Burner description and calibration

The burner used was manufactured in accordance with ASTM D5025 [95]. The burner was calibrated in accordance with ASTM D5207 for 20-mm flames [44]. ASTM D5207 stipulates that a copper slug with an embedded K-type thermocouple shall be suspended 10 mm above the burner and shall undergo a temperature rise from 100 ± °C to 700 ± 3 °C in 44 ± 2s of exposure to the burner. The burner met the temperature rise criterion repeatedly when the flow rate was increased slightly from 105 mL min^{-1} (recommended by the standard) to a flow rate 115 mL min^{-1}, as shown in Fig. 21. The flow rate was regulated by an Alicat MC-200SCCM-D mass flow controller.

Additionally, the visual flame height was 20 ± 1 mm when measured with a ruler for 115 mL min^{-1} but smaller for 105 mL min^{-1}. Furthermore, Downey found that when other operators were asked to re-create a 20 mm tall flame, the resulting flow rates were 118-197 mL min^{-1} with 166 mL min^{-1} being the average [38]. Downey compared the measured heat flux of the burner at 105 mL min^{-1} and 166 mL min^{-1} using a heat flux gauge embedded into an insulation piece shaped like a UL-94V sample; differences in heat fluxes were only 2-3 kW m^{-2} [38]. Thus, a flow rate of 115 mL min^{-1} reliably satisfies ASTM D5207 and any differences in heat flux between 115 mL min^{-1} and 105 mL min^{-1} flow rates are expected to be well within 2 kW m^{-2}, which are within the uncertainties of the heat flux measurements.

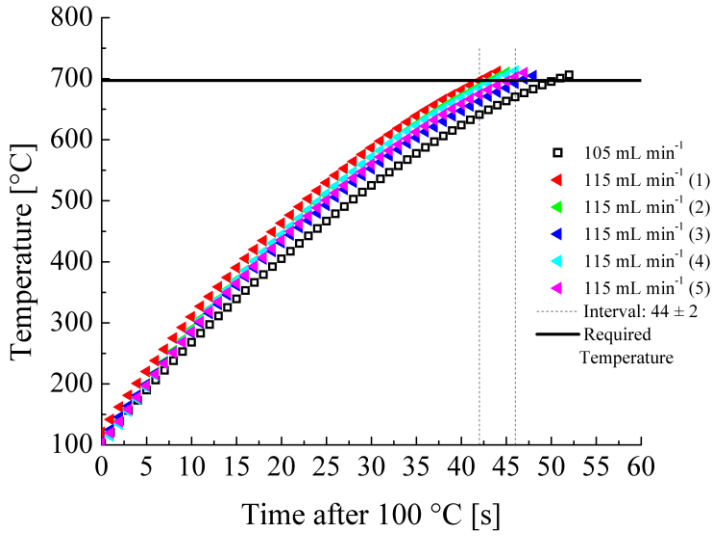

Fig. 21. Time-temperature curves for 105 mL min^{-1} gas flow rate and 115 mL min^{-1} gas flow rate. The former fails to pass while the latter satisfies the requirement several times.

4.3 UL-94V burner characterization

To characterize the UL-94V test, burner flame heat flux, temperature, and oxygen content were measured. These measurements were used to dictate the boundary conditions used in ThermaKin2Ds to more accurately simulate the UL-94V test.

4.3.1 Burner flame heat flux and temperature measurement

Heat flux was measured using a 0.95 cm or 0.64 cm diameter water-cooled Schmidt-Boelter heat flux gauge embedded in a piece of Kaowool PM insulation cut to approximate the sample size (12.5 cm long by 1.4 cm wide). The distance between the sample bottom and the middle of the sensor, y [cm], was varied from y = 0.55 to y = 7.80 cm; 3–6 measurements were performed at each position. The thickness of the insulation piece was 0.64 cm for measurements of $y \leq 1.5$ cm (for greater insulation of the gauge sidewall) and 0.32 cm otherwise. The face of the insulation piece was flush with the center of the burner, representing an infinitely thin sample. The heat flux gauge was painted with high emissivity black coating and calibrated against a reference traceable to the National Institute of Standards and Technology (NIST). The sensor was repainted and recalibrated before every measurement. For most measurements, the 0.95 cm diameter heat flux gauge was used. The 0.64 cm diameter heat flux gauge was used to confirm that the sensor size has no impact on the results and to determine the heat

flux near the sides of the sample by shifting the location of the gauge so that its center was 0.23 cm to the right of the sample centerline (the outer edge of the heat flux gauge was ≈ 0.15 cm from the side of the sample). The gauge signal was recorded at a rate of 2 Hz. Fig. 22 depicts the overall geometry of the heat flux and temperature measurements. For the temperature measurements, a 76 μm wire-diameter R-type thermocouple, housed in a ceramic tube, was used. Temperatures were measured as a function of vertical distance from the bottom of the sample, y, and as a function of distance normal to the sample surface, x [cm], by using a two-dimensional translation stage. y ranged from 0.25 to 4.20 cm while x varied from 0.00 to 0.60 cm in 0.05 cm increments. The temperature signal was recorded at a rate of 3 Hz.

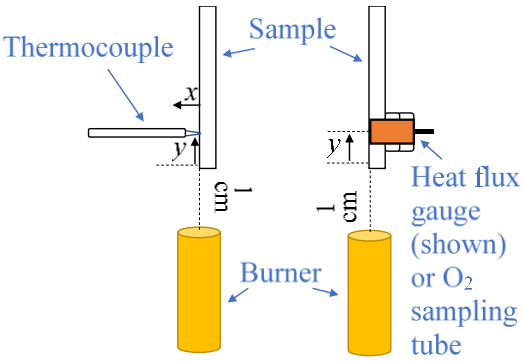

Fig. 22. Schematic of the heat flux and temperature measurements viewed from the side. The sample was usually made of Kaowool PM insulation but for some measurements it was PMMA.

4.3.2 Sample surface oxygen content beneath burner flame

Oxygen content was measured since the burner flame is premixed and oxygen is known to enhance PMMA decomposition [50] and potentially the other materials studied as well. Burner gases were sampled through a ceramic tube with 0.16 cm inner diameter at a flow rate of 100 mL min^{-1} via a diaphragm pump; the resulting velocity was much smaller than the burner flow velocity, minimizing disturbance of the flame. Oxygen content was measured using a Pm1111E paramagnetic oxygen sensor and its signal was recorded at a rate of 2 Hz. Prior to the sensor, gases pass through Drierite to remove any moisture to protect the sensor from damage. Steady-state oxygen concentration was determined by sampling for about 4 minutes. Like the heat flux gauge, the gas sampling tube was inserted through an insulation piece and made flush with its surface for varied y, ranging from 0.2 to 2.2 cm. Similarly, oxygen content was also measured at the surface of burning PMMA samples to confirm that no oxygen is present underneath the diffusion flame as was observed in earlier studies [13]; these measurements were conducted at y = 1 cm along the centerline and at y = 1.5 cm along the centerline and 0.35 cm to the right of the centerline.

4.4 TGA in inert and oxygenated environments

Thermogravimetric analysis was performed for each material mentioned in an inert (100 vol% N_2) environment and an oxygenated environment (5 vol%, balance N_2) to determine if the oxygen content within the burner gases significantly enhances thermal decomposition. The 5 vol% O_2 atmosphere was created by flowing N_2 at 57 mL min^{-1} and flowing O_2 at 3 mL min^{-1}. For PMMA, an additional test was conducted in a 7 vol% O_2 atmosphere which was created by flowing N_2 at 53 mL min^{-1} and flowing O_2 at 4 mL min^{-1}. N_2 was flowed at 50 mL min^{-1} for the 100 vol% N_2 atmosphere. Samples were 4–10 mg of PMMA in both solid pieces and powder (preliminary experiments) to investigate the effect of surface area on mass loss in a slightly oxygenated environment; surface area was considered because the literature review found that oxygen acts primarily at the surface for PMMA decomposing in air [50–53]. The samples were heated at rate of 10 K min^{-1} and their mass was recorded as a function of time and temperature. An alumina crucible was used for all tests since the platinum crucible was found to have a catalytic effect resulting in noise in the mass data.

4.5 Numerical simulation of TGA

One-dimensional geometry ThermaKin2Ds was used to model the TGA experiments. Samples were assumed to be thermally thin and were represented by a single element. The element was forced to follow the experimental temperature program by defining a very high convective coefficient at the boundary (100 kW m^{-2} K^{-1}). The heating rate was defined by an exponentially decaying sinusoidal function to capture the experimental heating rate [96]. Gaseous components were assumed to leave the element instantaneously.

4.6 IR flame length measurement from videos

Flame length of buoyancy-driven, laminar wall flames is known to increase with increasing heat release rate [97,98] and was used in this work to track dynamics of fire growth on PMMA samples. In this study, monochromatic IR images were analyzed to track the hot gases and soot of the flame. Experimental flame length was defined as the vertical distance between the tip of the flame and the initial base of the flame as captured in the IR images. Henceforth, this quantity shall be referred to as IR flame length. IR flame length data were used to evaluate the simulation and were also used to identify the position of the PMMA flame relative to the heat flux gauge for determination of the PMMA flame heat flux. IR flame length was chosen over MLR

because it was a noninvasive measurement that provided a well resolved early spread dynamics.

4.6.1 Overview of IR flame length measurement process

During image processing, each frame was extracted from the 30 fps videos collected with the IR camera and then read in MATLAB. Images were converted into grayscale using an unweighted average of the RGB pixel intensities. Next, each grayscale frame was binarized using an operator-defined intensity of 34/255; this intensity was selected since it provided the best resolution of early flame development (see appendix section A3.1). Then, every 30 binarized images were averaged together to give a probability of flame for each pixel in a 1 s period. This probability map was then binarized using a probability of 0.5 and then segmented into shapes using 8-point connectivity. The largest shape was selected and the locations of its tip and base were determined. Fig. 23 illustrates the IR flame length measurement process where t is the time from the start of the application of the burner. A picture of a lined grid was taken after the tests and was used to convert pixel length to physical length.

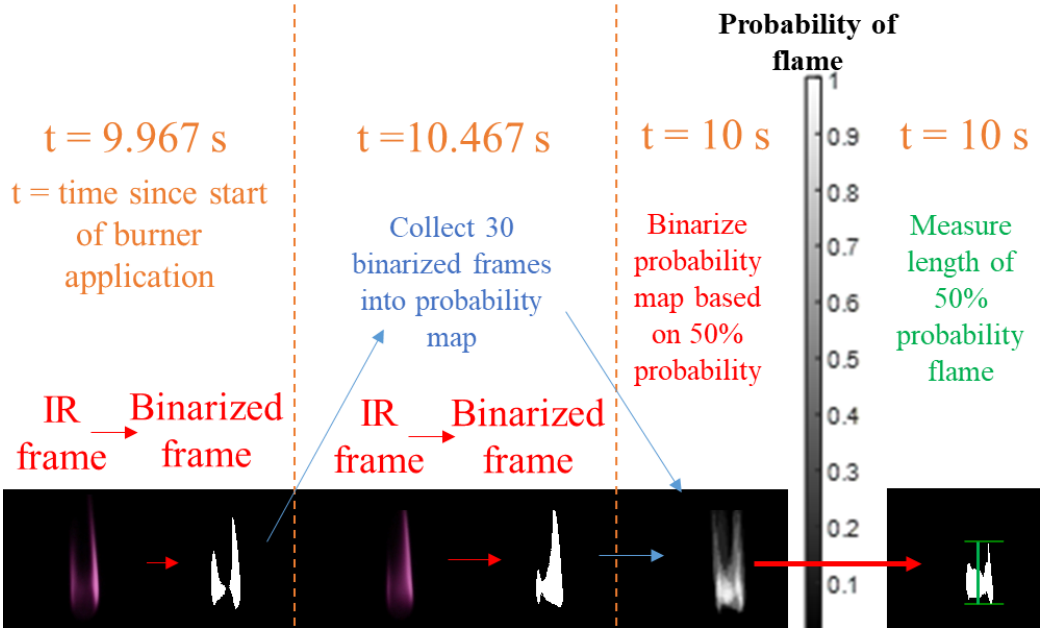

Fig. 23. An example illustrating the IR flame length measurement process.

4.7 Wall flame heat feedback model

Once the burner is removed, heat feedback from the flame fueled by polymer is the driving mechanism for flame spread and thus must be known for accurate modeling. In the UL-94V test, the polymer flame is a buoyancy-driven, laminar flame spreading vertically. The heat feedback of such flames has been rigorously characterized previously by Leventon et al. [75]. Leventon et al. studied laminar wall flames in a more controlled system. Samples were 5 cm wide slabs of heights 5–20 cm tall, insulated on all but one side so that the flame can only spread on the front face and so that the flame is uniform across the width of the sample. Mass loss and flame heat flux

were measured over time for several sample heights in separate experiments. A diagram of their sample holder is shown in Fig. 24 to illustrate the test geometry.

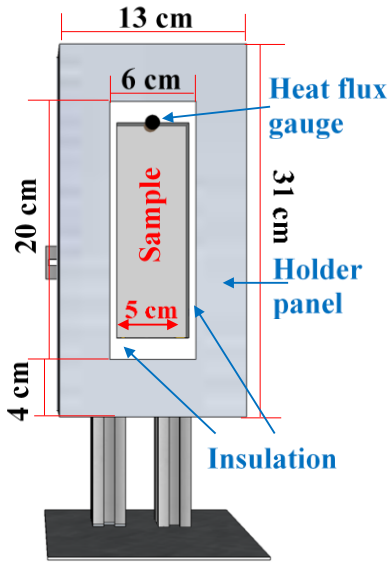

Fig. 24. Diagram of the vertical flame spread apparatus.

From the measurements, flame length (defined as the length of the region of nearly steady flame heat flux) as a function of width-normalized heat release rate (which was calculated from the mass loss rate) was determined. This quantity shall henceforth be referred to as heat flux flame length to differentiate it from the IR flame length. The expression for the heat flux flame length, y_f, is $y_f = a\left(\frac{dQ'}{dt}\right)^p + b$ where $\frac{dQ'}{dt}$ is the width-normalized heat release rate and a, b and p are empirical constants the values of which are given later in section 4.10.4. Leventon et al. used the flame heat

flux measurements to define the magnitude and distribution of the flame heat flux (specifically the shape of the decay profile). The flame heat feedback submodel was implemented into ThermaKin2Ds and was validated based on successful prediction of flame heat feedback over time [75]. In the 2D module of ThermaKin2Ds, the flame is represented by a heat flux profile applied to the front (and/or back) boundary once y_f is positive. Equation (12) expresses the flame heat flux in terms of material surface temperature, T_s [K], maximum flame temperature, $T_{f,max}$ [K], and a heat transfer coefficient, h_f, which had been determined to be 19.6×10^{-3} kW m^{-2} K^{-1} [75]. Radiation from the flame was found to be minor in comparison to convection [81] and was implicitly included in the heat transfer coefficient since the coefficient was derived based on total measured heat flux. T_{HFG} is the temperature of the water-cooled heat flux gauge sensor, measured to be 291 K; α_f defines the rate of decay of the flame heat feedback above y_f due to entrainment of air; and y^* is a dimensionless length scale based on the heat flux flame length. The model does not consider any blowing effect (reduction in convective heat transfer due to the outward flux of gaseous pyrolyzates of a burning surface) [79,80] because its effect is minor and current theory overcorrects for it, as was explained in section 3.6.1. Equation (13) defines y^* in terms of the distance from the bottom edge of the flame, y_{eff}, and the y_0 parameter which controls

the extension of the flame heat feedback beyond y_f. α_f and y_0 were determined to be 1.79 and 3.75 cm, respectively [75]. Finally, Equation (14) approximates $T_{f,max}$ as the adiabatic flame temperature, $T_{f,adiabatic}$, which is equal to 2330 K for PMMA [75], near the base of the flame and somewhat smaller beyond 5 cm above the base of the flame.

$$q_f'' = \begin{cases} h_f\left(T_{f,max} - T_s\right); & y_{eff} \le y_f \\ h_f\left(\alpha_f\left(T_{f,max} - T_{HFG}\right)e^{-\ln(\alpha_f)\cdot y^{*2}} + T_{HFG} - T_s\right); & y_{eff} > y_f \end{cases} \quad (12)$$

$$y^* = \frac{y_{eff}+y_0}{y_f+y_0} \quad (13)$$

$$T_{f,max} = \begin{cases} T_{f,adiabatic};\ y_{eff} \le 5\ cm \\ 0.87\ T_{f,adiabatic};\ y_{eff} > 5\ cm \end{cases} \quad (14)$$

Given the similarity in the flame structure, we adopted the flame heat feedback submodel expressions developed by Leventon et al. However, it was hypothesized that differences in sample geometry, notably the presence of free edges on the sides and bottom, may affect the magnitude of the flame heat flux; therefore, additional UL-94V tests were conducted with a heat flux gauge embedded into PMMA samples to verify the wall flame heat feedback submodel and, if needed, recalibrate it for the UL-94V geometry.

4.8 PMMA flame heat flux measurements

A procedure similar to the one described in section 4.3.1 was followed with a few changes. The sample was 1.3 cm wide PMMA with and without insulated sides instead of 1.4 cm wide Kaowool PM insulation and the sample was shifted so that it bisects the burner tube, in accordance with UL-94V [12]. The heat flux gauge was positioned from y = 0.4 to y = 6.0 cm for non-insulated samples and from y = 3.0 to y = 6.0 cm for insulated samples; 2–6 measurements were performed at each position. All tests were recorded with the IR camera looking from the side to measure IR flame length as described in section 4.6. IR flame length data were collected simultaneously with PMMA flame heat flux data to identify when the flame tip first reaches the heat flux gauge, so as to determine the heat flux of the tip of the flame, and to confirm when the flame has completely covered the heat flux gauge for determination of the steady PMMA flame heat flux. Heat flux of the tip of the PMMA flame was used to relate the simulated results to the experimental results, as explained in section 4.11.1. The steady PMMA flame heat flux measurements were used to quantify the flame heat feedback in the UL-94V test which was compared with the wall flame heat feedback submodel as detailed in section 4.7. A video of the front of the sample was also recorded to monitor the condition of the heat flux gauge surface and to observe possible melt flow or burnout.

4.9 Numerical simulation of UL-94V tests

The two-dimensional module of ThermaKin2Ds was used for the simulations of the UL-94V tests. It includes the wall flame heat feedback submodel formulated by Leventon et al. [75] summarized in section 4.7. The pyrolysis properties of the clear, extruded PMMA used in this work were obtained from an earlier study [64]. Further details of the PMMA pyrolysis properties were summarized in section 2.5 but they can also be found in the Appendix section A1.7. Two-dimensional simulations (including two-dimensional heat transfer inside the polymer sample) were performed because the burner and polymer heat feedback were only resolved in two dimensions and previous works have suggested that these simulations perform comparably to three-dimensional simulations [42,49] but with a significantly reduced computational cost. Since the UL-94V test has a plane of symmetry that bisects the sample, only half the sample was simulated. For example, the PMMA sample in the simulation was 12.5 cm tall and 0.135 cm thick with an adiabatic back boundary (which corresponds to the plane of symmetry). The conditions at the front boundary are discussed later in section 4.10.6. Spatial discretization was 1×10^{-3} cm in the thickness direction and 0.1 cm in the length direction; the timestep was 5×10^{-3} s. Decreasing these integration parameters by a factor of two had no significant impact on the simulation results, demonstrating convergence.

4.10 Experimental results and analysis

4.10.1 UL-94V burner flame temperature and heat flux

The burner flame temperature measurements were corrected for thermocouple radiative losses (4–126 K) and their associated errors were estimated to be approximately 2%, comparable to previous studies of high temperature flames [99,100]. There was no evidence of other effects which may impact thermocouple readings such as drift due to soot accumulation [101]. Further details of the corrections can be found in section A3.2 of the appendix. The corrected temperature profiles are shown in Fig. 25. From the profiles, the maximum temperature was extracted for each height (y) to be used in further analysis. Additionally, the x position of the maximum temperature was determined since it can provide an estimate of the thermal boundary layer thickness which was later used to estimate the heat flux based on the temperature measurements. Fig. 26 shows the extracted maximum temperatures and their x position for varied y.

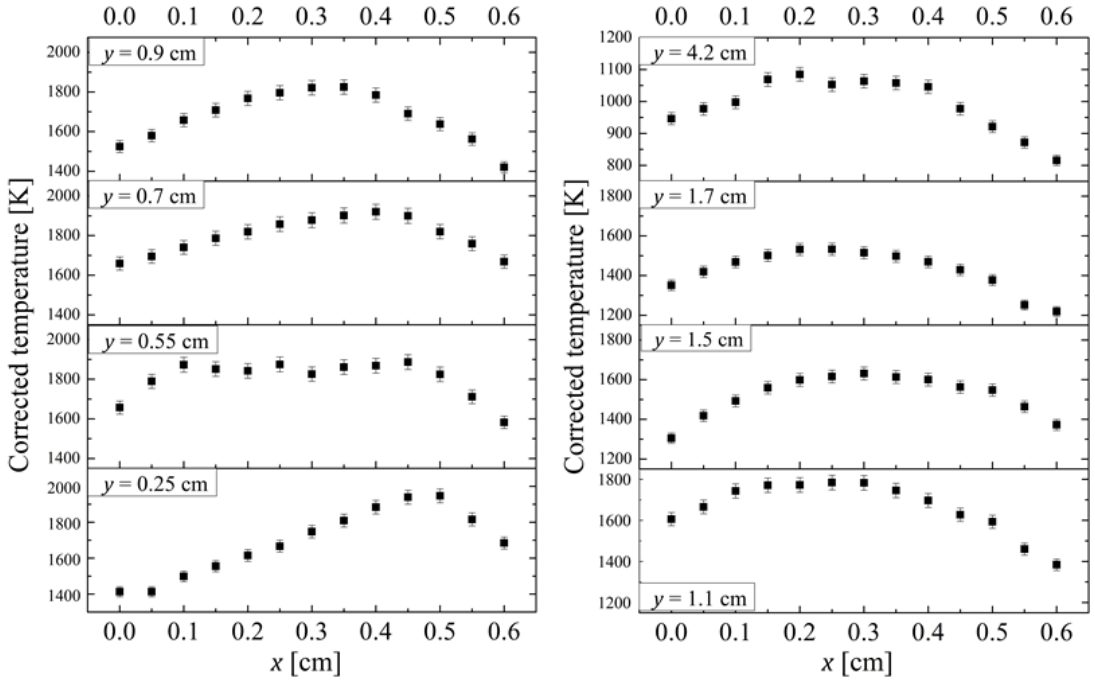

Fig. 25. Burner flame temperature profiles versus distance from the sample surface, x, for different heights, y, above the sample bottom. Temperature data were corrected for radiative losses.

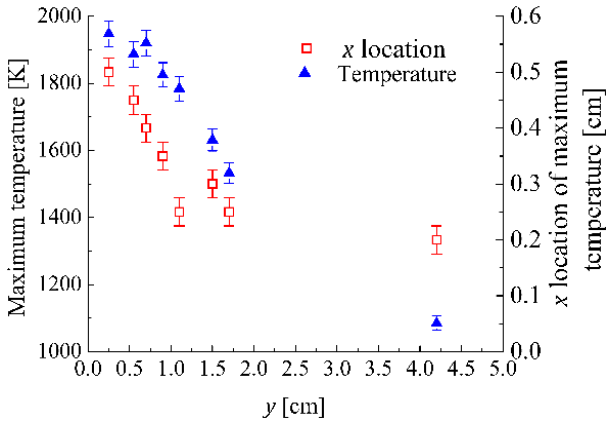

Fig. 26. Maximum corrected burner flame temperature and its location, x, as a function of the distance from sample bottom, y.

Burner flame heat flux measurements near the sides of the sample were found to be comparable to those in the center and showed no dependence on heat flux gauge diameter, so they were combined. Error in heat flux was taken to be the systematic 3% uncertainty of the NIST-traceable reference gauge plus two standard deviations of the mean calculated from repeated measurements. Fig. 27 shows the averaged burner heat flux and maximum burner temperature as well as estimates of the heat flux based on the temperature measurements.

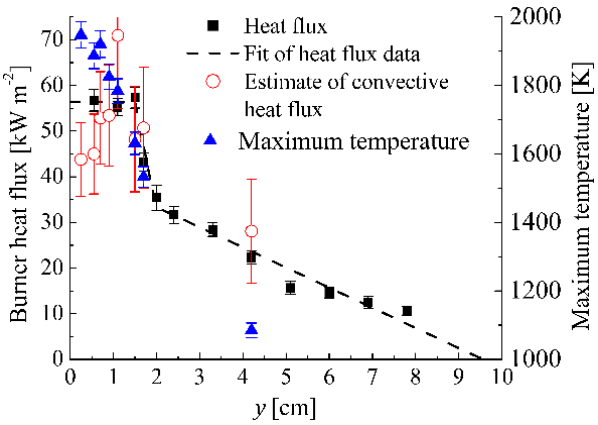

Fig. 27. Burner flame heat flux and maximum temperature presented as a function of distance from the sample bottom, y. Also shown is an estimate of the heat flux based on the temperature measurements.

The maximum temperature and heat flux profiles both show a steady region followed by a rapid linear decline and then a more gradual linear decline as y increases. As shown in Fig. 26, as the maximum temperature rapidly decreases with increasing y, the distance between the maximum temperature position and the sample surface

decreases; this decrease in thermal boundary layer thickness compensates for the decrease in temperature, manifesting in approximately constant heat flux for $y \leq 1.5$ cm (seen in Fig. 27). The heat flux estimated from the temperature data was calculated as $k\,\Delta T/\Delta x$, where k is the thermal conductivity of air at the maximum temperature, ΔT is the difference between the maximum temperature and that of the heat flux gauge sensor, and Δx is the distance between the maximum temperature location and the sample/gauge surface. As shown in Fig, 27, the heat fluxes estimated from the thermocouple measurements are close in value to those obtained using the heat flux gauges, which indicates that the flame heat flux to the surface is primarily convective, in agreement with previous studies [40,41,43].

The burner flame heat flux was fitted with a three-stage piecewise linear function as shown in Fig. 27. Based on the aforementioned findings, the heat flux was assumed to be entirely convective. For implementation into ThermaKin2Ds, this heat flux was expressed as a constant convective heat transfer coefficient, h_b [kW m^{-2} K^{-1}], and a three-stage piecewise linear function for the burner flame temperature [K]. h_b was determined by dividing the average heat flux for $y \leq 1.5$ cm by the difference between the averaged maximum burner temperature and the heat flux gauge temperature (T_{HFG} = 291 K). Equation (15) summarizes the expression for the burner flame heat flux, q_b'', to the sample surface at a variable temperature, T_s [K]. In the

simulation, the burner flame heat flux was applied for the first 10 s to reproduce the UL-94V test protocol.

$$q_b''[kW\ m^{-2}] = \begin{cases} h_b\ (1918 - T_s) & y \leq 1.5\ cm \\ h_b\ (3994 - 1383\ y\ - T_s) & 1.5\ < y\ \leq 2\ cm \\ h_b\ (1507 - 127\ y\ - T_s) & 2\ < y\ \leq 9.5\ cm \\ 0; & y\ > 9.5\ cm \end{cases} \quad (15)$$

$$h_b = 34.7\ \times\ 10^{-3}\ kW\ m^{-2}K^{-1}$$

For comparison, burner heat flux measurements of this work and literature values are summarized in Table 11. Additionally, h_b and burner flame temperature, T_b, are provided if they were determined in that work – some works used a constant heat flux rather than a convective term. Downey and Quintiere, who also measured burner heat flux with a water-cooled heat flux gauge, measured 57–65 kW m^{-2} in the $y\ \leq 1$ cm region [38,39], which agrees well with this work's measurements. The heat flux measured by Wang et al. [41,43] is significantly greater than this work's measurements. Interestingly, their estimated T_b is within 5% of this work's measurement. The discrepancy in heat flux is due mostly to discrepancy in h_b. It is suspected that the discrepancy in h_b is associated with differences in geometry. The convection to the copper slug (measured by Wang et al. [41,43]) may be greater than the convection to

the face of the sample (measured in this work). The burner heat flux assumed by Kempel et al. [49] is significantly greater than this work's measurements. It is also worth noting that only this work has fully characterized the burner heat flux across the entire sample. Previous works have either not measured the heat flux [49] or only considered heat flux to the bottom 1 cm of the sample [38,43]. This work has shown that the burner heat flux is steady until 1.5 cm from the bottom and is non-zero until about 9.5 cm from the sample bottom.

Table 11. Comparison of UL-94 burner flame heat flux measurements with literature values.

Authors	Source	Burner heat flux [kW m^{-2}] to a surface at 300 K	h_b [kW m^{-2} K^{-1}]	T_b [K]	Comments
McCoy and Stoliarov	This work	≈ 56 ± 2 kW m^{-2} in the steady portion	34.7×10^{-3}	1918± 39	Steady portion was in $y \leq 1.5$ cm. Measured with heat flux gauge (HFG)
Downey and Quintiere et al.	[38,39]	57–65	N/A	N/A	Very similar approach. Measured with a 0.64 cm diameter HFG
Wang et al.	[41,43]	≈ 94	54.3×10^{-3}	2026	Analysis of copper slug temperature measurement
Kempel et al.	[49]	≈ 82 (average of first 1.5 cm)	N/A	N/A	Not a measurement. Assumed candle flame with 150 kW m^{-2} maximum and rapid decay

4.10.2 Sample surface oxygen content under burner and PMMA flames

Fig. 28 shows the burner oxygen concentration measurements, which indicate the presence of a steady region of very low oxygen concentration (≤ 1 vol%) from 0 to 0.5 cm from the sample bottom followed by a linear increase in oxygen concentration. Error bars are two standard deviations of the mean of the time-averaged data plus a

systematic error of 0.2 vol% specified for the transducer by the manufacturer. Before further analysis, the oxygen content was averaged in the region between y = 0.7 and 1.7 cm resulting in an average of approximately 5 vol%. This region was chosen because it contains significant oxygen concentration and overlaps with the high burner flame heat flux (> 45 kW m^{-2}) region.

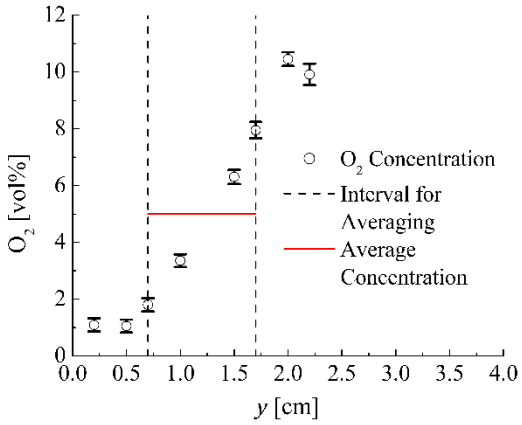

Fig. 28. Burner flame oxygen concentration measurements at the sample surface as a function of the distance from the sample bottom, y.

Oxygen content was also measured at the surface of a burning PMMA sample as mentioned in section 4.3.2. Average oxygen concentrations were found to be 0.65 ± 0.25 vol% or smaller for all sampled locations. This is in agreement with previous measurements of oxygen concentration in laminar flames spreading on PMMA slabs which found effectively no oxygen under the PMMA-fueled flame [13]. Thus, only oxygen from the premixed burner flame needs to be considered.

4.10.3 PMMA in 5 vol% oxygen: TGA results and oxidation submodel

TGA experiments were conducted in a 5 vol% O_2 (balance N_2) atmosphere based on the average measured oxygen content of the burner flame to determine its impact, for this given concentration, on the decomposition (and subsequently ignition) of PMMA. Previously, oxidation was accounted for in the simulation of cone calorimetry by correcting ignition times based on the shift in temperature corresponding to 5% mass lost observed in TGA data in air and nitrogen, as explained in section 3.8. However, this approach is not feasible for modeling of UL-94V since the prediction of extinction and ignition are a critical part modeling the test, so a correction cannot be simply made. Thus, a more rigorous attempt was made to study and model the impact of oxygen on the pyrolysis of PMMA (and other polymers). Since oxidation is known to act primarily at the surface of the material [50–53], it was hypothesized that increased surface area would enhance the mass loss to oxidation. To investigate this, preliminary TGA experiments were conducted using 4–7 mg samples either in the form of a chunk (single solid piece) or in the form of powder (higher surface area) and the results are summarized in Fig. 29. As Fig. 29 shows, the powder sample began to lose mass at a lower temperature than the chunk sample; this behavior was seen for additional tests (not shown). Additionally, thermal decomposition (without oxidation) was confirmed to be independent of surface area by comparing the

TGA results in 100 vol% N_2 of a powder and of a chunk sample and finding that their results overlap completely.

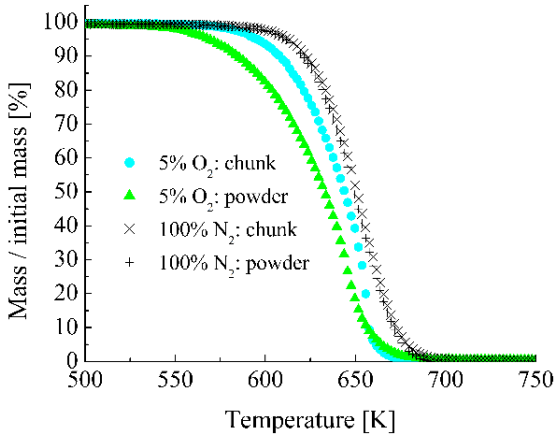

Fig. 29. Preliminary examination of sample surface area effect on mass loss dynamics observed in TGA experiments on PMMA in 5 vol% O_2 (balance N_2) and 100 vol% N_2 at 10 K min^{-1}.

It was further hypothesized that the MLR due to oxidation would scale linearly with sample surface area. Additional experiments in 5 vol% O_2 (balance N_2) were subsequently performed to demonstrate linear scaling. Samples were either medium-sized rectangular pieces (initial surface area ≈ 0.14 cm^2) or larger pieces (initial surface area ≈ 0.19 cm^2) which were approximately square, finely cut with a laser. The initial surface area includes all faces except the face touching the bottom of the crucible. However, it was found that during the test, the PMMA would soften and gradually fill the crucible (0.58 cm diameter). The tests were stopped at 600 K to better preserve the

shape of the sample and an average of the initial and final surface areas of the samples were computed to be used in further analysis.

Given that oxygen enhances decomposition primarily at the surface [50] and not throughout the solid, the TGA MLR data were normalized by their average sample surface area rather than by mass. The sample-surface-area-normalized MLR data of both medium and large samples reasonably converged and were thus combined and used for the development of the PMMA oxidation submodel. Additionally, a single TGA test was performed in a 7 vol% O_2 (balance N_2) atmosphere to determine if the result would be significantly different if the maximum oxygen concentration within the high burner heat flux region was used instead. Fig. 30 shows the experimental sample-surface-area-normalized MLR data for both 5 vol% and 7 vol% O_2 atmospheres and no significant differences are seen.

PMMA oxidation was modeled in ThermaKin2Ds by adding a surface reaction to the previously developed pyrolysis model summarized in section 2.5. This reaction was expressed as $J = C\ \exp(-D/RT_B)$ where J is the area-normalized MLR to the gas phase [g cm^{-2} s^{-1}], T_B is the temperature at the boundary [K], R is the universal gas constant [kJ mol^{-1} K^{-1}], and C and D are effectively a pre-exponential factor and activation energy [24]. C and D were varied until the area-normalized MLR predicted by the pyrolysis model in ThermaKin2Ds agreed well with the sample-surface-area-

normalized MLR from the TGA experiments; their values were determined to be C = 5.6×10^9 g cm^{-2} s^{-1} and D =162 kJ mol^{-1}. As shown in Fig. 30, the decomposition model fits both 5 and 7 vol% O_2 data well. Without the oxidation reaction, the simulation shows no significant mass loss below 600 K.

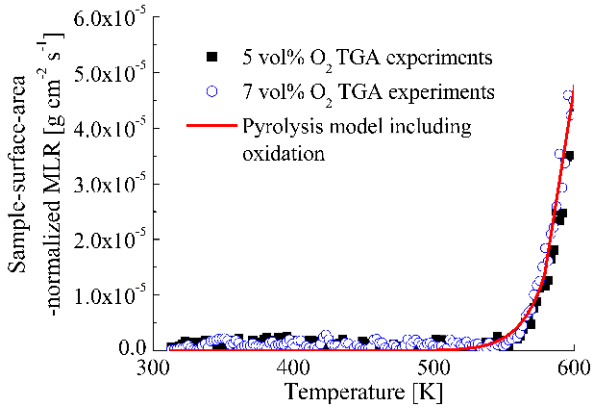

Fig. 30. Experimental and modeled sample-surface-area-normalized mass loss rate of PMMA in TGA performed in 5 and 7 vol% of O_2 (balance N_2) at 10 K min^{-1}.

For the UL-94V simulations, the oxidation submodel was implemented in ThermaKin2Ds by defining a section of the front edge between y = 0.7 and 1.7 cm, 1 $\times 10^{-3}$ cm thick, as oxidizable PMMA. Oxidizable PMMA has the same physical properties as PMMA; it serves only to selectively apply the oxidation boundary condition for approximately the duration of the burner application since the

measurements confirmed that the oxygen concentration under the PMMA-fueled flame was near zero.

4.10.4 Heat flux flame length expression

The expression of Leventon et al. [75] for heat flux flame length (y_f) was modified because it was originally parameterized on flames larger than 2 cm in length and therefore did not correctly predict positive y_f in the UL-94V experiments at the time of ignition. The first data point, corresponding to the width-normalized heat release rate at ignition, was added so that positive y_f was calculated by the simulation at the time of experimental ignition. The heat flux flame length expression was subsequently refitted. Fig. 31 shows the heat flux flame length data as well as the heat flux flame length predicted by Leventon's expression and the modified expression. As shown, for $y_f \geq 3$ cm, the original and modified expressions are effectively the same. The modified expression for the heat flux flame length has the same functional form, $y_f = a\left(\frac{dQ'}{dt}\right)^p + b$, but different coefficient values: a = 39.5 [cm$^{1.66}$ kW$^{-0.66}$], b = – 1.1 $\times$ 10^{-2} [cm] and p = 0.66.

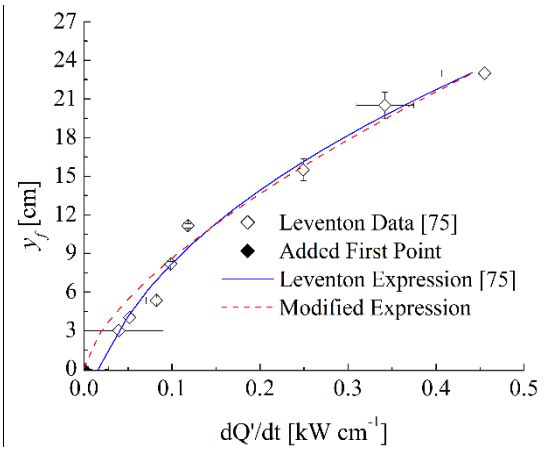

Fig. 31. Dependence of heat flux flame length on width-normalized heat release rate and the original [75] and modified heat flux flame length expressions.

4.10.5 PMMA flame heat flux measurements and wall flame submodel

PMMA flame heat flux data of each test were averaged in time once the flame fully covered the heat flux gauge after the burner had been removed and the heat flux reading was quasi-steady (absolute derivative with respect to time less than 1 kW m^{-2} s^{-1}). Time-averaged flame heat fluxes were then averaged together from repeated tests and are presented for insulated and non-insulated samples in Fig. 32. The error bars were computed as two standard deviations of the mean plus the systematic 3% uncertainty of the NIST-traceable reference gauge.

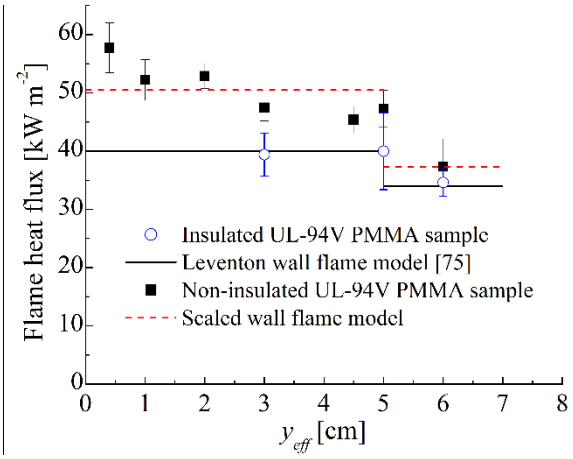

Fig. 32. PMMA flame heat flux measured in the UL-94V tests and the original [75] and scaled flame heat feedback submodel predictions.

Fig. 32 compares the measured PMMA flame heat fluxes to the laminar wall flame submodel of Leventon et al. [75]. This comparison indicates that, when the sides of the UL-94V sample are insulated, the polymer flame is effectively the same as the flames on the wider (5 cm) wall-embedded samples studied by Leventon et al. However, when the sides are not insulated, the flame heat flux is significantly greater. The increase in flame heat flux for non-insulated UL-94V samples was accounted for in the submodel by increasing the flame heat transfer coefficient, h_f, of Leventon's flame heat feedback submodel by 26.5% and reducing the assumed flame temperature for $y \geq 5$ cm by 11.5%, resulting in the dashed lines shown in Fig. 32.

From the IR videos, it was found that the flames were slightly thicker on insulated samples than non-insulated samples. To quantify this observation, the average

flame standoff distance was estimated using the same image analysis technique described in section 4.6. From the base to the top of the flame, the width of the flame was determined at all points and then averaged for each time step. By dividing the average width by two and subtracting half the initial sample thickness (0.135 cm), an estimate of the flame standoff distance is obtained. Then, using the corresponding IR flame length data, the flame standoff distance data were binned together based on IR flame length and averaged. The results are shown in Fig. 33 where the error bars are two standard deviations of the mean.

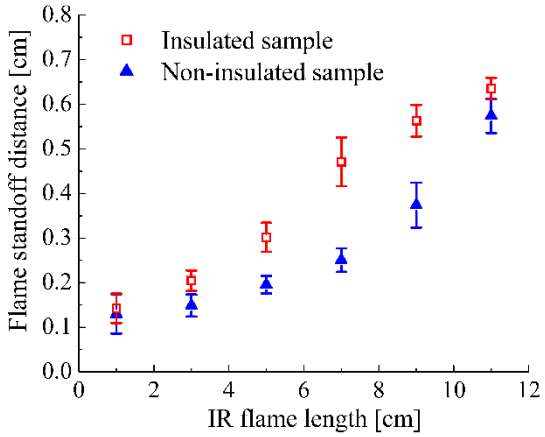

Fig. 33. Estimated flame standoff distance for both non-insulated and insulated samples and its dependence on IR flame length.

As shown, for all sizes of the PMMA flame, the flame standoff distance is smaller for non-insulated samples than for insulated samples. It was found that for the non-insulated samples, the flame standoff distance is about 0.11 cm smaller, on

average. This reduction represents a ≈ 27% decrease, which is comparable to the increase in measured flame heat flux of the non-insulated samples. It is hypothesized that with the edges of non-insulated samples burning, a larger flame results in greater buoyant acceleration and consequently, greater entrainment from the sides pushes the flame closer to the sample, reducing the standoff distance and increasing the heat flux.

4.10.6 Summary of thermal boundary conditions used in the UL-94V simulations

Considering the differences in measured PMMA flame heat flux, two separate simulations were conducted: one representing the non-insulated sample and the other representing the insulated sample. The oxidation submodel, heat flux flame length expression, and burner heat flux submodels are the same for both cases. Additional measurements using wider insulation samples confirmed that the burner flame heat flux is unaffected by insulated sides. Table 12 summarizes the PMMA flame heat feedback submodel parameters that differ between the two simulations.

Table 12. Summary of PMMA flame heat feedback submodel parameters used for simulations of UL-94V tests performed on non-insulated and insulated samples. The parameters not reported in the table are the same for both sample types.

Case	$h_{f,PMMA}$ [kW m^{-2} K^{-1}]	$T_{f,PMMA}$ [K]; $y_{eff} \leq y_f$ & $y_{eff} \leq 5$ cm	$T_{f,PMMA}$ [K]; $y_{eff} \leq y_f$ & $y_{eff} > 5$ cm
Insulated	19.6×10^{-3}	2330	2027
Non-insulated	24.8×10^{-3}	2330	1795

4.11 Results of modeling UL-94V for PMMA

4.11.1 Relating simulated heat flux flame length to experimental IR flame length

Before making any comparison, it is necessary to understand the difference between the heat flux flame length used in the flame heat feedback submodel and the experimental IR flame length. This difference is illustrated by Fig. 34. This figure shows the heat flux profile of the flame spreading on a solid. It has a region of relatively constant flame heat flux with a step transition at 5 cm and then exponential decay. The length of this relatively steady region defines the heat flame length (y_f) used in ThermaKin2Ds and calculated using the expression given in section 4.10.4. In the experiment, it is the IR image of the flame that is measured from the initial base to the tip for defining the IR flame length, labeled in the figure as $y_{eff,tip}$. As was pointed out by Leventon et al. [75] and shown in Fig. 34, $y_{eff,tip}$ extends past y_f and enters the

region of decaying heat flux. It was hypothesized that for each type of sample geometry (insulated or non-insulated), the tip of the flame has a characteristic heat flux. This heat flux can then be used to determine the value of y^* via Equation (12), which can be then used to relate the simulated y_f to the experimental $y_{eff,tip}$.

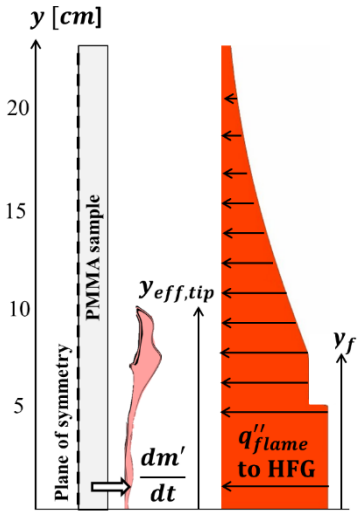

Fig. 34. An illustration of flame spreading on a pyrolyzing solid including the flame heat feedback profile as measured by a water-cooled HFG. Only half the sample is shown because of the symmetry of the problem. The figure illustrates how the experimental IR flame length, $y_{eff,tip}$, extends past the heat flux flame length, y_f, used in ThermaKin2Ds.

The heat flux of the tip of the flame was determined by identifying when it reached the center of the heat flux gauge and then selecting the corresponding heat flux data point. For the non-insulated samples, this process was repeated nine times for three different heat flux gauge locations: y = 4.5 cm, 5.0 cm, and 6.0 cm. Measurements below these locations were not used since the heat flux measurements approached their

steady values almost immediately after the burner was removed. For the insulated samples, this process was repeated a total of five times at y = 5.0 cm and 6.0 cm. The heat flux corresponding to the flame tip was determined to be 24 ± 4.4 kW m^{-2} for the insulated samples and 27.3 ± 4.1 kW m^{-2} for the non-insulated samples where the uncertainty is two standard deviations of the mean plus 3% for the uncertainty in the NIST-traceable reference gauge. In both cases, these values represent a full range of measurement locations confirming the validity of the aforementioned hypothesis. Using the heat fluxes of the flame tip in Equation (12), y^* was obtained for the tip and was found to be more or less the same for both insulated and non-insulated samples. Thus, the values were averaged together to obtain $y^*_{tip} = 1.25 \pm 0.12$. The final expression: $y_{eff,tip}$ [cm] = 1.25 (y_f [cm] + 3.75) – 3.75 is obtained by re-arranging Equation (13). $y_{eff,tip}$ was then calculated for all simulated cases and then compared with the experimental measurements.

4.11.2 Results and modeling for insulated PMMA samples

As an example, Fig. 35 illustrates the results over time of a simulated UL-94V test of an insulated PMMA sample. The temperature maps are of the sample viewed from the side with the front face on the right. The filled-area plots illustrate the net heat flux calculated by ThermaKin2Ds along the sample surface after smoothing with a 5-s

moving average. Also plotted on the net heat flux graphs are the calculated y_f, shown as a black, vertical line. Notice that in the first 5 s, the net heat flux matches the shape of the burner heat flux profile measured by the heat flux gauge. Once the burner is removed and the PMMA flame manifests, y_f corresponds to a region of approximately constant net heat flux. Above y_f, the net heat flux decays rapidly. Variations in net heat flux are due to variations in surface temperature (since it is a convective flux), the reduction in flame temperature due to entrainment described by Equation (14), and due to the Monte-Carlo algorithm used for the radiative heat transfer between the sample and the environment [24]. Flame spread is captured by the advancement of y_f. Sample burnout is seen starting between 35 and 45 s near the front, bottom portion of the sample.

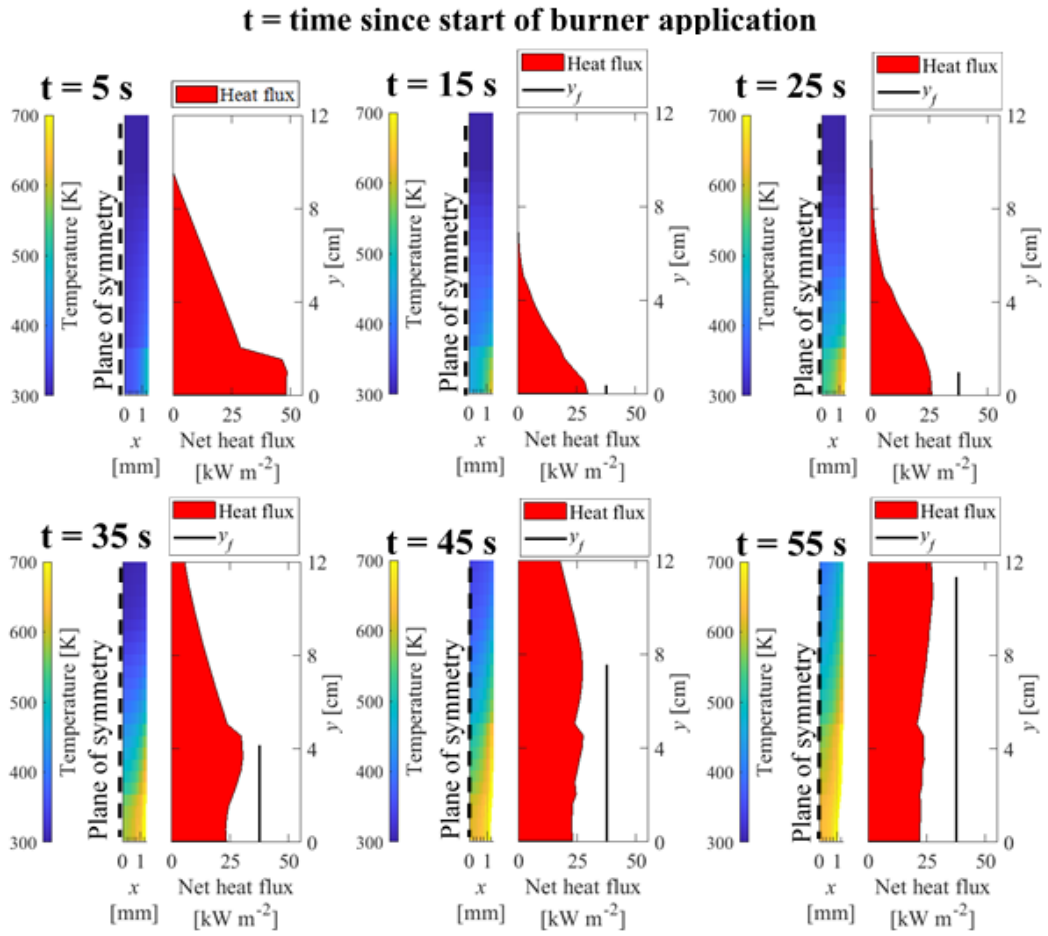

Fig. 35. Simulated insulated sample temperature contours, time-averaged net heat flux, and y_f calculated by ThermaKin2Ds over time. Only half the sample is shown because of the symmetry of the problem.

Comparison of the modeling results with the experimental results of the insulated samples is shown in Fig. 36. The experimental $y_{eff,tip}$ was averaged from three separate tests. Experimental uncertainties were estimated by propagation of the uncertainties in the pixel measurement and in the conversion from pixels to physical

length and were found to be about 18%, on average, as further explained in the section A3.3 of the Appendix. The model predictions of $y_{eff,tip}$ are shown as shaded areas to account for the uncertainty in the relation between y_f and $y_{eff,tip}$. The dip in the model's $y_{eff,tip}$ near 20 s is due to the model's coarse transition from oxygen-enhanced pyrolysis to non-oxygen-enhanced pyrolysis, however, this does not hamper agreement with experimental results. Looking at the plot on the left, the model predicts the experimental results well, especially for the first 38 s of the test. Then, the model begins to overpredict $y_{eff,tip}$ due to the onset of melt flow which was not originally included in the model. To better account for dripping, an additional mass flux boundary condition was included to represent the removal of PMMA due to dripping. his mass flux boundary condition is of the same equation form as the oxidation boundary condition, except with different kinetic parameters; PMMA removed due to dripping does not contribute to the simulation's flame length. An estimate of the activation energy of PMMA dripping was taken from the literature [82] (80 kJ mol^{-1}) and the pre-exponential factor (1.66×10^3 g cm^{-2} s^{-1}) was varied until simulations predicted 60 ± 6% mass lost to dripping in accordance with a previous study of UL-94V tests using 0.3 cm thick PMMA [102]. As shown, inclusion of dripping enables the model to predict $y_{eff,tip}$ for nearly the entire test. The model does overpredict the flame length

at the end of the test due to the simplicity of the dripping submodel. Still, the overall success of the model, especially at early stages, supports the validity of the various submodels used.

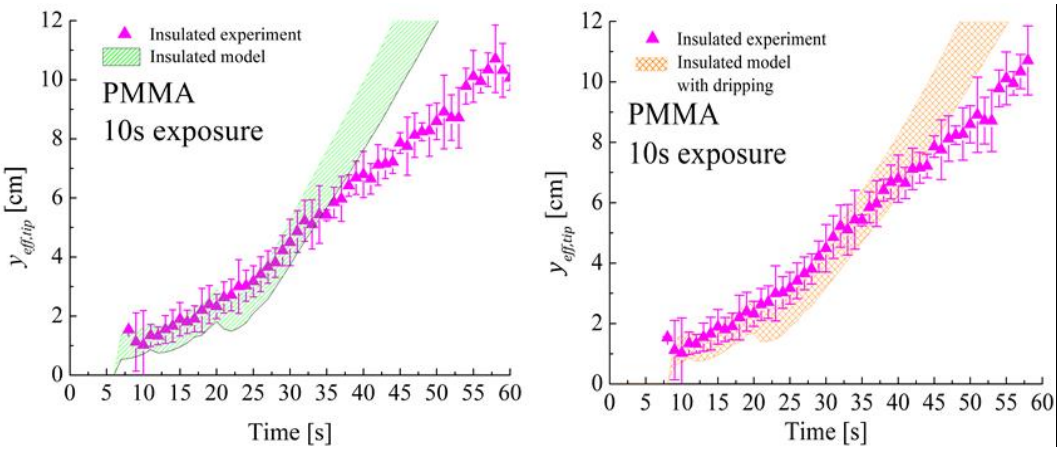

Fig. 36. Comparison of experimental and simulated flame spread dynamics for insulated samples. When dripping is included in the model, predictions improve. The shaded area accounts for the uncertainty in the value of y^* used to relate the simulated y_f to $y_{eff,tip}$.

4.11.3 Results and modeling for non-insulated PMMA samples

The results of the experiments and modeling for non-insulated samples are shown in Fig. 37. The experimental $y_{eff,tip}$ was also averaged from three separate tests. Experimental uncertainties were about 8%, on average, as explained further in section A3.3 of the Appendix. Looking at the experimental results, the rate of spread is significantly faster when the edges are not insulated and the test takes about 35 s as opposed to about 60 s to reach the top.

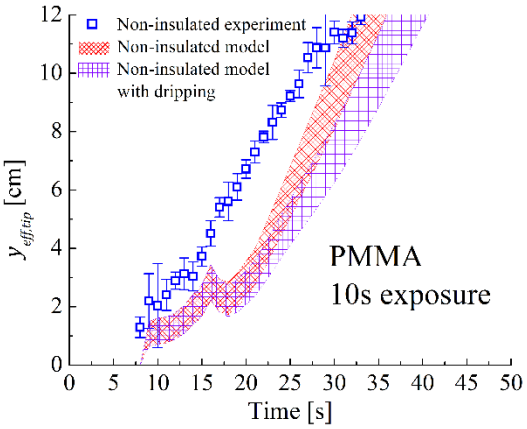

Fig. 37. Comparison of experimental and simulated flame spread dynamics for non-insulated samples. The shaded area accounts for the uncertainty in the value of y^* used to relate the simulated y_f to $y_{eff,tip}$.

Overall, the model is able to predict that flame spreads to the top of the sample; however, it underpredicts $y_{eff,tip}$ throughout the duration of the test. Additionally, the model does not fully capture the transition from oxygen-enhanced to non-oxygen-enhanced pyrolysis (at about 17 s), but it does predict the rate of spread reasonably well after the transition, especially if dripping is considered. Unlike the results for the insulated samples, the model does not successfully predict initial $y_{eff,tip}$ despite the correction made to the PMMA flame heat feedback. It is believed that this discrepancy is associated with the pyrolysis, flame spread, and potentially oxidation on the edges of the sample, which are not captured by the current two-dimensional model. These edge effects enhanced initial flame growth and spread. This explanation is supported

by several previous studies [40,41,43]. Nevertheless, to the author's knowledge, this is the best prediction to date of flame spread on a UL-94V sample.

Chapter 5: Extension of UL-94V model to other polymers

The success of the model's predictions of the UL-94V test motivated investigation into its ability to predict the results for other polymeric materials, both those which fail the test and those which pass the test. UL-94V tests were conducted with and without insulated sides to investigate the importance of edge effects on other polymers in the UL-94V test. Simulations of the UL-94V test were performed and then compared with experimental results.

5.1 Materials and sample preparation

The materials studied other than PMMA included several materials which either fail the UL-94V test (no rating or HB rating) or pass (V-0 rating). These materials were chosen since comprehensive pyrolysis parameter sets had been previously developed for these materials, allowing for simulation in ThermaKin2D, and because they represent a range of UL-94V ratings. The materials which fail UL-94V were acrylonitrile butadiene styrene (ABS), high-impact polystyrene (HIPS), and glass-fiber reinforced (25 wt.%) poly(butylene terephthalate) (PBT/GF25). The thicknesses of these materials were 0.31, 0.29, and 0.16 cm thick, respectively. The materials which pass UL-94V were poly(ether ketone) (PEEK), polyetherimide (PEI), and poly(vinyl chloride) (PVC). The thicknesses of these materials were 0.32, 0.30, and 0.30 cm,

respectively. Further details about the materials, including manufacturer, are given in Table 13. Reported ratings have an associated thickness because thickness can affect UL-94V rating; thinner materials are easier to ignite and sustain flame. All materials were prepared in the same manner as the clear, extruded PMMA, which was described in section 4.1, with the same length and width and with some of the samples insulated on the sides to investigate the importance of edge effects.

Table 13. Summary of materials used in the UL-94V study.

Material	**Thickness [cm]**	**Rating (thickness [cm])**	**Rating Source**	**Manufacturer**
ABS	0.31	HB (0.16)	Westlake Plastics	Westlake Plastics
HIPS	0.29	HB (0.147)	Americas Styrenics (Styron)	Spartech
PBT/GF25	0.16	HB (0.15)	BASF (rated material may not have 25% GF)	BASF
PMMA (clear, extruded)	0.27	NR	Acrylite	Acrylite / Evonik
PEEK	0.32	V-0 (0.15)	Curbell Plastics	Victrex
PEI	0.30	V-0 (0.075)	Sabic	GE Plastics
PVC	0.30	V-0 (0.31)	Curbell Plastics	Vycom

5.2 Revised test approach

The V-0 rated materials, PEEK, PEI, and PVC, self-extinguish after the first 10 s application of the burner which prompts a second application of the burner. However, modeling two applications of the burner is a non-trivial task since the model would have to consider the cooling of the sample between applications of the burner. Assumptions would also have to be made about how quickly the burner should be re-applied in the simulation once extinction occurred. In light of this, it was decided to simplify the problem by conducting tests using a single 20 s application instead of two 10 s applications. To evaluate the equivalency of this altered procedure, we conducted a UL-94V test on each material, including PMMA, as according to the standard (two 10 s applications) and our modified procedure (one 20 s application) and compared the results; samples were not insulated. Additionally, based on the findings from the literature review and tests using PMMA, the importance of edge effects will be explored for the other materials by separate testing samples with and without insulated sides. Thus, it will be determined if these slight changes in procedure affect the UL-94V ratings.

5.2.1 Effect of burner application time on UL-94V test results

It was hypothesized that using a single 20 s application instead of two 10 s applications would not significantly change the outcome of the UL-94V test (using non-insulated samples). For the materials which fail UL-94V, only one 10 s application was needed since the materials did not self-extinguish. Fig. 38 compares the results using a 10 s versus 20 s exposure time for ABS, HIPS, PMMA, and PBT/GF. As shown for these materials, $y_{eff,tip}$ values are effectively the same throughout the test except for a brief period from 10–20 s. This strongly supports that using a 20 s application does not alter the outcome of the UL-94V test for the materials which sustain flame and fail the test.

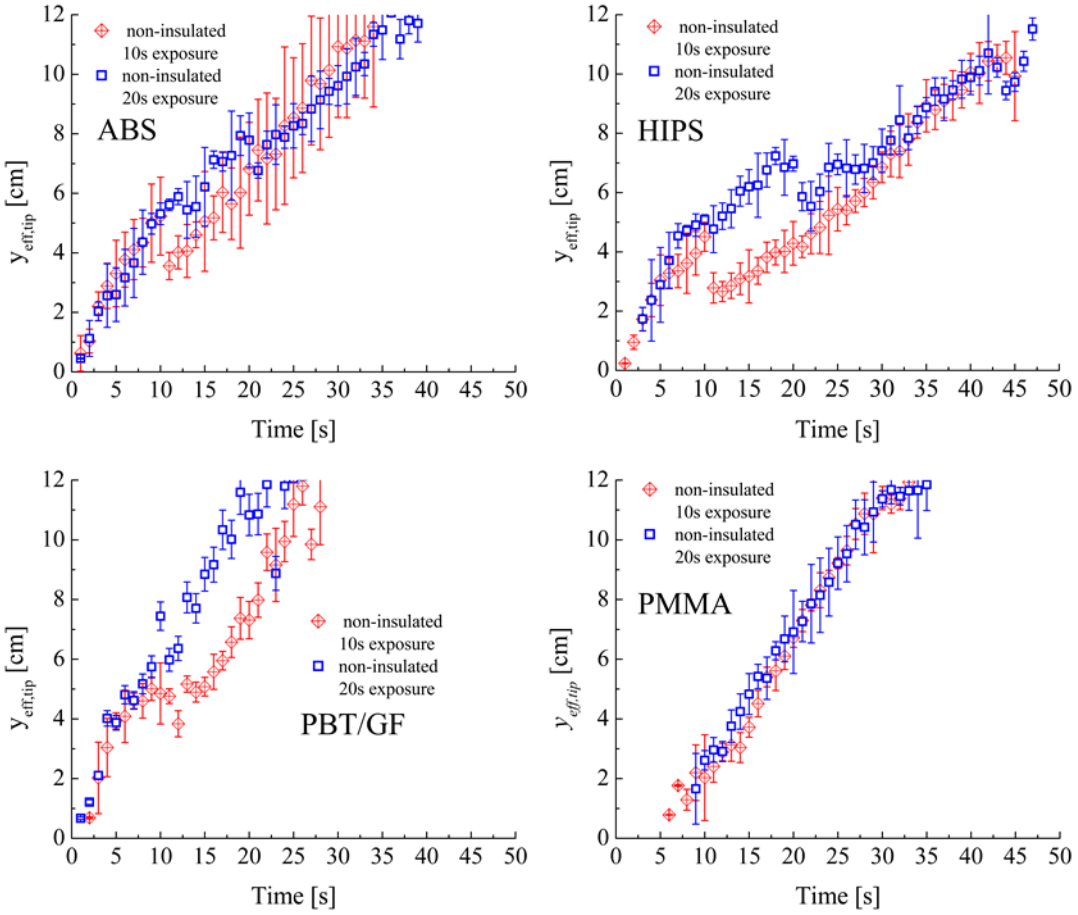

Fig. 38. Comparison of UL-94V experimental data for materials which fail UL-94V using one 10 s exposure versus one 20 s exposure.

For the materials which pass, two 10 s applications were performed since the flames do self-extinguish. Fig. 39 compares the results using two 10 s exposures versus one 20 s exposure time for PEEK, PEI, and PVC. In all cases, the flame self-extinguished after the removal of the burner for repeated 10 s applications and for the single 20 s application. Additionally, the experimental $y_{eff,tip}$ appear to be the same

for both cases. This supports the notion that a single 20 s application does not significantly alter the outcome of the UL-94V test for the passing materials as well. Thus, given that the results of UL-94V test are largely unchanged by applying the burner once for 20 s instead of twice for 10 s, this work will adopt a single 20 s exposure time since that greatly simplifies modeling. All further results shall feature data based on 20 s exposure times.

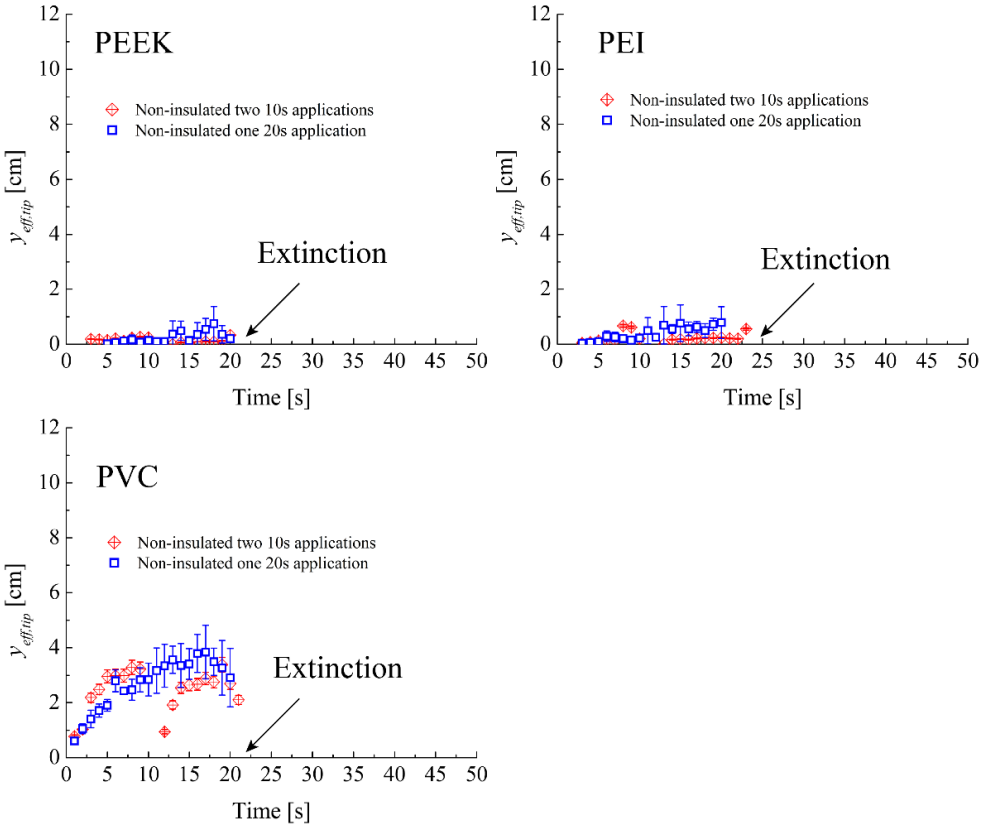

Fig. 39. Comparison of UL-94V experimental data for passing materials using two 10 s exposure versus one 20 s exposure.

5.2.2 Effect of insulated sides on UL-94V rating

The impact of insulated sides on UL-94V rating was explored by comparing the experimental data with and without insulated sides for 20 s exposures. Fig. 40 illustrates the results for the materials which fail UL-94V and Fig. 41 illustrates the results for the materials which pass. Like PMMA, all other samples which sustained flaming showed slower rate of flame spread on insulated samples than non-insulated samples; this reduction in rate of spread is likely due to the reduced influence of edge effects and reduced flame heat flux. The results for the materials which pass UL-94V, however, practically overlap and show no impact whatsoever due to the presence of insulation. For the materials which fail UL-94V, $y_{eff,tip}$ are not exactly equal during the first 20 s, but they are comparable. This is expected since the burner flame is narrower (1.0 cm) than the sample (1.3 cm wide) and only impinges the front and back faces and not the sides. Most importantly, the outcome (UL-94V rating) is still the same for all materials regardless if the sample was insulated or not. Insulated sides had no impact whatsoever on UL-94V test outcome for the samples studied in this work. Thus, samples with insulated sides will used in conjunction with non-insulated samples to evaluate the model since they represent a significantly easier problem to model as was seen for tests using PMMA and discussed in section 4.11.

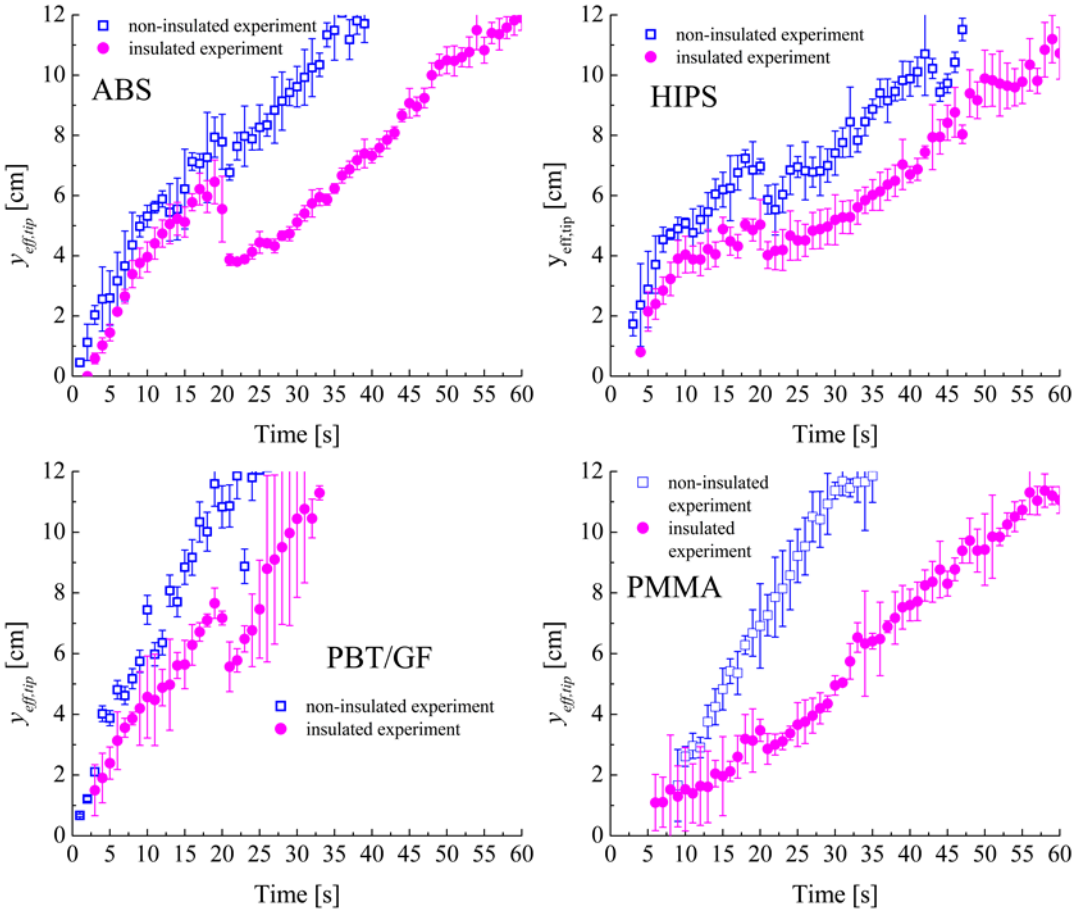

Fig. 40. Comparison of $y_{eff,tip}$ experimental results of materials which fail UL-94V with and without insulated sides for a 20 s exposure. The insulation does reduce the rate of spread, but the end result of the test is the same.

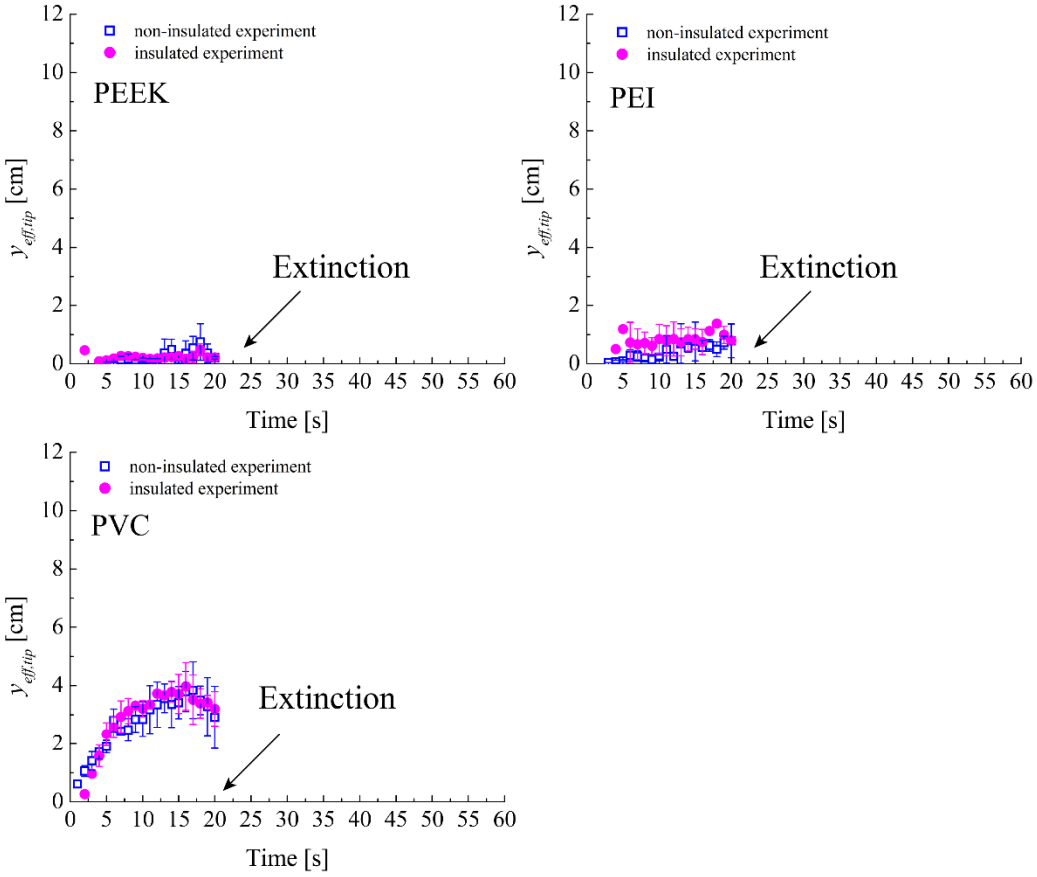

Fig. 41. Comparison of experimental results with and without insulated sides for materials which pass UL-94V. No impact is seen by the presence of insulation.

5.3 Experimental results and model development for other polymers in UL-94V tests

Simulation of a UL-94V material requires submodels for the burner heat flux, polymer flame heat feedback, pyrolysis (in an inert environment), and potentially, a submodel for oxidation due to the oxygen content of the burner flame. Submodels for the first three items have already been developed and only the oxidation submodels

need to be developed further prior to simulation; the results of the oxidation measurements are presented in the following sections.

5.3.1 Effect of 5 vol% oxygen atmosphere on thermal decomposition of other polymers

TGA tests in 5 vol% oxygen (balance nitrogen) and 100 vol% nitrogen were performed for all materials based on the measured burner flame oxygen content. Samples were cut rectangles with a well-defined surface area (initial surface area ≈ 0.13 - 0.16 cm^2). Several of the materials showed an additional reaction corresponding to the oxidation of the char. However, oxidation is only a concern leading up to ignition after which the decomposition is effectively inert due to the presence of a diffusion flame, as confirmed by the oxygen measurements under a PMMA polymer flame as discussed in section 4.10.2. Thus, we are only concerned if oxygen has an impact on the first reaction peak (lowest temperature), enabling ignition to occur at lower temperatures. Only HIPS (in addition to PMMA) showed a significant shift in temperature as illustrated by Figure 42 below. Subsequently, an oxidation submodel was developed for HIPS as described in section 5.3.2.

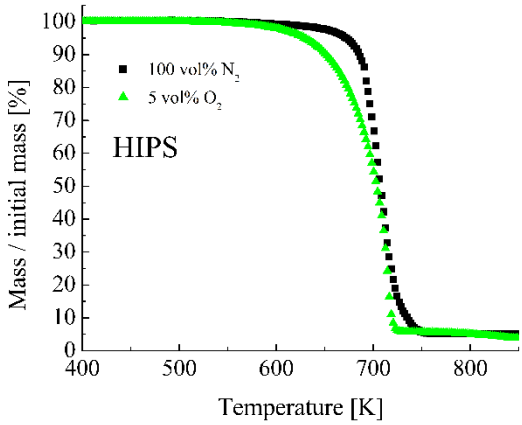

Fig. 42. TGA experiments on HIPS in 5 vol% O_2 (balance N_2) and 100 vol% N_2 at 10 K min^{-1}.

5.3.2 Oxidation submodel for HIPS in 5 vol% oxygen

The oxidation submodel for HIPS was developed in the same manner as PMMA described in section 4.10.3. Mass loss rate data were normalized by an average of the sample's initial and final surface areas because the sample would change shape and fill the pan. The kinetic parameters for the HIPS oxidation submodel were determined via inverse analysis using ThermaKin2Ds. Recall from section 4.10.3 that the oxidation reaction is expressed as $J = C\ \exp(-D/RT_B)$ where J is the area-normalized MLR to the gas phase [g cm^{-2} s^{-1}], T_B is the temperature at the boundary [K], R is the universal gas constant [kJ mol^{-1} K^{-1}], and C and D are effectively a pre-exponential factor and activation energy [24]. Fig. 43 shows the experimental mass flux of HIPS in 5 vol% O_2 (balance N_2) as well as the result of the oxidation submodel. The derived kinetic parameters for the oxidation of HIPS in 5 vol% O_2 are $C = 8.3 \times 10^3$ g cm^{-2} s^{-1} and $D =$

110 kJ mol^{-1}. The oxidation reaction accounts for nearly all the simulated mass loss (or temperatures below 650 K; simulated mass loss to thermal decomposition alone represents less than 1% of the total mass loss, on average, in this temperature range.

For the UL-94V simulations, the oxidation submodel was implemented in ThermaKin2Ds by defining a section of the front edge between y = 0.7 and 1.7 cm, 1 × 10^{-3} cm thick, as oxidizable HIPS. Oxidizable HIPS has the same physical properties as HIPS; it serves only to selectively apply the oxidation boundary condition for approximately the duration of the burner application since the measurements on a burning PMMA sample confirmed that the oxygen concentration under the flame is effectively zero for UL-94V samples.

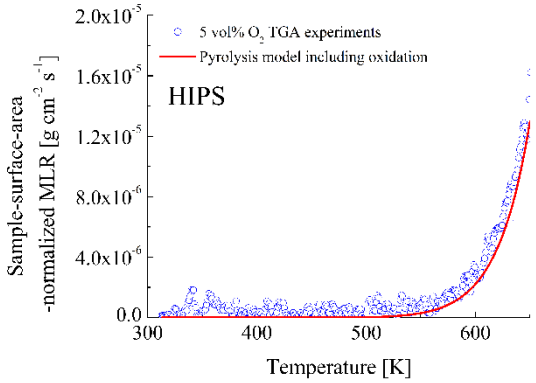

Fig. 43. Experimental and modeled sample-surface-area-normalized mass loss rate of HIPS in TGA performed in 5 vol% of O_2 (balance N_2) at 10 K min^{-1}.

5.3.3 Model formulation for other polymers

The burner heat flux profile remains the same and the heat flux flame length expression (y_f), written in terms of HRR, also remains the same when simulating other materials. The convective coefficient for polymer flame heat feedback submodel was assumed to be the same for each material since the geometry of the sample does not change and because the wall flame model was able to predict experimental flame heat fluxes of several polymers using a single heat transfer coefficient and material-specific flame temperatures [75]. Much like the modeling of the cone calorimeter, a generalized flame temperature was sought to allow for predictions of materials with unknown flame temperatures. An average flame temperature was calculated from the adiabatic flame temperatures of a range of materials [75]. The adiabatic flame temperatures used were calculated based on heats of combustion from MCC data rather than cone calorimeter data because these temperatures provided the best predictions of flame heat feedback on small, vertical samples [75]. This average value was calculated to be ≈ 2360 K, which is very close to the adiabatic flame temperature of PMMA (2330 K), so for simplicity, the temperature was unchanged when simulating the other materials. Additionally, preliminary simulations found the results were largely unchanged when using material-specific flame temperatures as shown in section A.3.4.

Only a few parameters thus had to be changed when simulating other materials: The pyrolysis property set, the oxidation model parameters if applicable, and the thickness of the sample. Table 14 summarizes which submodels and parameters remained the same and which ones changed.

Table 14. Summary of UL-94V parameters dependence on material

Parameters which changed with material	Parameters which remained unchanged
• Pyrolysis property set • Sample thickness • Oxidation submodel (if applicable)	• Burner convective coefficient and burner flame temperature expressions • y_f and $y_{eff,tip}$ expressions • Polymer flame convective coefficient • Polymer flame temperature • Positioning of oxidative layer (if applicable)

5.4 Comparison of simulations with UL-94V experiments using insulated sides

The following sections compare the simulated results and experimental results for each material using insulated samples. The results for non-insulated samples are found in section 5.5. Error bars of experimental $y_{eff,tip}$ data and the uncertainty of the shaded area of the model predictions were determined in the same manner done for PMMA, details of which were given in section 4.11.2.

5.4.1 Results and modeling for insulated materials which fail UL-94V

The results for all the materials which fail UL-94V test suing samples with insulated sides are shown in Fig. 44. Starting with PMMA, much like the results for 10 s exposure, predictions of $y_{eff,tip}$ are quite good, especially when dripping is considered; see section 4.11.2 for the dripping submodel discussion and parameters.

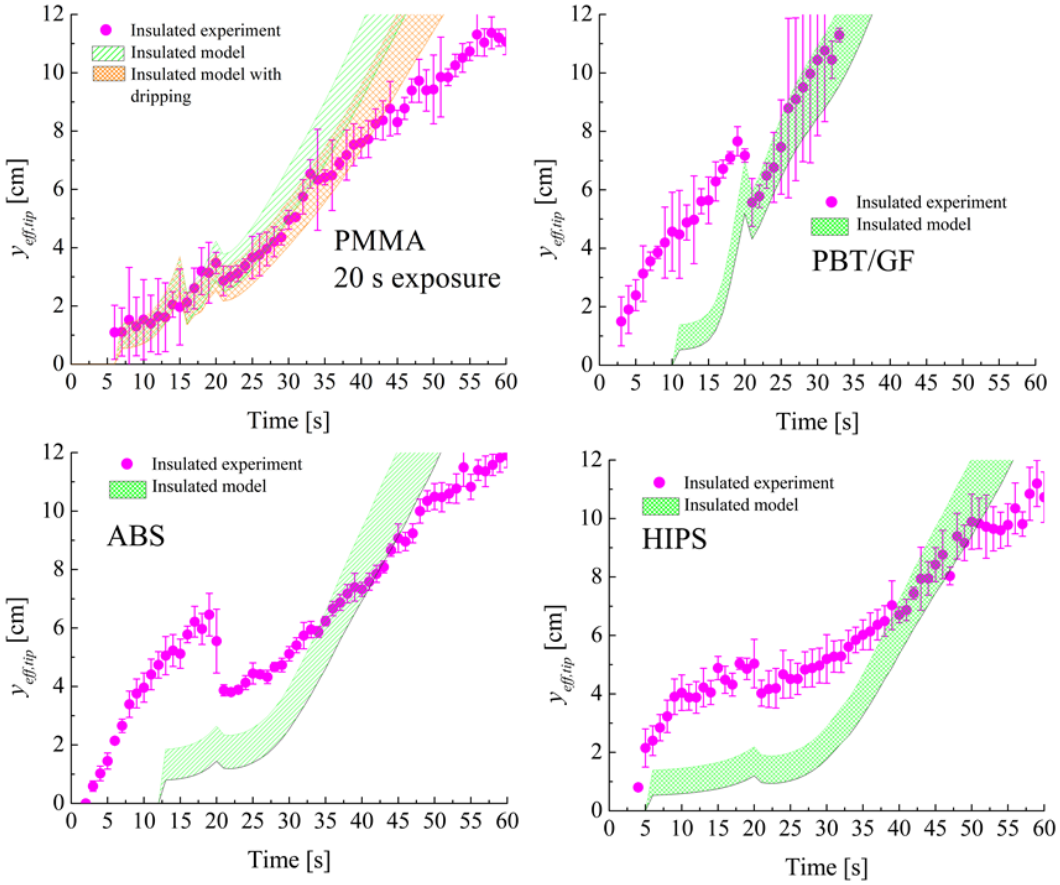

Fig. 44. Comparison of experimental and simulated flame spread dynamics for materials which fail UL-94V using samples with insulated sides.

Only PMMA showed significant dripping during the test so a dripping submodel was only considered for PMMA.

The model's prediction of PBT/GF was a mixed result. The model failed to predict early $y_{eff,tip}$, initial rate of spread, and ignition properly. It also overpredicts rate of spread from 15–20 s. However, this overprediction helps to compensate such that predictions after 20 s are excellent. Additionally, the rating of the test (NR) was successfully predicted by the simulation. Possible reasons for the poor initial predictions by the model shall be discussed later in section 5.4.3.

The results for ABS and HIPS are quite similar. In both cases, the model was able to successfully predict that the flame reaches the top of the sample, failing the test. However, the simulation significantly underpredicts initial $y_{eff,tip}$ and rate of spread during the first 25–30 s for both materials and in the case of ABS, predicts a later ignition time. Possible reasons for this underprediction shall be discussed in section 5.4.3. Additionally, near the end of the experiment, the model begins to overpredict the rate of spread for both materials. One possibility is melt flow, however, these materials did not exhibit significant melt flow until the conclusion of the test. Another possibility for this overprediction is that the model fails to account for the reduction in incident heat flux due to the accumulation of soot. Both ABS and HIPS are highly sooting materials. Previous work by Leventon et al. found ABS and HIPS laminar wall flames

could even self-extinguish due to soot deposition [75] as illustrated in Fig. 45, courtesy of Dr. Leventon. The layer of soot acts a heat transfer barrier to the polymer sample surface, which can even inhibit upward flame spread when given enough time to accumulate.

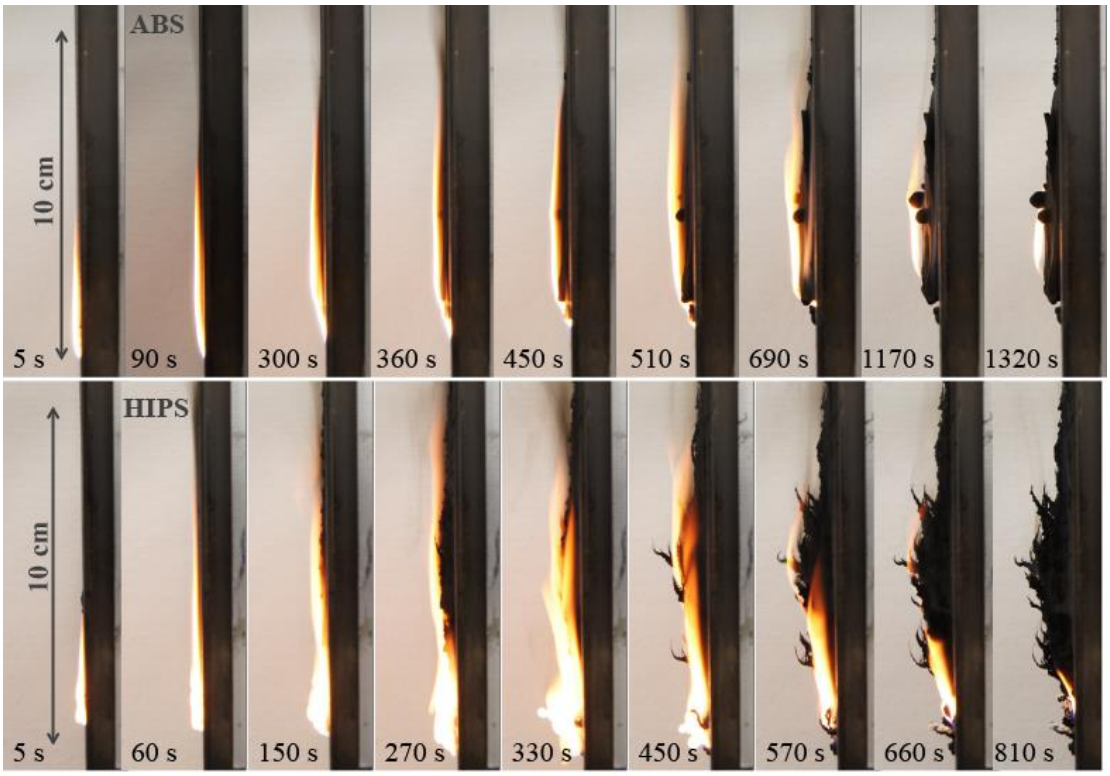

Fig. 45. Photographs illustrating self-extinguishment of ABS (top) and HIPS (bottom) laminar wall flames due to soot deposition [75]. Photographs were provided courtesy of Dr. Leventon. The layer of soot acts as a thermal insulator, preventing extension of the pyrolysis front, preventing upward propagation such that the flame extinguishes due to burnout of the lower region.

To investigate the possibility that soot effects are responsible for the overpredictions, simulations were redone with the net flame heat feedback reduced by about 34% once the model exceeded 5 cm in $y_{eff,tip}$. This 34% estimate was found by comparing the heat flux data of a soot covered gauge with that of a gauge that was kept clean by an insulation shield which was removed at a later time [75]; soot covered gauge readings were 30 – 38% lower than clean gauge readings for ABS and HIPS samples 5 cm tall [75]. The results of the simulation with reduced heat flux are shown in Fig. 46. Fig. 46 strongly supports that the reduction in net heat flux due to soot deposition in the experiment was responsible for the discrepancy. Once this soot effect is included in the model, the rate of spread predictions at later times agree very well with the experiment.

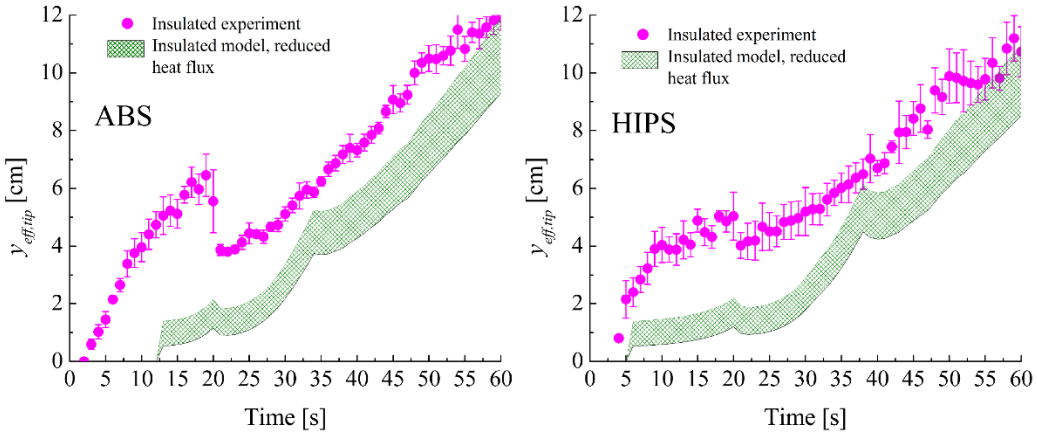

Fig. 46. Comparison of experimental and simulated flame spread dynamics for insulated ABS and HIPS samples but with the net heat flux of the model reduced once $y_{eff,tip}$> 5 cm to imitate the effects of soot accumulation.

5.4.2 Results and modeling for insulated materials which pass UL-94V

Fig. 47 shows the results for PVC insulated UL-94V tests and model predictions. The PVC experiment performs quite differently than the other passing materials because while the burner is applied, it produces relatively large flames much like the materials which failed the test (ABS, HIPS, PBT/GF, and PMMA). However, as soon as the burner was removed, it extinguishes. The simulation predicts the initial flame growth quite well while the burner is applied. However, the simulation fails to predict extinction. One possible explanation is that the chlorinated species produced by the decomposing PVC inhibit the gas-phase combustion, destabilizing the polymer flame. Species containing chlorine or other halogens are hypothesized to inhibit

combustion by catalyzing the recombination of radical species, effectively trapping the radicals which would otherwise propagate the reaction [103–106]. The addition of chlorine gas to premixed flames has been found to reduce burning velocities [107].

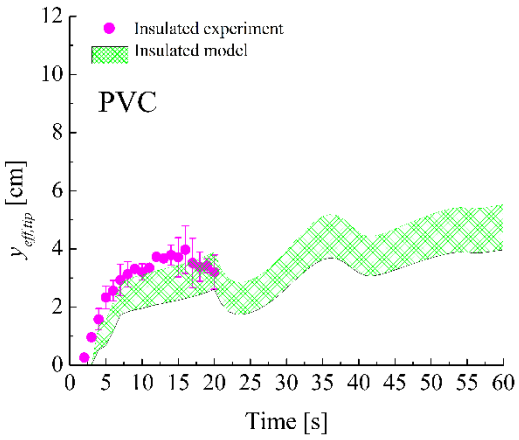

Fig. 47. Comparison of experimental and simulated flame spread dynamics for insulated PVC samples.

ThermaKin2Ds assumes instantaneous reaction between gaseous pyrolyzate and oxidizer and does not explicitly model the gas-phase combustion chemistry. Fully resolving the chemistry of the combustion of PVC is an extremely difficult task. Even a simulation of thermal decomposition of PVC, without any sort of flame heat feedback or flame spread submodels, that fully resolves the species generated is not currently feasible. Further work is needed to determine how to best implement gas-phase effects into ThermaKin2Ds.

Regarding the other passing materials, PEEK and PEI, neither material sustains flame as was shown in Fig. 41. While the burner was applied, both produce small flamelets that disappear once the burner is removed. For both of these materials, the model does not predict ignition, so no simulated results are shown. However, the criterion for ignition was based on steady burning so this result is reasonable. Additionally, the outcome of the test (V-0) rating is predicted successfully.

5.4.3 Overall model performance for insulated UL-94V tests

Overall, the model performs reasonably well. Ratings of all but one material were successfully predicted. Successful predictions of rate of spread at later times for PBT/GF and for ABS and HIPS once soot depositions effects were considered, support the pyrolysis and flame heat feedback submodels as well as the scaling analysis to relate simulated y_f to experimental $y_{eff,tip}$. Initial predictions of $y_{eff,tip}$ had mixed success. For the passing materials, predictions were good, supporting the burner and pyrolysis submodels. However, for the materials which sustain flame, initial $y_{eff,tip}$ were consistently underpredicted. One possibility may have to do with the oxidation submodel as in the case of HIPS since its oxidation submodel was not validated at a larger scale. Another possibility is due to the sensitivity of the UL-94V model to the pyrolysis submodels and the inability of some pyrolysis models to capture the very

small mass fluxes that correspond to the onset of ignition. These small mass fluxes were not modeled at the time since they were comparable to the noise in CAPA experiments and represent only a very small fraction of the test. To investigate this possibility, mass fluxes near the onset of steady burning rate were extracted from CAPA data for ABS, HIPS, and PBT/GF under 50–60 kW m^{-2} irradiation [59,64,67]; these data were chosen since they correspond to the heat fluxes of the UL-94V burner and polymer flames. The extracted mass fluxes were multiplied by the materials' heats of combustion (or average heat of combustion) obtained from MCC to obtain HRR per unit area. The HRR per unit area were multiplied by 0.015 m to obtain the HRR per unit width, $\frac{dQ'}{dt}$, of the pyrolyzing region of the UL-94V sample; simulations found that the bottom 0.015 m of the sample is responsible for effectively all of the volatile flux (or equivalently, $\frac{dQ'}{dt}$) produced in the first 20 s. $\frac{dQ'}{dt}$, converted into units of kW cm^{-1}, is then used to calculate y_f using the expression given in section 4.10.4 which is then used to calculate $y_{eff,tip}$ based on the analysis in section 4.11.1. Essentially, the error in predicted onset mass flux can be used to estimate the corresponding error in initial predicted $y_{eff,tip}$. Table 15 summarizes the results of this sensitivity analysis. Overall, the analysis suggests that initial $y_{eff,tip}$ might be underpredicted by the model by about 2.0 cm. This is reasonably close to the initial discrepancies between the experiment and

model for these materials, supporting this possibility. Future work will seek to better resolve onset mass fluxes to improve predictions of ignition and extinction in simulated UL-94V tests.

Table 15. Results of the sensitivity analysis of the impact of error in onset mass fluxes of the pyrolysis model on computed $y_{eff,tip}$

Material	Error in predicted onset mass flux [kg m^{-2} s^{-1}]	Error in initial predicted $y_{eff,tip}$ [cm]
ABS	$\approx 2.0 \times 10^{-4} - 7.0 \times 10^{-4}$	1.4 – 2.2
HIPS	$\approx 5.0 \times 10^{-4} - 6.0 \times 10^{-4}$	2.0 – 2.1
PBT/GF	$\approx 2.0 \times 10^{-4} - 9.0 \times 10^{-4}$	1.3 – 2.0

5.5 Comparison of simulations with UL-94V experiments with non-insulated sides

The following sections compare the simulated results and experimental results for each material using non-insulated samples. The results for insulated samples are found in section 5.4. Although the results of the insulated samples are better defined, the results of the non-insulated samples can be used to evaluate the importance of edge effects.

5.5.1 Results and modeling for non-insulated materials which fail UL-94V

Fig. 48 shows the results for the non-insulated samples. Beginning with PMMA, as was seen for the results for 10 s exposure, when the sample is not insulated, the model underpredicts $y_{eff,tip}$ throughout the experiment, suggesting that pyrolysis and flame spread on the edges, or so called-edge effects, are responsible. Rate of spread

predictions are reasonably good, however, if dripping is considered. Overall, the performance is about the same as was seen for 10 s exposures. PBT/GF also shows signs of edge effects with the experimental data outpacing the model's predictions to a greater extent on non-insulated samples than for insulated samples. The model underpredicts $y_{eff,tip}$ for the duration of the experiment on non-insulated samples whereas for insulated samples it did predict flame spread well after 20 s had passed. Still, the model does predict the outcome of the test properly.

ABS and HIPS both show signs of edges effects. As shown in Fig. 48, flame spread is much, much faster than that predicted by the model when the sides are not insulated and initial predictions of $y_{eff,tip}$ are worse. The model does, however, predict the outcome of the test properly. Additionally, like the results on the insulated samples, the model overpredicts rate of spread at later times for both ABS and HIPS. Once again, the test was re-simulated for these two materials with the net heat flux reduced by 34% once the model's $y_{eff,tip}$ exceeds 5 cm, the results of which are shown in Fig. 49. As shown, the results with the reduced heat flux better predict rate of spread while still predicting the UL-94V rating properly, supporting the hypothesis that soot accumulation is responsible for the discrepancy.

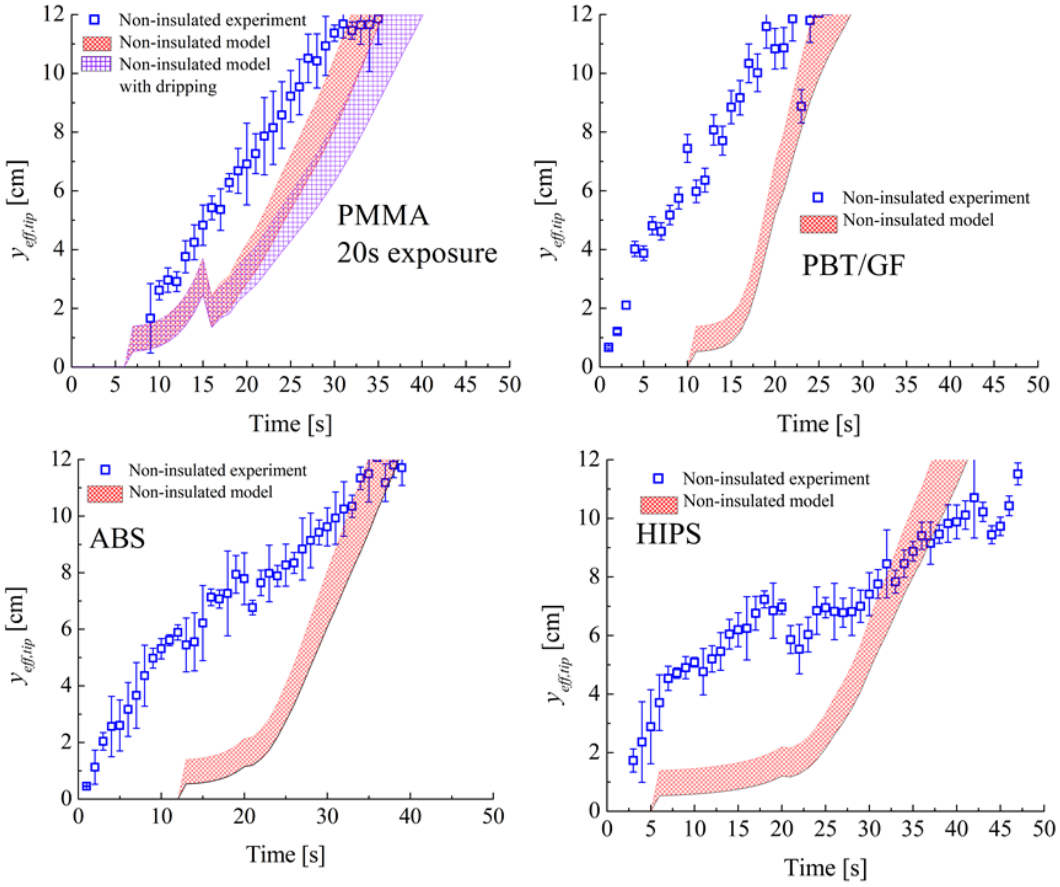

Fig. 48. Comparison of experimental and simulated flame spread dynamics for materials which fail UL-94V using non-insulated samples.

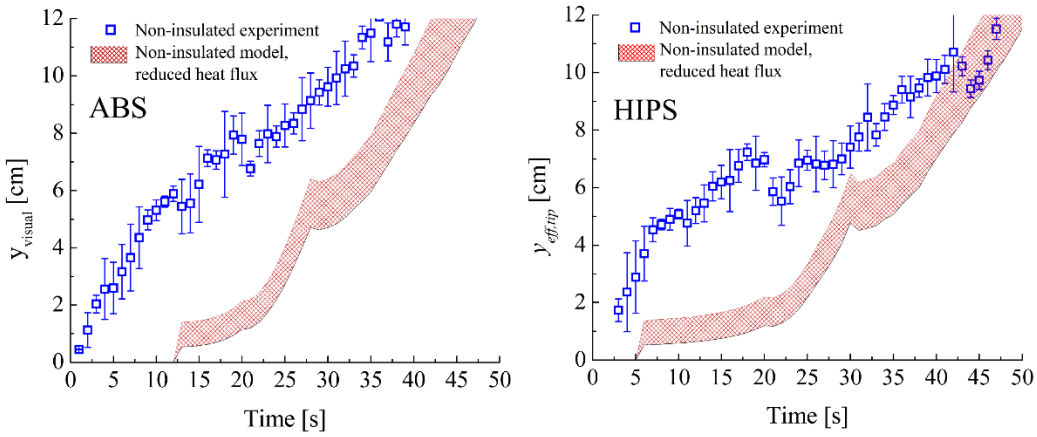

Fig. 49. Comparison of experimental and simulated flame spread dynamics for non-insulated ABS and HIPS samples but with the net heat flux of the model reduced once $y_{eff,tip}$> 5 cm to imitate the effects of soot accumulation.

5.5.2 Results and modeling for non-insulated materials which pass UL-94V

As Fig. 50 shows, the model performs about the same on the non-insulated PVC sample as it did for the insulated PVC sample. Initial predictions of $y_{eff,tip}$ and spread are quite good but the model fails to predict the extinction once the burner is removed due to the instabilities of the PVC flame as discussed in section 5.4.2.

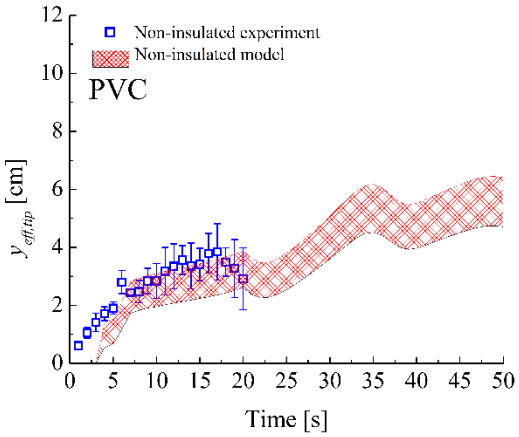

Fig. 50. Comparison of experimental and simulated flame spread dynamics for non-insulated PVC samples.

There is not much to discuss further about the results for PEEK and PEI of non-insulated samples since the simulation does not ignite for either material, so no figure is provided. The increase in flame heat feedback when simulating non-insulated samples does not affect the results since ignition is controlled by the burner model which does not change. The experimental results also showed that $y_{eff,tip}$ are effectively the same on insulated and non-insulated samples, which is reasonable since the burner flame is narrower than the sample as discussed in section 5.2.2. Still, the model does predict the rating for both these materials with and without insulated sides.

5.5.3 Overall model performance for non-insulated UL-94V tests

Overall, the model can predict the outcome of the UL-94V test on non-insulated samples. Ratings on all but one material (PVC) were successfully predicted. However, when compared to the results with the insulated samples, agreement between model and experiment is much worse for materials which spread flame, likely due to the pyrolysis, burning, and oxidation at the sample edges.

Chapter 6: Oxidative pyrolysis study

6.1 Overview

This work was able to model steady burning in the cone calorimeter and rate of spread on UL-94V samples reasonably well. However, the model failed to predict time to ignition properly for certain polymeric materials both in the UL-94V test and in the cone calorimeter for low levels of irradiation. It was hypothesized that the presence of oxygen in the air above the sample in the cone calorimeter test and the oxygen present in the pre-mixed burner flame in the UL-94V test enhanced decomposition, resulting in shorter ignition times than predicted by the pyrolysis models which were developed in inert conditions for reasons discussed in section 2.3 and 2.4. TGA experiments in 21 vol% O_2 and 5 vol% O_2 atmospheres confirmed that some of the materials studied begin to lose mass at significantly lower temperatures when oxygen is present, supporting the hypothesis. For modeling the cone calorimeter test, a simple analysis using thermally-thick ignition theory was able to correct ignition times for oxidation effects. For modeling the UL-94V test, a simple correction is not sufficient since the occurrence of ignition must be predicted within a set time frame. For this case, a more rigorous modeling of oxidation was developed. TGA experiments were performed using rectangular samples in 5 vol% O_2 atmospheres. Mass loss rate data were extracted and

then normalized by average sample surface area since preliminary results and findings from the literature suggested a surface area dependence. The pyrolysis model was supplemented by an additional mass flux expression whose kinetic parameters were varied until simulations predicted experimental mass flux. However, this oxidative model was not validated on larger-scale samples and the surface area of the sample did change over time since it would melt and fill the pan. Additionally, expressions for oxidative pyrolysis would be valuable for air (20% O_2) and other oxygen concentrations. Given its importance in predicting ignition in these fire tests, a better understanding of oxidative pyrolysis is needed.

A methodology similar to that used in comprehensive pyrolysis model development was used. First, milligram-scale TGA tests are performed to derive oxidative kinetics while removing the complication of thermal transport. Two approaches are considered based on the findings of the literature review. One approach was to use powdered samples to derive volumetric oxidative kinetic parameters. The activation energy and pre-exponential factors of the existing reaction scheme are changed to fit the data. The other approach was to assume oxidation occurs only at the surface and to inversely analyze the mass loss rate normalized by sample area of disc-shaped samples. For this case, the reaction scheme is unchanged but an additional mass-flux expression, like the one described in section 4.10.3, is included in simulations.

Next, gram-scale CAPA II experiments are performed to study oxidative pyrolysis at a larger scale to determine which approach for determination of oxidative kinetics gives the best predictions of mass loss rate. Back surface temperature data will be used to determine if oxidation produces any appreciable heating of the sample.

6.2 TGA in oxygenated environments revisited

6.2.1 Material and sample preparation

The material used for this portion was cast, black PMMA (henceforth black PMMA). Black PMMA was chosen because it is sensitive to oxidation, much like clear, extruded PMMA, but its pyrolysis properties have been more recently characterized [108]. The exact same material used in [108] was used in this study. Samples were either powder, generated via a file, or small 5.8 mm diameter discs 0.33 ± 0.05 mm thick. The discs were obtained by using a laser cutter to cut thin slices of black PMMA from a larger block (6 mm thick). A punch tool is then used to make the discs from the thin strips. Discs were made thin to ensure the thermally-thin assumption of thermogravimetric analysis and so that sample masses (usually 11 mg) are close to those used in previous measurements (4–7 mg) [108]. Disc diameters correspond to the inner diameter of the crucibles and fill it completely so only the top is exposed. Powder samples were used so that oxygen can readily penetrate the sample to allow oxidation

throughout most (if not all) the sample. Disc samples were used to restrict oxidation to the top surface of the sample. Fig. 51 shows photos of the two types of sample geometry.

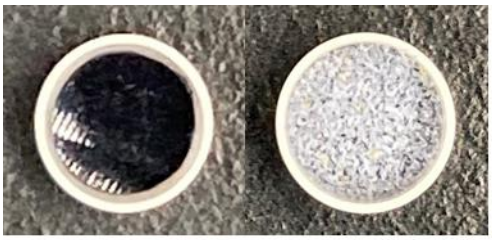

Fig. 51. Photos of TGA sample geometry. Disc on the left and powder on the right.

6.2.2 TGA tests in oxygenated environments

TGA tests were to be performed in nitrogen, 5 vol%, 10 vol%, and 20 vol% oxygen atmospheres. Nitrogen tests were performed only for the discs since tests using powder had been performed previously [108]; the nitrogen data serve as a baseline and to confirm the previously developed comprehensive pyrolysis model. 20 vol% oxygen was to represent air. 5 vol% and 10 vol% were chosen since they lie between these extremes and such concentrations were found at the sample surface in UL-94V tests during burner application, as described in section 4.10.3. These concentrations were created by flowing combination of nitrogen and oxygen gases in the proportions summarized in Table 16. However, these concentrations were later checked by sampling the gas from the exhaust and measuring oxygen concentration with a

calibrated paramagnetic sensor (in the same manner as section 4.3.2). The furnace was off and no sample was loaded during these measurements. Actual concentrations were consistently 0.5 vol% lower than nominal concentrations as reported in Table 16. The actual concentrations were used for CAPA tests and further analysis. The same settings as previous TGA tests were otherwise used: the heating rate was 10 K min^{-1}, the crucible was ceramic and without a lid, and sample mass was recorded as a function of time and temperature. DSC data was collected but not studied due to the poor sensitivity of the ceramic crucibles to heat flow and because the CAPA tests were to be used to evaluate if oxidative pyrolysis produces significant heat.

Table 16. Summary of gas flow rates for oxygenated atmospheres used in TGA tests

Nominal oxygen concentration [vol%]	**Nominal N_2 flow rate [mL min^{-1}]**	**Nominal O_2 flow rate [mL min^{-1}]**	**Measured oxygen concentration [vol%]**
0	50	0	0
10	54	6	9.5 ± 0.1
20	46	12	19.5 ± 0.1

6.3 CAPA II tests in oxygenated environments

6.3.1 Modifications to CAPA II and creation of oxygenated environments

To incorporate oxygen, a separate connection was made to introduce air at a controlled flow rate. Pressurized air flows from a wall connection through a silica gel desiccator to remove excess moisture prior to entering a 500 SLPM (standard liters per

minute) Alicat air mass flow controller which regulates the flow rate. Air flow meets nitrogen flow at a tee. Just before the tee is a shutoff valve which serves to isolate the air connection when testing in pure nitrogen so trapped air does not interfere. After the tee, the gases goes through large loops of 0.95 cm diameter copper tubing (approximately 3 m in length) to induce turbulence for better mixing. Fig. 52 is a photo showing the air connection.

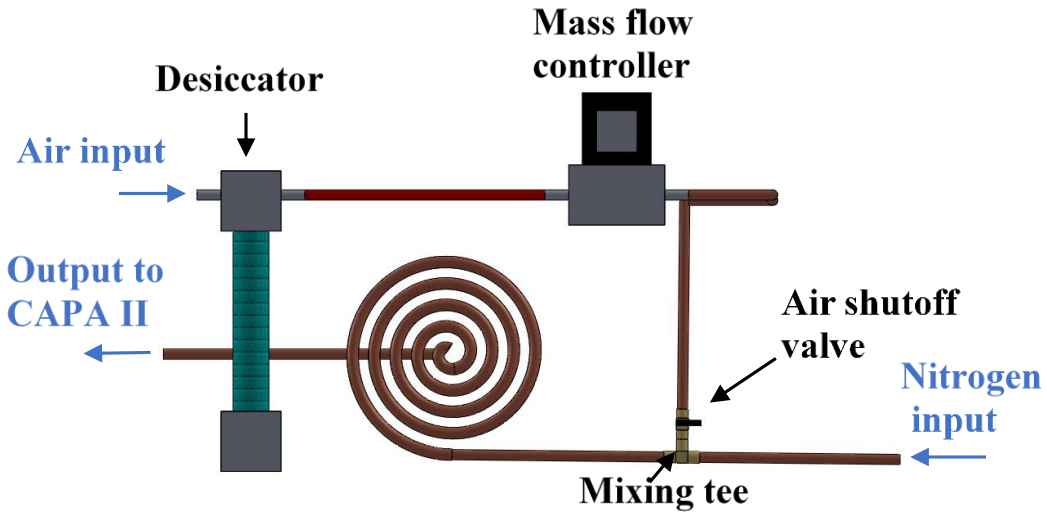

Fig. 52. Schematic of air connection added to CAPA. Not to scale. Support shelving also not shown for simplicity.

Oxygen concentrations were created by flowing air and nitrogen at specified flow rates while keeping the total flow rate 185 L min^{-1} to match previous testing. Oxygen concentrations were calculated assuming air comprises 20.95 vol% O_2. Oxygen concentrations were verified by sampling the gases at the top surface of a mock

sample, made of Kaowool PM insulation; the heater irradiation was set to 35 kW m^{-2} and slid into place to seal the sample chamber. The same gas sampling system described in section 4.3.2 was used with the only change being the sampling probe was longer (30 cm ceramic tube). The sampling probe was inserted through the top of the sample chamber i.e. through the empty center of the heating coil. Gases are then sampled at a flow rate of 100 mL min^{-1} (the limit of the sensor). Measured concentrations agreed well with nominal concentrations calculated from the flow rates as summarized in Table 17.

Table 17. Gas flow rates to create oxygenated atmospheres in CAPA II

Nominal oxygen concentration [vol%]	**Nitrogen gas flow rate [SLPM]**	**Air flow rate [SLPM]**	**Measured oxygen concentration [vol%]**
0	185	0	0.6 ± 0.2
9.5	84	101	9.5 ± 0.1
19.5	13	172	19.5 ± 0.1

6.3.2 Material and sample preparation

Samples were 7 cm diameter discs, 5.8 mm thick, cast black PMMA. The same black PMMA used in the TGA experiments (and used previously [108]) was used for the CAPA experiments. Thin copper foil (0.12 mm thick) is adhered to one side of the sample using light amount of epoxy. This foil is then painted with high temperature, high emissivity (0.92), black paint. Copper has a high thermal conductivity and the

layer is thin so the bottom temperature of the sample is more or less the temperature of the foil. The use of the foil facilitates clean up and allows for a surface with well-defined emissivity. Finally, rings of Kaowool are used to insulate the sides of the sample during tests. Fig. 53 shows photographs of an assembled CAPA II sample.

Fig. 53 Photographs of the top (left) and bottom (right) of an assembled CAPA II sample.

6.3.3 CAPA tests conditions for oxygenated environments

Two heat fluxes were used for the CAPA tests: 25 kW m^{-2} and 15 kW m^{-2}. 25 kW m^{-2} was used to enable comparison with the previous study which parameterized the black PMMA (anerobic) pyrolysis model while avoiding the risk of auto-ignition. A second heating condition was sought to evaluate the model further. Traditionally, this second heating condition is higher but that is not possible in this case without risking ignition so a significantly lower heat flux, 15 kW m^{-2}, was used instead. Two tests were performed for each concentration of oxygen (and nitrogen) at 25 kW m^{-2} as well as in 19.5 vol% O_2 for 15 kW m^{-2}. Only one test was performed for nitrogen and

4.5 vol% at 15 kW m^{-2} since they took over 120 minutes to complete after which the gas pipes become significantly chilled and begin to frost. Sample mass and back surface temperature are both measured over time with further details in the following sections. Additionally, thermocouple measurements monitored the temperature of the interior walls; such measurements are used to estimate their heat transfer contribution.

6.3.4 Mass measurements and calculations

Mass of the sample was measured via a Sartorius Cubis digital balance (1 mg resolution) at a rate of 2 Hz. Mass loss rate, MLR [kg m^{-2} s^{-1}], was calculated for each time step using a forward difference scheme and normalized by sample's top area. Then, data was smoothed using a moving average across 5 s for the 25 kW m^{-2} tests and across 10 s for 15 kW m^{-2}; a larger period was used for the 15 kW m^{-2} tests since the tests are much longer and because signal noise is more impactful when the MLR is lower. Data points were then assembled into 5 s and 10 s bins for 25 kW m^{-2} and 15 kW m^{-2} tests, respectively. Data in bins are averaged and error is estimated as two standard deviations of the mean. Repeated tests are binned together.

6.3.5 IR back surface temperature measurements and validation

Back surface temperature was measured by using a FLIR E40 IR camera at a rate of 7.5 Hz. The camera is not positioned underneath due to lack of space underneath

the sample (water cooling lines, connection to mass balance, gas flow inlet) but instead focuses on a gold mirror (average reflectance of 0.96) which reflects the radiation from the copper foil adhered to the bottom of the sample. From the IR video, temperature data was extracted at 12 points of varied radial location and then averaged together. The accuracy of this temperature measurement method was verified by heating a copper plate, painted with the same high emissivity high temperature black paint, under 25 kW m^{-2} irradiation and comparing the IR measurement with the measurements from thermocouples embedded into the copper plate. The results of this check can be found in section A4.2 of the appendix.

6.4 Numerical simulation and modeling for oxidation in TGA and CAPA tests

6.4.1 Anaerobic Black PMMA thermal decomposition reaction scheme

As discussed previously, a comprehensive pyrolysis model for cast, black PMMA was developed recently based on tests in nitrogen [108] and was used as a foundation for this work. Thermophysical properties: specific heats, density, thermal conductivities were unchanged. Reaction kinetics were subject to change as described further in the following sections. Given its importance to this work, the pyrolysis model is summarized here in Tables 18, 19, and 20. Table 18 summarizes the reaction scheme. Reaction 1 represents the glass transition of Black PMMA at 395 K (ThermaKin2Ds

specifies this limit)) which changes its thermal conductivity. Reaction 2 occurs at approximately 450 K wherein 2% of the PMMA decomposes into the gas and the rest to an intermediate. Finally, Reaction 3 is when the remaining black PMMA is converted almost entirely into gas. Fig. 54 shows the model versus the experimental data in N_2; data were supplied by Mr. Fiola. By design, the agreement is excellent.

Table 18. Black PMMA reaction scheme [108]

#	Reaction
1	BlackPMMA → BlackPMMA Glass
2	BlackPMMA Glass → 0.98 BlackPMMA Int + 0.02 BlackPMMA Gas
3	BlackPMMA_Int → 0.002 BlackPMMA Res + 0.998 BlackPMMA_Gas

Table 19. Black PMMA reaction kinetics and heats of reaction. Endothermic heats of reaction are marked as positive [108]

#	A [s^{-1} or m^3 kg^{-1} s^{-1}]	E [J mol^{-1}]	H [J kg^{-1}]
1	1	0	0
2	4.95×10^{16}	1.64×10^5	5×10^3
3	1.35×10^{11}	1.64×10^5	8.17×10^5

Table 20. Black PMMA component properties [108]

Component	ρ [kg m^{-3}]	ε	κ [m^2 kg^{-1}]	k [W m^{-1} K^{-1}]	c [J kg^{-1} K^{-1}]
Black PMMA	1210	0.96	2.38	0.16	-1390 + 8.33 T
Black PMMA Glass	1210	0.96	2.38	0.34 – 4.2 $\times 10^{-4}$ T	851 + 3.07 T
Black PMMA Int	1210	0.96	2.38	0.34 – 4.2 $\times 10^{-4}$ T	851 + 3.07 T
Black PMMA_Res	1210	0.96	2.38	0.34 – 4.2 $\times 10^{-4}$ T	851 + 3.07 T

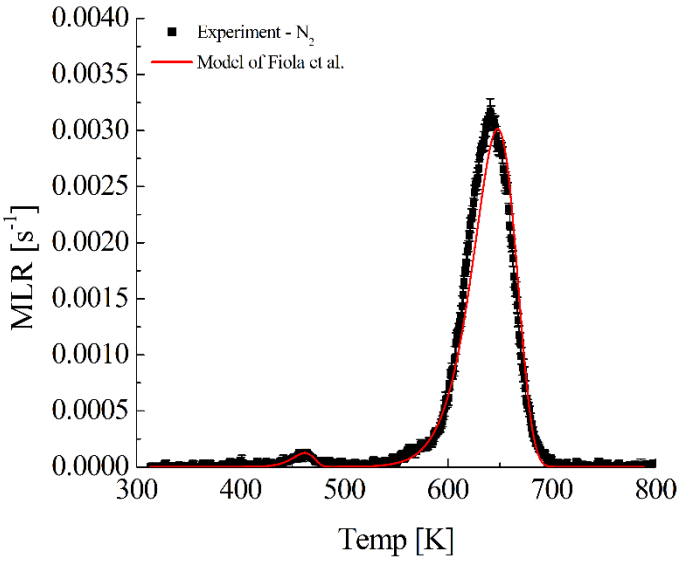

Fig. 54. Plot showing thermal decomposition model and experimental data done in N_2.

6.4.2 Simulation parameters for TGA

One-dimensional geometry ThermaKin2Ds was used to model the TGA experiments. Samples were assumed to be thermally thin and were represented by a single element. Simulations of powder had an arbitrary thickness of 0.01 mm since their results were normalized by initial mass (effectively thickness). Simulations of discs had a thickness of 0.33 mm to match the experiment since their results are not normalized by mass; the simulated sample was still a single element. The element was forced to follow the experimental temperature program by defining a very high convective coefficient at the boundary (100 kW m^{-2} K^{-1}). The heating rate was defined by an exponentially decaying sinusoidal function to capture the experimental heating

rate [96]. Gaseous components were assumed to leave the element instantaneously. An additional surface reaction was applied when simulating the discs, as described in section 6.4.4.

6.4.3 Automated inverse analysis for volumetric decomposition of powders

Previously, Fiola developed a methodology and algorithm to automate inverse analysis of TGA data to determine reaction kinetics [108,109]. Full details on how the algorithm operates are described in [109] but a brief overview is given in section A4.1. This methodology had been successfully applied to simple polymers in N_2, including cast, black PMMA, as well as rigid polyisocyanurate foam which had several decomposition steps. This work used the program to automate inverse analysis of the powder tests performed in oxygenated environments to derive revised kinetic parameters.

6.4.4 Iterative inverse analysis for surface oxidation of discs

For the discs, the pyrolysis model described in 6.4.1 was not altered but instead supplemented by a surface reaction of the form $J = C\ \exp(-D/RT_B)$ much like what was described in section 4.10.3. The terms are J is the area-normalized MLR to the gas phase [kg m^{-2} s^{-1}], T_B is the temperature at the boundary [K], R is the universal gas constant [J mol^{-1} K^{-1}], and C [kg m^{-2} s^{-1}] and D [J mol^{-1}] are effectively a pre-

exponential factor and activation energy [24]. C and D were determined by inverse analysis until model-predicted mass flux best matched experimental results. Note that only the mass flux leading up to the peak were considered since the sample shape is likely compromised beyond the temperature of peak MLR. Unfortunately, the automated method cannot be used so iterative guessing of the kinetic parameters was required. A more detailed description of this process can be found in section A4.1.

6.4.5 Simulation parameters for CAPA

CAPA II tests were simulated using the 2D-axisymmetric module of ThermaKin2Ds. Simulated samples were PMMA discs of 3.5 cm radius, 5.8 mm thickness, as to match the experiment. At the bottom is the copper foil, assumed to be 0.05 mm thick. The copper layer does not participate in any reaction but is there to emulate the back surface temperature. Properties of copper were taken from [85]. Element size was 5×10^{-5} m and timestep was 0.01 s. Gaseous components were assumed to exit without resistance. The convective and radiative boundary conditions associated with the irradiation of the heater and transfer between the top and bottom surface of the sample with the chamber walls were explicitly implemented. More detail about the boundary conditions can be found in appendix A4.3. Finally, the largest uncertainty in the pyrolysis parameter set is the specific heat [110] which has an

uncertainty of up to 10%. Specific heats were increased by 10% to better fit the CAPA data to facilitate comparison.

6.5 Oxygenated TGA results and modeling

6.5.1 Experimental results for powders

TGA mass data were used to calculated mass loss rate, MLR [s^{-1}], normalized by initial sample mass. Overall, the addition of oxygen shifts decomposition to lower temperatures; both the onset and location of peak MLR occur at lower temperatures, as shown in Fig. 55. However, peak MLR is slightly smaller, but wider, when oxygen is included relative to the data in N_2. Increasing the concentration of oxygen increases peak MLR but does not seem to change the peak temperature or the onset of mass loss. Additionally, Reaction 2 which is found in the nitrogen data at 450 K was largely absent from all tests done with oxygen.

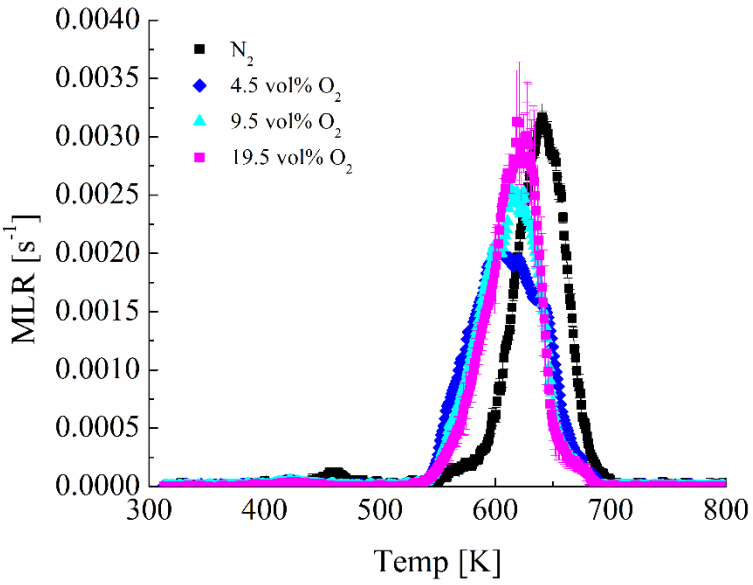

Fig. 55. Experimental TGA results for powdered black PMMA.

6.5.2 Modeling results for powders: derivation of volumetric kinetics

Since no additional mass loss rate peaks were seen, the same reaction scheme as Fiola [108] was used but with the kinetic parameters of reaction 3 redetermined; reaction 3 is responsible for the large, second peak. For simplicity, reaction 2 was left unchanged. The results of the parameterization are shown graphically in Fig. 56 for all concentrations and are summarized in Table 21. The gas yield for reaction 3 was 0.97 (mass-based) for all concentrations.

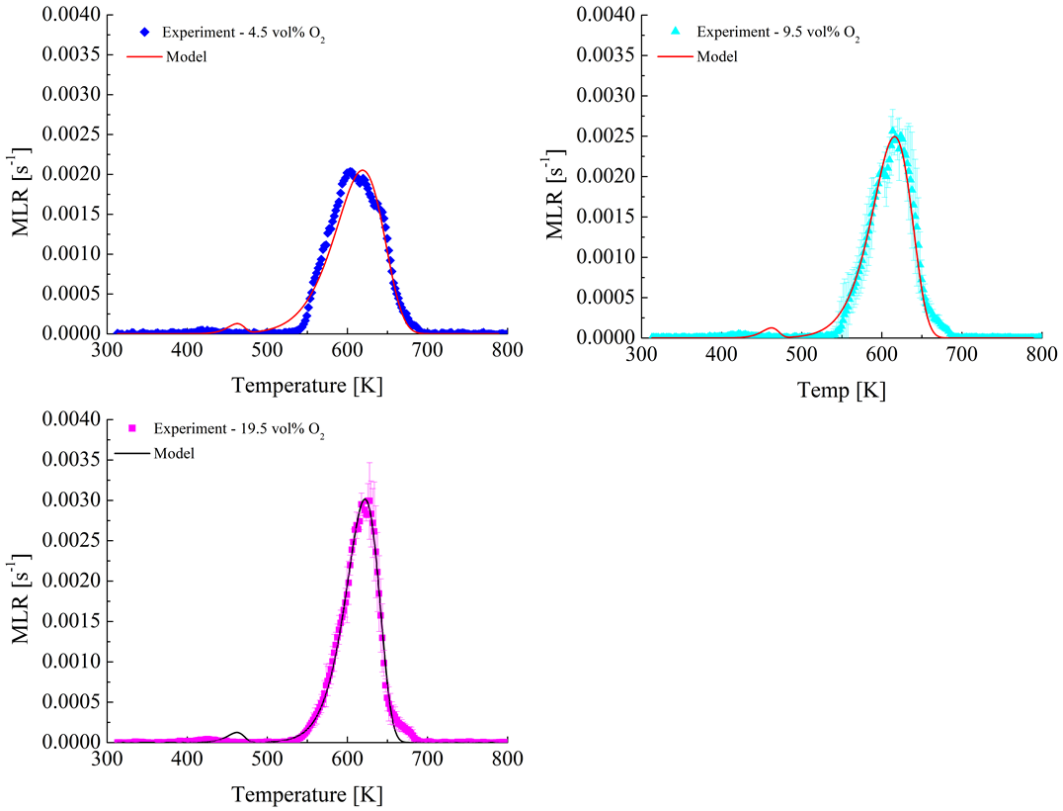

Fig. 56. Comparison of experimental and model MLR for all tested O_2 concentrations in TGA tests.

Table 21. Summary of oxidative kinetics for reaction 3 (see Table 18).

Oxygen concentration	***A* [s^{-1}]**	***E* [J mol^{-1}]**
4.5 vol%	1.44×10^6	1.00×10^5
9.5 vol%	1.69×10^8	1.23×10^5
19.5 vol%	3.98×10^{10}	1.51×10^5

Looking at the values in Table 21 both the pre-exponential factor and activation energy increase with increasing O_2 concentration. The increase in pre-exponential factor is reasonable since it represents collision frequency which would likely be higher when the concentration of oxygen is increased. The increase in activation energy is unexpected however, that may be an artefact of the inverse analysis. Activation energy and pre-exponential factor are closely related and can compensate for one another [111,112]. There are not many studies which determined the kinetics of thermal decomposition of PMMA in air let alone partially oxygenated environments. However, Peterson et al. [113] did report activation energies for single-step thermal degradation of PMMA in N_2 and air and found that the activation energy for N_2 was $1.5 – 2.5 \times 10^5$ J mol^{-1} and $6 –7 \times 10^4$ J mol^{-1} for air. This value is significantly lower than that derived for the 19.5 vol% O_2 tests. Again, compensation of the pre-exponential factor may be responsible; Peterson et al. did not report pre-exponential factors. Finally, to elucidate any trends, the kinetics parameters were plotted versus O_2 concentration as shown in Fig. 57. Since *A* varies by orders of magnitude, a semi-log plot was used. A strong linear trend is seen for both kinetic parameters as O_2 concentration increases. These trend lines can be used to estimate the kinetics of other concentrations. Note that for these fits, the plotted oxygen concentrations are that of the input gas mixture while

oxygen concentrations near and within the sample may be significantly different due to the evolved gases.

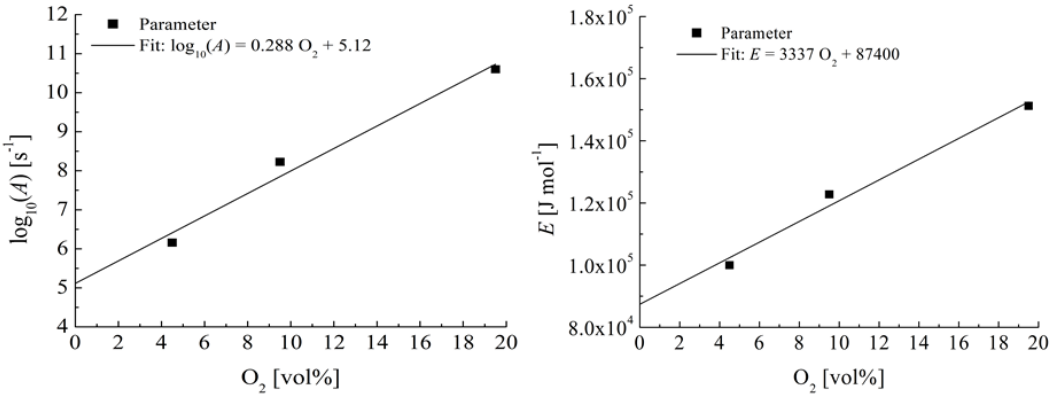

Fig. 57. Plots comparing volumetric kinetic parameters versus oxygen concentration.

6.5.3 Experimental results for discs

TGA mass data was used to calculated MLR which was then normalized by the top area of the disc. As shown in Fig. 58, like the powder data, disc samples show a significant shift to lower temperature for the onset of decomposition and peak mass flux when oxygen is introduced. Also like the powder data, the initial onset temperature (~550 K) was about constant for all tested concentrations and no significant reaction peak is seen at 450 K. However, unlike the powder data, the temperature of peak mass flux varied with oxygen concentration. Most notably, the temperature of peak mass flux for tests in 4.5 vol% O_2 nearly matches that of the nitrogen data while the other concentrations have a peak at lower temperature. Additionally, the magnitude of peak

mass flux showed no obvious relationship with oxygen concentration. Tests at 4.5 vol% O_2 and 19.5 vol% O_2 have similar peaks while the peak of 9.5 vol% O_2 is lower and the peak of the N_2 tests is higher.

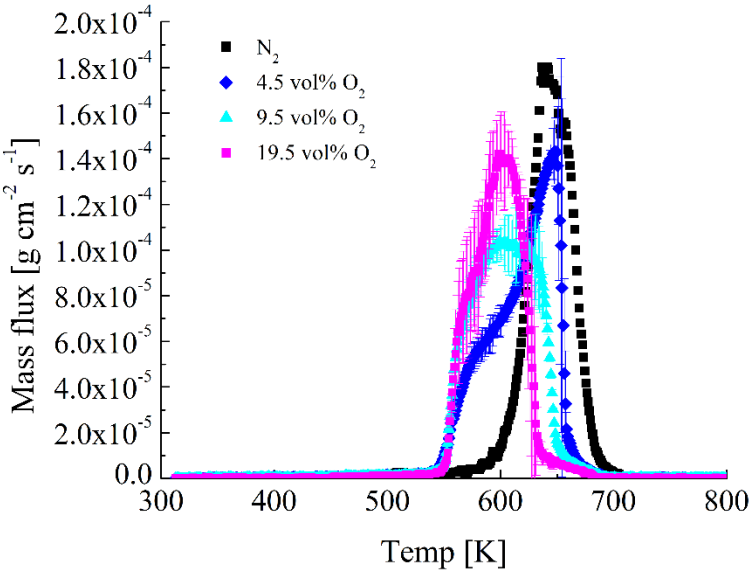

Fig. 58. TGA mass flux results for black PMMA discs in varied O_2 concentration.

6.5.4 Modeling results for discs: derivation of surface reaction kinetics

The activation energy of the surface reaction, D, which gave the best fit of experimental data was approximately constant for all concentrations and found to be 9.0×10^4 J mol^{-1}. The pre-exponential factor, C, was found to increase with increasing oxygen concentration, as summarized in Table 22. The resulting model predictions were mixed shown in Fig. 59. The model underpredicts initial mass flux of the 4.5 vol%

O_2 test but overpredicts the initial mass flux of 9.5 and 19.5 vol% O_2. Predicted mass flux at higher temperatures are reasonably good for 4.5 vol% and 19.5 vol% O_2 but less so for 9.5 vol% O_2.

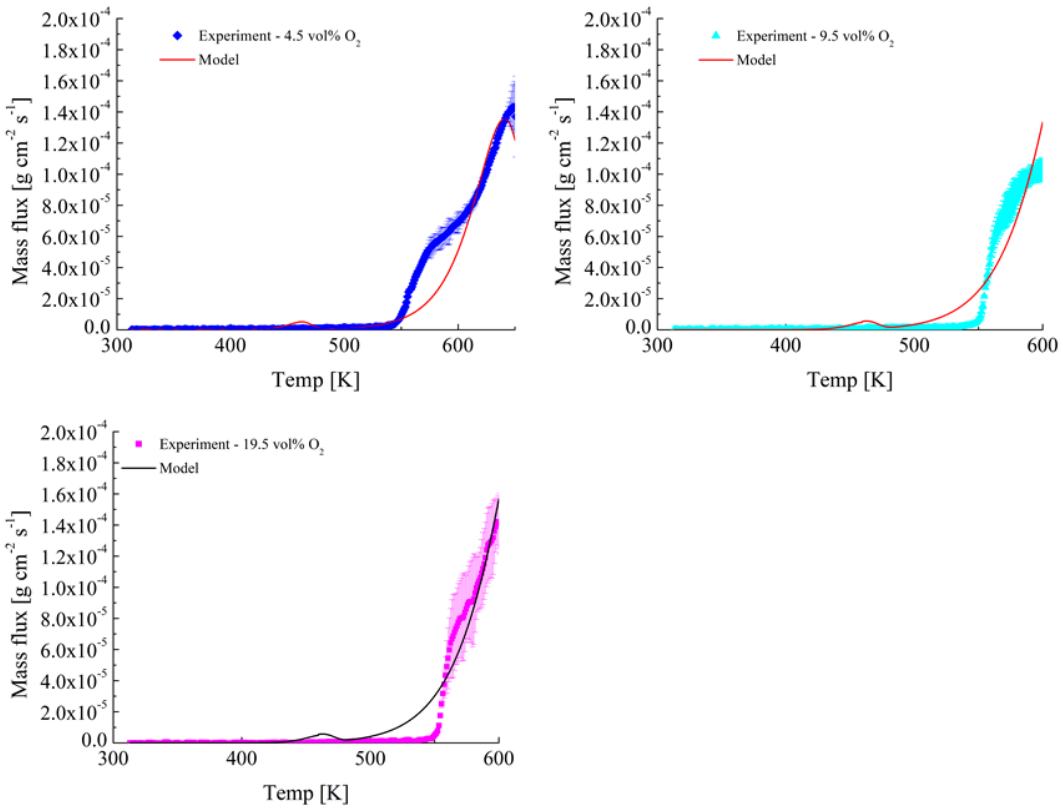

Fig. 59. Comparison of experimental and model MLR for all tested O_2 concentrations in TGA tests.

Table 22. Summary of kinetics for oxidative surface reaction

Oxygen concentration	***C*** **[g cm^{-2} s^{-1}]**	***D*** **[J mol^{-1}]**
4.5 vol%	2.00×10^3	9.0×10^4
9.5 vol%	8.40×10^3	9.0×10^4

19.5 vol%	1.02×10^4	9.0×10^4

Finally, to determine if there was a trend, C was plotted versus O_2 concentration as shown by Fig. 60; the intercept was set to 0 since that would correspond to a test in nitrogen which would not have a surface reaction. Much like the powders, these oxygen concentrations are based on the incoming flow and may not accurately reflect oxygen content at the sample surface due to evolving gases. There is a reasonable linear trend with oxygen concentration, so kinetics can be estimated for other concentrations.

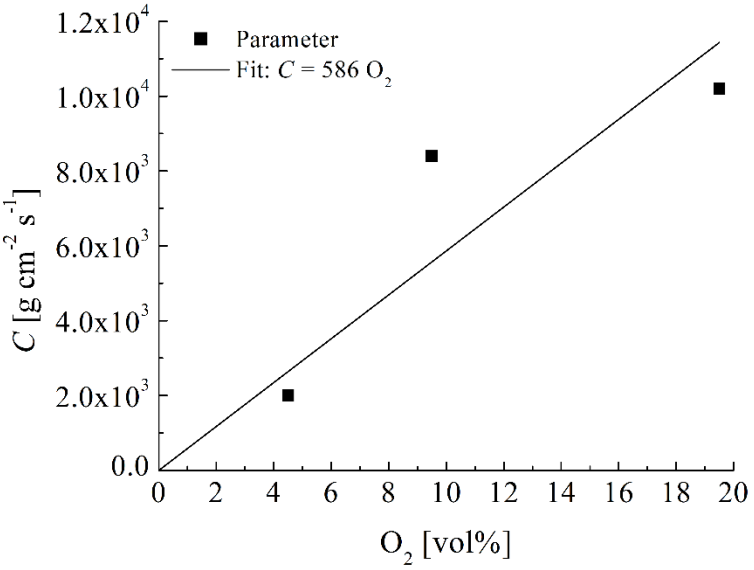

Fig. 60. Plots comparing the surface reaction pre-exponential factor versus O_2 concentration.

6.6 Oxygenated CAPA II results and model performance

6.6.1 CAPA II experimental results

Beginning with the MLR results, as oxygen content increases, the peak and quasi-steady MLR increase as shown in Fig. 61 for 25 kW m^{-2} in Fig. 62 for 15 kW m^{-2}. Additionally, the curves appear to be shifted to earlier times, i.e. the onset of MLR occurs sooner. This contrasts with the TGA results which saw no clear trends in peak MLR with oxygen concentration and a similar onset temperature for all concentrations; however, the TGA results are plotted versus temperature so perhaps direct comparison is inappropriate. Additionally, the 4.5 vol% and N_2 MLR data are close for the 15 kW m^{-2} test and seemingly overlap for the 25 kW m^{-2} test. Again, this is contrast to the TGA results which saw large separation between N_2 data and any of the tests with oxygen. However, when focusing on the first ~10% of the test (first 200 s of 25 kW m^{-2}, first 800 s of the 15 kW m^{-2}) as shown in Fig. 63 and 64, there is noticeable separation between the 4.5 vol% O_2 and N_2 data on the order of 10 s for the 25 kW m^{-2} test but little to no separation for 15 kW m^{-2}. This can explain why 4–5 vol% O_2 can significantly impact predictions of ignition time in UL-94V simulations (heat flux on the order of 50 kW m^{-2}, relative to a cold surface) even though the 4.5 vol% O_2 data is otherwise similar to the N_2 data.

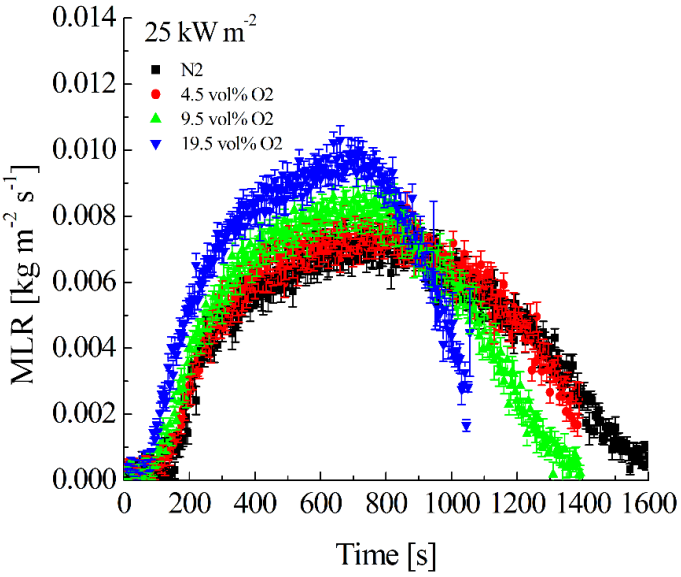

Fig. 61. CAPA II MLR data for varied oxygen concentrations under 25 kW m^{-2} irradiation.

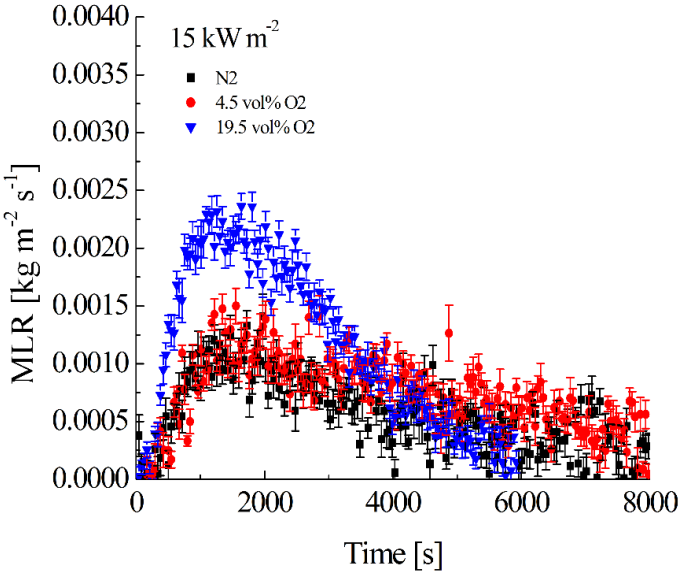

Fig. 62. CAPA II MLR data for varied oxygen concentrations under 15 kW m^{-2} irradiation. No data are available for 9.5 vol% O_2 due to limited resources.

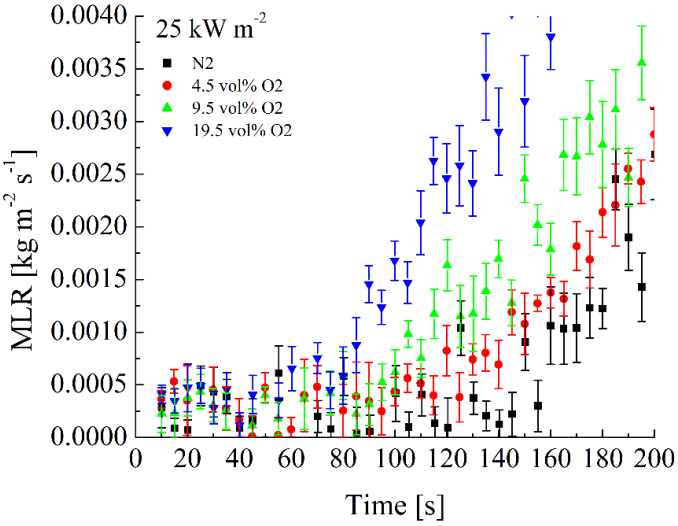

Fig. 63. CAPA II MLR data for varied oxygen concentrations under 25 kW m^{-2} irradiation in the first 200 s.

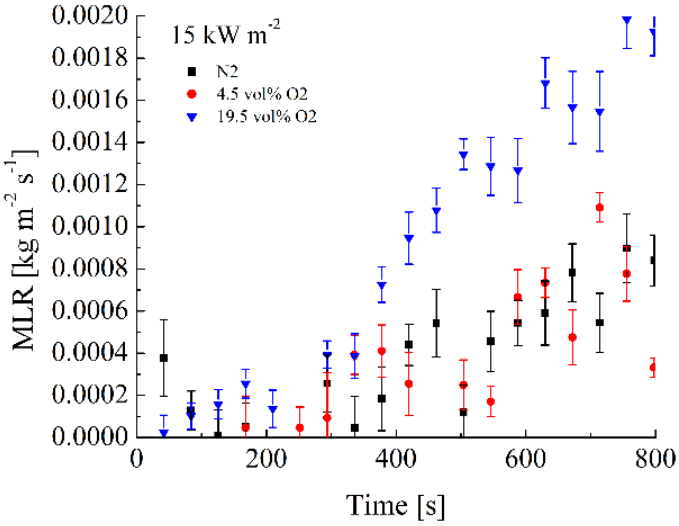

Fig. 64. CAPA II MLR data for varied oxygen concentrations under 15 kW m^{-2} irradiation in the first 800 s.

As for the temperature data, oxygen does not appear to have a significant impact on back surface temperature, T_{back} as shown in Fig. 65 and 66 for 25 and 15 kW m^{-2}, respectively. The plots are cut off at 800 s and 4000 s for 25 and 15 kW m^{-2}, respectively, because comparison for the different concentrations at later times is inappropriate due to significant differences in sample thickness due to differences in integral mass loss; the tests at higher oxygen concentrations begin to diverge since the sample becomes significantly thinner. Prior to this, the T_{back} data overlap for all oxygen concentrations for both heat fluxes. Given that T_{back} data do not vary with oxygen concentration, it is concluded that the oxidative pyrolysis of black PMMA does not significantly produce nor remove heat so no change will be made to the pyrolysis model in this regard.

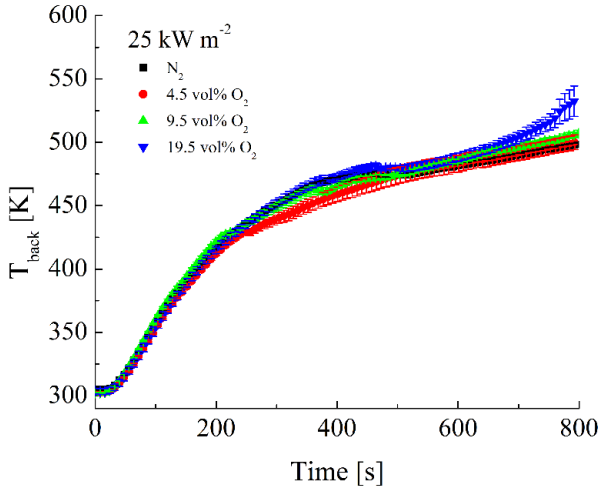

Fig. 65. CAPA II T_{back} data for varied oxygen concentrations under 25 kW m^{-2} irradiation.

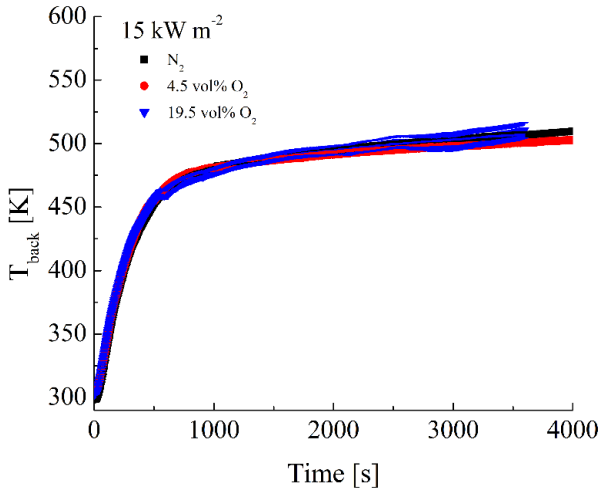

Fig. 66. CAPA II T_{back} data for varied oxygen concentrations under 15 kW m^{-2} irradiation.

6.6.2 Model performance for 25 kW m^{-2} CAPA II tests

Fig. 67 shows the model predictions for MLR for 25 kW m^{-2} for all tested atmospheres. Beginning with the test in N_2, agreement between model predictions and experiment is good and is within experimental uncertainty for most of the test. This further validates the pyrolysis parameter set and the experimental methods. For the tests with oxygen added, three models are presented. The surface model are simulations with the surface reaction parameterized for the mass flux of the discs in TGA tests but the pyrolysis model otherwise unchanged. The volumetric model has no additional reaction, but the kinetics of thermal decomposition are changed to match the normalized MLR of the powders in TGA tests. Finally, the nitrogen model is the original model without making any changes to serve as a reference. As for model

performance, neither model particularly improves prediction of the MLR data for 4.5 vol% O_2, compared to the nitrogen model. However, the volumetric model better predicts peak MLR for the 9.5 vol% O_2 test but does overpredict early MLR. The volumetric model is also a significant improvement for 19.5 vol% O_2 test and matches the MLR well. The surface model, however, consistently overpredicts MLR and does not present any significant improvement in MLR predictions apart from maybe 19.6 vol% O_2 when compared to the nitrogen model.

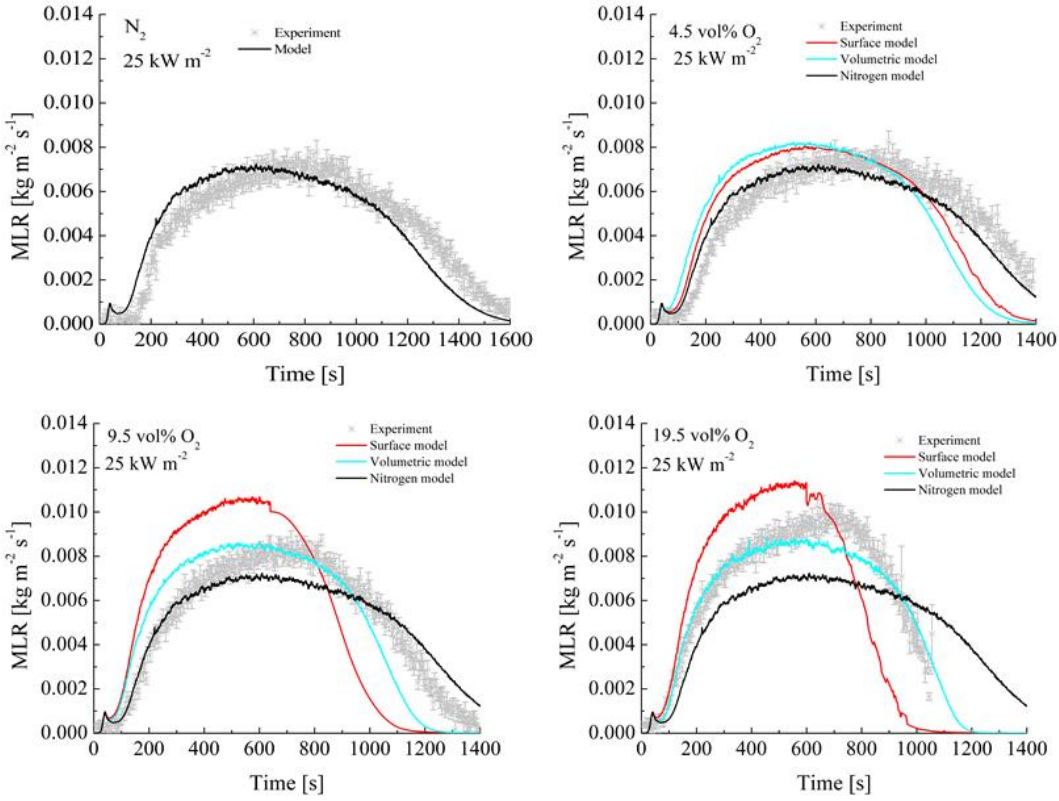

Fig. 67 Comparison of experimental and model predictions of MLR in CAPA II tests for varied oxygen concentrations and 25 kW m^{-2} irradiation.

After comparing model predictions for T_{back} with experimental results, a systematic error in the T_{back} measurements was revealed. Using the T_{back} data for 25 kW m^{-2}, a direct comparison was made with the original model and the data of Fiola [108] which is shown in Fig. 68. As shown, agreement is excellent until T_{back} reaches 475 K above which a dip in T_{back} data is seen and a growing discrepancy emerges. This drop in temperature was also seen for all other tests, creating a discrepancy as shown

in Fig. 68 for the comparison of the 15 kW m^{-2} nitrogen results. The calibration of the heat flux gauge, the heat flux of the heater, and the IR camera settings were all verified to be proper. It is believed that the discrepancy is due to a separation of the sample from the copper foil by failure of the epoxy. All samples were prepared at the same time, so it was quite possible to repeatedly fail to apply sufficient epoxy. No further comparison or analysis of T_{back} data will be presented given this systematic error and given that the experimental results indicated that oxidative pyrolysis does not generate or consume significant heat.

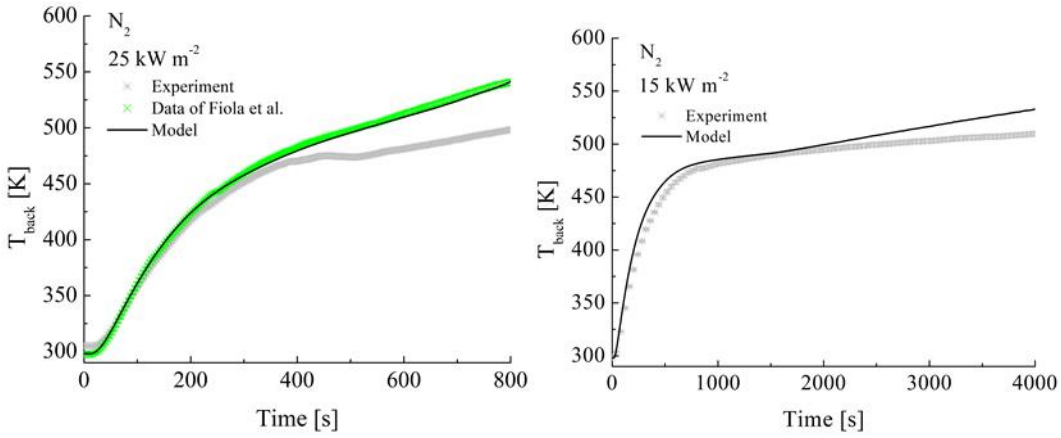

Fig. 68 Comparison of experimental and model predictions of T_{back} in CAPA II tests for nitrogen tests. A systematic discrepancy was identified at 475 K.

6.6.3 Model performance for 15 kW m^{-2} CAPA II tests

Fig. 69 shows the model predictions for MLR for 15 kW m^{-2} for all tested atmospheres. Beginning with the test in N_2, agreement between model predictions and

experiment is quite good, further validating the pyrolysis parameter set. For the 4.5 vol% O_2 test, neither model provides any improvement compared to the N_2 model and for once, the volumetric model has a worse prediction than the surface model. The predictions for the 19.5 vol% O_2 test are significantly improved, however, using the volumetric model while the surface model again overpredicts MLR.

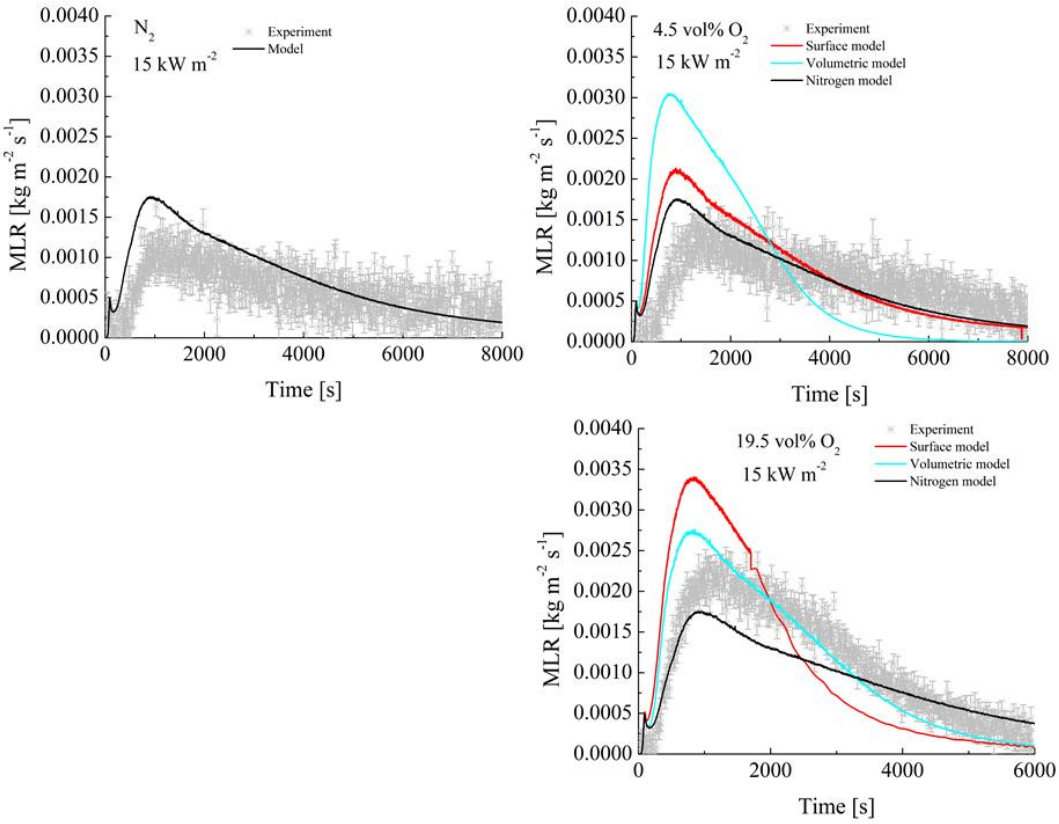

Fig. 69 Comparison of experimental and model predictions of MLR in CAPA II tests for varied oxygen concentrations and 15 kW m^{-2} irradiation.

6.6.4 Accounting for mass transport of oxygen

The surface model showed a tendency to consistently overpredict MLR, particularly for tests at the higher heat flux. Since the pre-exponential factor of the surface model is proportional to oxygen content, the model's predictions are also proportional to oxygen content. Thus, perhaps overprediction is due to the assumption that the oxygen content available to the pyrolyzing solid is equal to that of the gas flow composition in the test chamber. Due to the evolving gases and elevated temperature, diffusion may become significant. There could be a concentration gradient between the sample and the surrounding gas mixture. To explore this possibility, an analysis was performed to estimate the volumetric concentration at the surface of the sample for each test condition. The diffusive mass flux of a species is given by Equation (16) [114] where $\dot{m}_i''$ is the mass flux of the species [kg m^{-2} s^{-1}], K is the mass-transfer coefficient [m s^{-1}], and ξ_1 and ξ_2 are the mass concentrations between the interface [kg m^{-3}].

$$\dot{m}_i'' = \mathrm{K}(\xi_1 - \xi_2) \qquad (16)$$

ξ_1 can be calculated given the known volumetric concentration at the inlet and the ideal gas law re-arranged to form Equation (17) where P is the pressure [Pa] assumed to be 101325 Pa (atmospheric), X is the volume fraction, MW is the molecular weight [kg mol^{-1}] of the gas, 32×10^{-3} for O_2 , R is the universal gas constant [J mol K^{-1}], and T is

the temperature. Thermocouple measurements of the gas inlet found the steady-state temperatures to be 323 K and 333 K for 15 kW m^{-2} and 25 kW m^{-2} tests, respectively.

$$\xi = \frac{P \text{ X } MW}{R\ T} \quad (17)$$

If $\dot{m}_i''$ and K can be estimated, ξ_2 (and X_2 by extension) can be determined for the oxygen at the sample surface. A rough estimate for $\dot{m}_i''$ was obtained based on one of the proposed reaction mechanisms of Kashiwagi et al. [51] for the thermo-oxidative degradation of PMMA. This proposed mechanism suggests one mol of O_2 splitting two mols of MMA at so-called weak linkages. These weak linkages are estimated to account for approximately 30% of the polymer (by mass). Based on this information, the diffusive mass flux was estimated by multiplying the steady-state mass flux of the experiments by 0.3 and by the mass ratio of one mol of O_2 to two mols of MMA.

Table 23. Average, peak experimental mass flux and estimated mass flux of oxygen in CAPA II tests

$\dot{m}_{exp}''$ ($\dot{m}_{o2}''$) [kg m^{-2} s^{-1}]	15 kW m^{-2}	25 kW m^{-2}
4.5 vol%	0.0011 (5.27×10^{-5})	0.0071 (3.39×10^{-4})
9.5 vol%	n/a	0.0079 (3.74×10^{-4})
19.5 vol%	0.002 (9.72×10^{-5})	0.009 (4.63×10^{-4})

K was estimated based on a relationship between heat and mass transfer given by Equation (18) [114] where h is the convective heat transfer coefficient which was determined to be, on average, 7.2 W m^{-2} K^{-1} based on CFD simulations of CAPA [115],

ρ and c_p are the density and specific heat which were assumed to be equal to the density of air [114], Pr is the Prandtl number of air, and Sc is the Schmidt number for oxygen in air [114]. Any blowing effect (change in convection due to outward mass flux of gaseous pyrolyzates) was not explicitly considered in this analysis. The result of this calculation is shown in Table 24.

$$\mathrm{K} = \frac{h}{\rho c_p}\left(\frac{Pr}{Sc}\right)^{2/3} \qquad (18)$$

Table 24. Estimated effective volumetric concentrations of oxygen at the sample surface for CAPA II tests.

	15 kW m^{-2}	25 kW m^{-2}
4.5 vol%	3.9	0.5
9.5 vol%	n/a	5.0
19.5 vol%	18.3	14.3

As Table 24 shows, the oxygen concentration at the sample may be significantly less than the volumetric concentration of the incoming gas flow, particularly for higher heat fluxes. Although these values are based on speculation, they do seem reasonable and align with the trends seen in the experimental data of Fig. 61 and Fig. 62. For instance, the N_2 and 4.5 vol% O_2 MLR data overlapped in 25 kW m^{-2} tests but not in the 15 kW m^{-2}. This analysis suggests the oxygen concentration at the surface may effectively be 0.5 vol% for the 25 kW m^{-2} which would be close to anaerobic conditions which would explain the overlap. Using the estimated volumetric concentrations of Table 24 along

with the fits for the kinetic parameters in Fig. 57 and Fig. 60, the kinetic parameters for the surface and volumetric models can be re-calculated and then used to re-simulate CAPA II tests.

6.6.5 Model performance accounting for mass transport

The results using the revised kinetic parameters to account for mass transport are given in Fig. 70 for 25 kW m^{-2} and Fig. 71 for 15 kW m^{-2}. In the legends, in parentheses, is the effective volumetric oxygen that was calculated for each test. For the 25 kW m^{-2} results, using the revised kinetics significantly improved predictions by the surface model but resulted in little to no changes in the volumetric model. For the volumetric model, due to the complex coupling between the activation energy and pre-exponential factor, the reduction in pre-exponential is balanced by a reduction in activation energy resulting in only small changes in predicted MLR. On closer inspection, the volumetric model shows only small increases in predicted MLR with increasing oxygen concentration (from 0.0081 to 0.0087 kg m^{-2} s^{-1}) when comparing the 4.5 vol% and 19.5 vol% O_2 predictions (without considering mass transport). Thus, the volumetric model is not sensitive to oxygen concentration which would explain why when accounting for mass transport predictions do not noticeably change. The

surface model, with its kinetics revised based on the mass transport analysis, now gives the best predictions of all models for all oxygen concentrations for 25 kW m^{-2}.

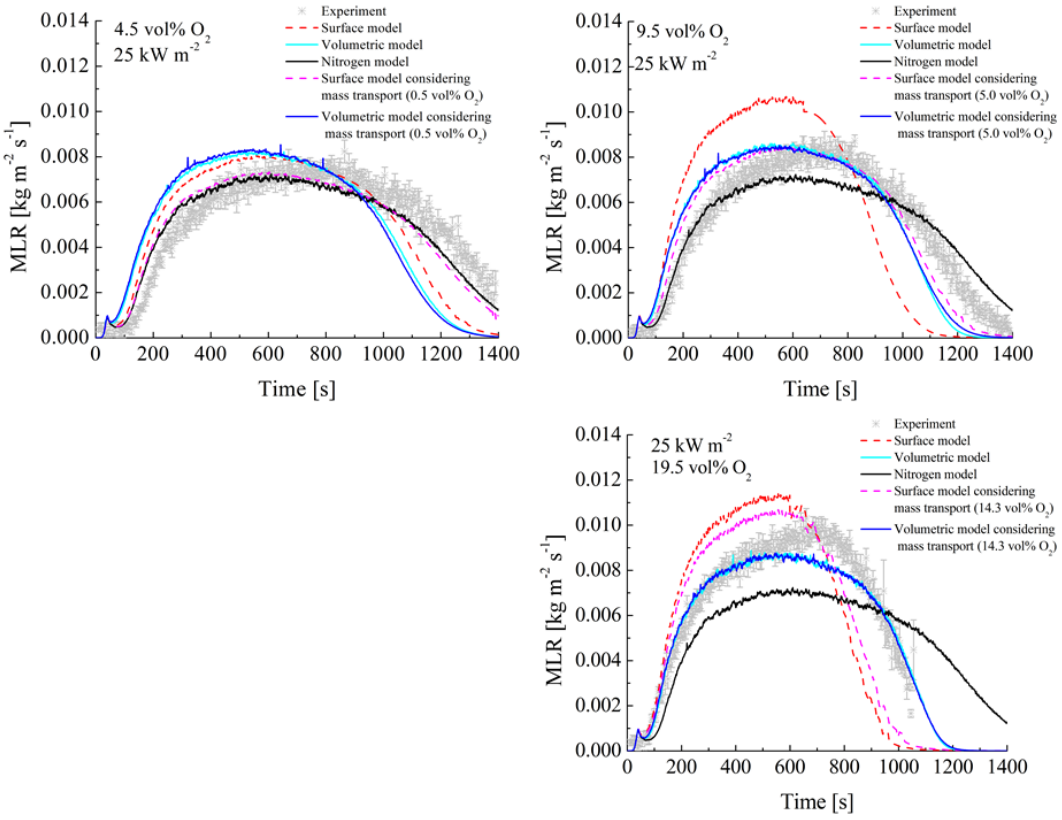

Fig. 70. Comparison of experimental MLR in CAPA II tests for varied oxygen concentrations and 25 kW m^{-2} irradiation with model predictions considering mass transport.

However, for the 15 kW m^{-2} tests, predictions by both models are largely unchanged since the estimated reduction in oxygen concentration is small. The surface model shows a very slight decreased in predicted MLR whereas the volumetric model actually showed a slight increase in predicted MLR due to the complex coupling of the

pre-exponential factor and activation energy. The nitrogen model still provides the best prediction for both 15 kW m^{-2} tests, although the volumetric model predicts MLR after 2000 s reasonably well for 19.5 vol% O_2.

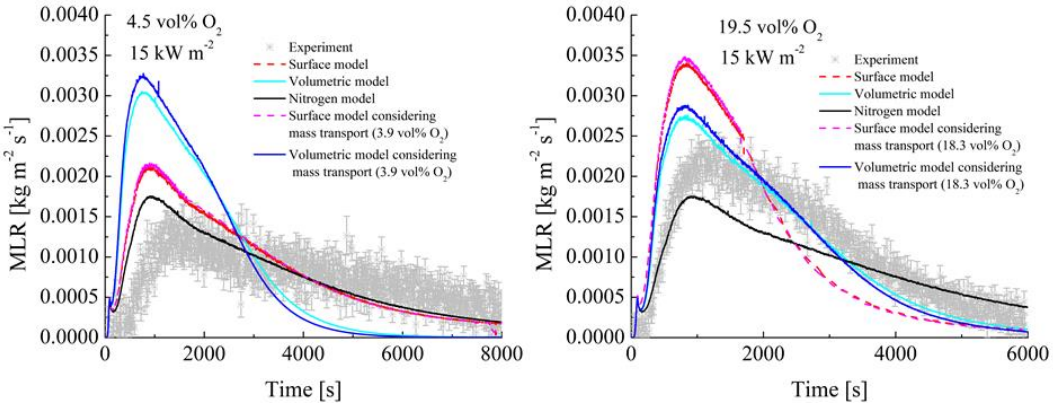

Fig. 71. Comparison of experimental MLR in CAPA II tests for varied oxygen concentrations and 15 kW m^{-2} irradiation with model predictions considering mass transport.

6.6.6 Final comments on model performance

The results of the 15 kW m^{-2} tests indicate that the pyrolysis model developed in nitrogen can best predict MLR in oxygenated environments (up to 19.5 vol%). This suggests that for sufficiently low incident heat flux, an anaerobic model can predict pyrolysis in an aerobic environment with reasonable accuracy. For the 25 kW m^{-2} tests, the nitrogen model is no longer sufficient and an oxidative kinetic model gives better results. However, which oxidative model gives better predictions for 25 kW m^{-2} tests depends on whether mass transport is considered or not. If mass transport is considered

and the calculation is correct, the surface model performs quite well, which would support oxidation occurring primarily occurring at the sample surface. However, if mass transport is not considered or if the correction is incorrect, the volumetric model gives better predictions. More detailed measurements and analysis are needed to fully understand the mechanisms of oxidative pyrolysis and which type of oxidative model is more appropriate.

Chapter 7: Concluding remarks

7.1 Cone calorimeter study conclusions

1. The heat flux was measured in the center and near one side in cone calorimeter tests. Measurements near the side were 2.0–3.8 times greater than in the center.
2. The flame was thinner and closer to the sample surface near the sides of cone calorimeter samples.
3. A two-zone model was developed for the flame heat feedback of the cone calorimeter test with the center having a radiative portion and the side dominated by convection.
4. Estimates of the convective heat flux were used to determine the size of the zones. The center zone was estimated to be about 29% of the area and 71% for the side zone.
5. Predicted average HRR and peak HRR were within 1.4 – 34.4% (≈16% on average) of experimental results
6. Time to ignition predictions were significantly off since the pyrolysis model does not account for enhanced decomposition due to oxidation. A simple correction was subsequently made using thermally-thick ignition theory.

7.2 UL-94V study conclusions

1. The heat flux, temperature, and oxygen content of the UL-94V burner flame were characterized spatially using a noncombustible mock sample. Burner heat flux was determined to be primarily convective and a piecewise, linear expression was developed for it, the first of its kind.

2. UL-94V tests were conducted using several polymers with and without insulated sides to investigate edge effects: pyrolysis, flaming, and spread on the edges of the sample. The dynamics of flame spread on these samples were successfully captured using analysis of videos recorded with a 900 nm filter.
3. Burner flame oxygen content was about 5 vol%. TGA tests conducted in a 5 vol% O_2 (balance N_2) atmosphere showed that oxidation is significant for PMMA and HIPS at this concentration; an oxidation submodel was developed based on inverse analysis of these tests.
4. PMMA flame heat flux was measured using insulated and non-insulated samples and was found to be about 26.5% greater on non-insulated samples. The increase in flame heat flux was attributed to an observed 27% reduction in average flame standoff distance. The flame heat feedback submodel was scaled accordingly.
5. The conditions of the UL-94V test characterized in this work were combined with a previously developed pyrolysis submodels and a previously developed laminar wall flame heat feedback submodel to simulate the UL-94V test of both insulated and non-insulated samples for a range of materials.
6. The simulation of the insulated samples predicted flame length and rate of flame spread well for most materials, validating the submodels used.
7. The simulations of the non-insulated samples predicted rate of spread reasonably well but significantly underpredicted flame length despite the flame heat feedback submodel being scaled up. This discrepancy was attributed to the edge effects.

8. The results suggest that insulating the sides of narrow samples reduce the influence of the edge effects such that the flame spread is more two-dimensional in nature and, thus, more susceptible to physical interpretation.
9. The model, however, cannot predict gaseous flame inhibition and consequently, failed to predict test outcome for materials for which this inhibition is significant.

7.3 Oxidative pyrolysis study conclusions

1. Oxidative pyrolysis of black PMMA was studied in milligram and gram-scale experiments. Milligram scale experiments were used to determine kinetic parameters for either a surface reaction or a volumetric reaction for a range of oxygen concentrations.
2. Gram-scale CAPA II experiments showed slightly different trends than TGA experiments. Differences in the onset of decomposition between oxygenated and nitrogen tests were less pronounced and peak MLR clearly increased as a function of oxygen concentration.
3. Back surface temperature measurements indicated that oxidative pyrolysis provides no appreciable heating or cooling to the sample.
4. For low heat flux (15 kW m^{-2}), the pyrolysis model developed in nitrogen performed the best for a range of oxygen concentrations whereas for higher heat flux (25 kW m^{-2}), the nitrogen model is less viable and an oxidative pyrolysis model provides much better predictions.
5. An analysis was performed to estimate a possible reduction in volumetric oxygen concentration at the sample surface due to mass transport.

6. If mass transport is considered, the surface model gives the best predictions for the 25 kW m^{-2} tests but the nitrogen model still gives the best predictions for the 15 kW m^{-2} tests. Predictions of the volumetric model are largely unchanged by the volumetric model when mass transport is considered.
7. Future work is needed to evaluate the utility of the oxidative pyrolysis kinetics for predictions of ignition times in fire tests.

7.4 Contributions to the field

The key contribution of this work is greater fundamental understanding of the factors which are key to modeling bench scale fire tests, namely the heat feedback and for some materials, oxidative pyrolysis. First, the structure of the flame has a greater impact than the type of material on the flame heat feedback in these bench scale fire tests. In the cone calorimeter study, the overall structure of the flame was similar for a wide range of materials and their flame heat feedback was similar. However, differences in the flame structure across the sample surface (the flame is closer to the sample surface and thinner near the sides) resulted in differences in heat flux by a factor of 2–3.8 when comparing heat fluxes near the side versus the center. Similarly in the UL-94V study, the addition of insulation to the sides changed the structure of the flame which resulted in significant changes to flame heat feedback. When the edges are insulated, flame standoff distance increases, reducing flame heat flux by about 21% (relative to a cold surface). This increase in flame standoff distance is speculated to be

caused by reduced entrainment when the sides are no longer burning (which otherwise would entrain air to draw in the flame). Insulating the sides also affects the flame heat feedback since it removes (or at least reduces) the multidimensional heating at the edges. When the edges are free, convective heat transfer from the flame on the front and sides results in rapid rise in temperature of the material at the edges, resulting in ignition and flame spread propagating there. Observations of the flame on non-insulated and insulated samples confirmed this for a wide range of materials. Additionally, although flame heat feedback was not measured for multiple materials, a sensitivity analysis (in section A3.4) using material-specific flame temperatures showed that flame heat feedback was affected less by material type than it was by changes in the structure of the flame (insulated vs non-insulated sample).

Second, the impact of oxygen on the pyrolysis of material is dependent primarily on the material as well as heating rate and oxygen concentration. Certain materials show little to no sensitivity to oxygen whereas other materials, such as PMMA, show high sensitivity. No trends in chemical structure have been identified by this work to indicate a material's sensitivity to oxygen for thermal degradation but TGA tests can readily reveal if a material is sensitive or not. Based on the results using black PMMA, heating rate (incident heat flux) has an impact because oxidative pyrolysis processes have lower activation energy than anaerobic pyrolysis. If the heating rate is

low, temperatures will be lower for a longer period, allowing the lower activation energy processes of oxidative pyrolysis to dominate. However, higher heating rate results in higher temperatures sooner for which anaerobic pyrolysis competes with oxidative pyrolysis. This behavior was seen for the cone calorimeter predictions for multiple materials: predicted ignition times showed a larger error for low irradiation than for high irradiation when using an anaerobic pyrolysis model. The experimental MLR data of CAPA II tests also showed for black PMMA, oxygen has a greater impact on pyrolysis for lower irradiation. Finally, oxygen concentration impacts oxidative pyrolysis by affecting the kinetics of the processes. Higher oxygen concentrations increase the frequency of collision between O_2 and polymer molecules. Oxygen also allows for additional decomposition mechanisms which have lower activation energy when compared to anaerobic pyrolysis. Given the importance of the oxygen concentration, when selecting a model for oxidative pyrolysis mass transport of oxygen to the sample should be considered. Oxygen will have to diffuse through the evolved pyrolyzate gases to reach the sample and this diffusion is especially important when the concentration of oxygen is low and for higher heating rate which results in a greater mass production rate of pyrolyzate gases.

7.5 Overall summary

Overall, this work found that with careful characterization of the boundary conditions, ThermaKin2Ds can accurately simulate bench scale fire tests when supplied a comprehensive pyrolysis model, making it a valuable predictive tool. Its utility was demonstrated later by providing a blind prediction of cone calorimetry of OSB. However, the quality of predictions is strongly dependent on the quality of the pyrolysis model since any errors in the pyrolysis model will propagate. This work also found that oxygen can significantly impact predictions of ignition time in fire tests, a hurdle to accurate simulation. Correcting ignition time predictions, either by ignition theory or by considering oxidative kinetics, shows promise but is still limited. There remains significant work to better understand the mechanisms of oxidative pyrolysis and for a larger range of materials. However, if an oxidative model can address the issue of predicting ignition times, ThermaKin2Ds will be a powerful and practical tool for modeling fire tests.

Appendices

A1 Pyrolysis Model Parameters

Tables containing the pyrolysis model parameters are provided for all simulated materials in the following sections. Oxidation submodel parameters for HIPS and PMMA determined for UL-94V tests are also given.

A1.1 ABS pyrolysis model

Table A1. ABS reaction scheme [59]

#	Reaction
1	ABS → 0.023 ABS_Res + 0.977 ABS_Gas

Table A2. ABS reaction kinetics and heats of reaction. Endothermic is marked as positive [59].

#	A [s^{-1} or $m^3\ kg^{-1}\ s^{-1}$]	E [J mol^{-1}]	H [J kg^{-1}]
1	1×10^{14}	2.19×10^5	4.6×10^5

Table A3. ABS component properties [59]

Component	ρ [kg m^{-3}]	ε	κ [m^2 kg^{-1}]	k [W m^{-1} K^{-1}]	c [J kg^{-1} K^{-1}]
ABS	1050	0.95	1.71	0.3 - 2.8 $\times 10^{-4}$ T	1580 + 1.3 T
ABS_Res	80	0.95	1.71	0.13 – 5.4 $\times 10^{-4}$ T + 4.8 $\times 10^{-9}$ T^3	820 + 0.112 T

Table A4. ABS gaseous heats of combustion [59].

Component	MCC Δh_c [kJ g^{-1}]
ABS_Gas	36.5

A1.2 Black PMMA (cast) pyrolysis model

Note: Oxidative pyrolysis parameters are not presented here but are presented in Chapter 6 since they require further context. These parameters are strictly for anaerobic pyrolysis.

Table A5. Black PMMA reaction scheme [108]

#	Reaction
1	BlackPMMA → BlackPMMA Glass
2	BlackPMMA Glass → 0.98 BlackPMMA Int + 0.02 BlackPMMA Gas
3	BlackPMMA_Int → 0.002 BlackPMMA Res + 0.998 BlackPMMA_Gas

Table A6. Black PMMA reaction kinetics and heats of reaction. Endothermic heats of reaction are marked as positive [108]

#	A [s^{-1} or m^3 kg^{-1} s^{-1}]	E [J mol^{-1}]	H [J kg^{-1}]
1	1	0	0
2	4.95×10^{16}	1.64×10^5	5×10^3
3	1.35×10^{11}	1.64×10^5	8.17×10^5

Table A7. Black PMMA component properties [108]

Component	ρ [kg m^{-3}]	ε	κ [m^2 kg^{-1}]	k [W m^{-1} K^{-1}]	c [J kg^{-1} K^{-1}]
Black PMMA	1210	0.96	2.38	0.16	-1390 + 8.33 T
Black PMMA Glass	1210	0.96	2.38	0.34 – 4.2 $\times 10^{-4}$ T	851 + 3.07 T
Black PMMA Int	1210	0.96	2.38	0.34 – 4.2 $\times 10^{-4}$ T	851 + 3.07 T
Black PMMA_Res	1210	0.96	2.38	0.34 – 4.2 $\times 10^{-4}$ T	851 + 3.07 T

Table A8. Black PMMA gaseous heats of combustion [108]

Component	MCC Δh_c [kJ g^{-1}]
BlackPMMA_Gas	24.05

A1.3 HIPS pyrolysis model (including oxidation for UL-94V)

Table A9. HIPS reaction scheme [64]

#	Reaction
1	HIPS → 0.043 HIPS_Res + 0.957 HIPS_Gas
2	HIPS_Ox → 0.043 HIPS_Res + 0.957 HIPS_Gas
3	HIPS_Ox → HIPS_Gas

Table A10. HIPS reaction kinetics and heats of reaction. Endothermic is marked as positive [64]

#	A [s^{-1} or $m^3\ kg^{-1}\ s^{-1}$]	E [J mol^{-1}]	H [J kg^{-1}]
1 & 2	1.71×10^{20}	3.01×10^{6}	6.89×10^{6}
3	8.29×10^{4}	1.10 × 105	0

Table A11. HIPS component properties [64]

Component	ρ [kg m^{-3}]	ε	κ [m^2 kg^{-1}]	k [W m^{-1} K^{-1}]	c [J kg^{-1} K^{-1}]
HIPS & HIPS_Ox	1060	0.95	2.12	$0.1 + 1\times10^{-4}$ T	592 + 3.42 T
HIPS_Res	1060	0.95	100	$0.1 + 1\times10^{-4}$ T	592 + 3.42 T

Table A12. HIPS gaseous heats of combustion [64]

Component	Cone (this work) Δh_c [kJ kg^{-1}]	MCC [65] Δh_c [kJ g^{-1}]
HIPS_Gas	30.1	39.2

A1.4 PBT/GF (DEPAL) pyrolysis model

Table A13. PBT/GF with and without DEPAL reaction scheme [67]

*GF was assumed to have the same reactions as PBT but without mass loss or heat flow. The GF reactions strictly change the thermal transport properties of the GF.

Material	#	Reaction
PBT	1	PBT → PBT_Melt
	2	PBT_Melt → 0.84 PBT_Res1 + 0.16 PBT_Gas1
	3	PBT_Res1 → 0.12 PBT_Res2 + 0.88 PBT_Gas2
PBT and DEPAL	4	DEPAL → 0.07 DEPAL_Res1 + 0.93 DEPAL_Gas1
	5	PBT_Melt + 3.6 DEPAL → 2.0 PBT_DEPAL_Res1 + 2.6 PBT_DEPAL_Gas1
GF	1*	GF → GF_Melt
	2*	GF_Melt → GF_Res1
	3*	GF_Res1 → GF_Res2

Table A14. PBT matrix reaction kinetics and heats of reaction. Endothermic is marked as positive [67].

#	A [s^{-1} or $m^3\ kg^{-1}\ s^{-1}$]	E [J mol^{-1}]	H [J kg^{-1}]
1	2.0×10^{40}	4.00×10^5	6.0×10^4
2	2.0×10^{25}	3.41×10^5	1.4×10^5
3	2.4×10^{20}	2.90×10^5	3.1×10^5
4	1.0×10^{12}	2.09×10^5	0
5	2.0×10^{20}	3.19×10^5	2.4×10^6
1*	2.0×10^{40}	4.00×10^5	0
2*	2.0×10^{25}	3.14×10^5	0
3*	2.35×10^{20}	2.66×10^5	0

Table A15. PBT matrix component properties [67]

Component	ρ [kg m^{-3}]	ε	κ [m^2 kg^{-1}]	k [W m^{-1} K^{-1}]	c [J kg^{-1} K^{-1}]
PBT	1333	0.88	2.8	0.12	-524 + 5.60 T
PBT_Melt	1333	0.88	2.8	0.23	2100 + 0.20 T
PBT_Res1	1120	0.88	51.4	0.1 + 1.2 × 10^{-4} T	1900 + 0.10 T
PBT_Res2	1333	0.94	100	0.18	1700
GF	2518	0.81	6.4	0.70	442 + 1.24 T
GF_Melt	2518	0.81	6.4	0.003	442 + 1.24 T
GF_Res1	2518	0.88	53.2	0.006	442 + 1.24 T
GF_Res2	413	0.94	100	0.15	442 + 1.24 T
DEPAL	1570	0.88	2.8	0.40	-2750 + 11.8 T
DEPAL_Res1	2566	0.94	100	1 × 10^{-10} T^3	1700
PBT_DEPAL_Res1	1511	0.94	100	1 × 10^{-9} T^3	1700

Table A16. PBT matrix gaseous heats of combustion [67]

Component	MCC Δh_c [kJ g^{-1}]
PBT_Gas1	21
PBT_Gas2	25
DEPAL_Gas1	7
PBT_DEPAL_Gas1	28

A1.5 PEEK pyrolysis model

Table A17. PEEK reaction scheme [62]

#	Reaction
1	PEEK → PEEK_Melt
2	PEEK_Melt → 0.6 PEEK_Res1 + 0.4 PEEK_Gas1
3	PEEK_Res1 → 0.84 PEEK_Res2 + 0.16 PEEK_Gas2

Table A18. PEEK reaction kinetics and heats of reaction. Endothermic is marked as positive [62]

#	A [s^{-1} or $m^3\ kg^{-1}\ s^{-1}$]	E [J mol^{-1}]	H [J kg^{-1}]
1	3.5×10^{33}	4.15×10^5	3.9×10^4
2	4.3×10^{28}	5.05×10^5	2.68×10^5
3	1.4	5.2×10^4	1.01×10^5

Table A19. PEEK component properties [62]

Component	ρ [kg m^{-3}]	ε	κ [m^2 kg^{-1}]	k [W m^{-1} K^{-1}]	c [J kg^{-1} K^{-1}]
PEEK	1297	0.90	1.6	0.20	-350 + 4 T
PEEK_Melt	1297	0.90	50.8	0.14	1235 + 1.7 T
PEEK_Res1	778	0.94	100	$0.26 + 1.4\times 10^{-10}\ T^3$	632.5 + 2.35 T
PEEK_Res2	654	0.94	100	$0.26 + 1.4\times 10^{-10}\ T^3$	30 + 3 T

Table A20. PEEK gaseous heats of combustion [62]

Component	MCC Δh_c [kJ g^{-1}]
PEEK_Gas1	24.5
PEEK_Gas2	2

A1.6 PEI pyrolysis model

Table A21. PEI reaction scheme [59]

#	Reaction
1	PEI → PEI_Melt
2	PEI_Melt → 0.65 PEI_Res1 + 0.35 PEI_Gas1
3	PEI_Res1 → 0.77 PEI_Res2 + 0.23 PEI_Gas1

Table A22. PEI reaction kinetics and heats of reaction. Endothermic is marked as positive [59]

#	A [s^{-1} or m^3 kg^{-1} s^{-1}]	E [J mol^{-1}]	H [J kg^{-1}]
1	1	0	1×10^3
2	7.66×10^{27}	4.65×10^5	8×10^4
3	6.5×10^2	8.80×10^4	5×10^3

Table A23. PEI component properties [59]

Component	ρ [kg m^{-3}]	ε	κ [m^2 kg^{-1}]	k [W m^{-1} K^{-1}]	c [J kg^{-1} K^{-1}]
PEI	1285	0.95	1.36	$0.4 - 4 \times 10^{-4}$ T	-35.7 + 4.1 T
PEI_Melt	1285	0.95	100	0.32 -3.3×10^{-4} T	1880 + 0.575 T
PEI_Res1	80	0.95	100	$0.45 + 1.9\times 10^{-4}$ T	1590 + 0.308 T
PEI_Res2	80	0.86	100	$0.5 - 3.4 \times 10^{-5}$ T + 2×10^{-10} T^3	592 + 3.42 T

Table A24. PEI gaseous heats of combustion [65]

Component	MCC Δh_c [kJ g^{-1}]
PEI_Gas1	21.3

A1.7 PMMA (extruded, clear) pyrolysis model (including oxidation for UL-94V)

Table A25. PMMA reaction scheme [64]

#	Reaction
1	PMMA → PMMA_Glass
2	PMMA_Ox → PMMA_Ox_Glass
3	PMMA_Glass → 0.015 PMMA_Res1 + 0.985 PMMA_Gas1
4	PMMA _Ox_Glass → 0.015 PMMA_Res1 + 0.985 PMMA_Gas1
5	PMMA_Ox_Glass → PMMA_Gas1

Table A26. PMMA reaction kinetics and heats of reaction. Endothermic is marked as positive [64]

#	A [s^{-1} or m^3 kg^{-1} s^{-1}]	E [J mol^{-1}]	H [J kg^{-1}]
1 & 2	1	0	0
3 & 4	8.6×10^{12}	1.88×10^5	8.46×10^5
5	5.6×10^{10}	1.62×10^5	0

Table A27. PMMA component properties [64]

Component	ρ [kg m^{-3}]	ε	κ [m^2 kg^{-1}]	k [W m^{-1} K^{-1}]	c [J kg^{-1} K^{-1}]
PMMA & PMMA_Ox	1155	0.95	1.94	0.45 -3.8 × 10^{-4} T	601 + 3.63 T
PMMA_Glass & PMMA_Ox_Glass	1155	0.95	1.94	0.27 - 2.4 × 10^{-4} T	601 + 3.63 T
PMMA_Res1	1155	0.95	1.94	0.27 - 2.4 × 10^{-4} T	601 + 3.63 T

Table A28. PMMA gaseous heats of combustion

Component	Cone Δh_c [kJ g^{-1}] [116]	MCC (used for UL-94V) Δh_c [kJ g^{-1}] [65]
PMMA_Gas1	25.5	24.5

A1.8 POM pyrolysis model

Table A29. POM reaction scheme [64]

#	Reaction
1	POM → POM_Melt
2	POM_Melt → 0.4 POM_Res1 + 0.6 POM_Gas1
3	POM_Res1 → 0.018 POM_Res2 + 0.982 POM_Gas1

Table A30. POM reaction kinetics and heats of reaction. Endothermic is marked as positive [64]

#	A [s^{-1} or $m^3\ kg^{-1}\ s^{-1}$]	E [J mol^{-1}]	H [J kg^{-1}]
1	2.69×10^{42}	3.82×10^{5}	1.92×10^{5}
2	3.84×10^{14}	2.00×10^{5}	1.19×10^{6}
3	4.76×10^{44}	5.90×10^{5}	1.35×10^{6}

Table A31. POM component properties [64]

Component	ρ [kg m^{-3}]	ε	κ [m^2 kg^{-1}]	k [W m^{-1} K^{-1}]	c [J kg^{-1} K^{-1}]
POM	1424	0.95	2.14	$0.25 + 1.6 \times 10^{-5}$ T	-1861 + 9.98 T
POM_Melt	1424	0.95	2.14	$0.21 + 8 \times 10^{-6}$ T	1649 + 1.15 T
POM_Res1	1424	0.95	2.14	$0.19 - 6 \times 10^{-5}$ T	1649 + 1.15 T
POM_Res2	1424	0.95	2.14	$0.19 - 6\times 10^{-5}$ T	1649 + 1.15 T

Table A32. POM gaseous heats of combustion

Component	Cone Δh_c [kJ g^{-1}] [116]
POM_Gas1	15.3

A1.9 PVC pyrolysis model

Table A33. PVC reaction model [63]

#	Reaction
1	PVC → PVC_Glass
2	PVC_Glass → 0.96 PVC_Res1 + 0.04 PVC_Gas1
3	PVC_Res1 → 0.78 PVC_Res2 + 0.22 PVC_Gas2
4	PVC_Res2 → 0.57 PVC_Res3 + 0.43 PVC_Gas3
5	PVC_Res3 → 0.90 PVC_Res4 + 0.10 PVC_Gas4
6	PVC_Res4 → 0.49 PVC_Res5 + 0.51 PVC_Gas5

Table A34. PVC reaction kinetics and heats of reaction. Endothermic is marked as positive [63].

#	A [s^{-1} or m^3 kg^{-1} s^{-1}]	E [J mol^{-1}]	H [J kg^{-1}]
1	6.0×10^{40}	2.85×10^5	0
2	1.4×10^{31}	3.36×10^5	3.0×10^3
3	1.4×10^{45}	5.11×10^5	6.2×10^4
4	1.4×10^9	1.28×10^5	1.28×10^5
5	3.0×10^{10}	1.70×10^5	-1.48×10^4
6	3.0×10^{10}	1.80×10^5	6.7×10^4

Table A35. PVC component properties [63]

Component	ρ [kg m^{-3}]	ε	κ [m^2 kg^{-1}]	k [W m^{-1} K^{-1}]	c [J kg^{-1} K^{-1}]
PVC	1409	0.90	2.6	$0.13 + 9 \times 10^{-5}$ T	-2259 + 10 T
PVC_Glass	1409	0.90	2.6	$0.069 + 9.5 \times 10^{-5}$ T	-37 + 4 T
PVC_Res1	1353	0.90	2.6	$0.069 + 9.5 \times 10^{-5}$ T	-37 + 4 T
PVC_Res2	1055	0.92	51.3	$0.072 + 1.5 \times 10^{-4}$ T	-456 + 3.85 T
PVC_Res3	602	0.92	51.3	$0.072 + 1.5 \times 10^{-4}$ T	-456 + 3.85 T
PVC_Res4	1060	0.94	100	$0.028 + 7.7 \times 10^{-5}$ T $+ 6.9 \times 10^{-10}$ T^3	-875 + 3.7 T
PVC_Res5	265	0.94	100	$0.028 + 7.7 \times 10^{-5}$ T $+ 6.9 \times 10^{-10}$ T^3	-875 + 3.7 T

Table A36. PVC gaseous heats of combustion [63]

Component	Δh_c [kJ g^{-1}]
PVC_Gas1	12
PVC_Gas2	1.3
PVC_Gas3	2.8
PVC_Gas4	18
PVC_Gas5	36.5

A1.10 OSB pyrolysis model

Table A37. OSB reaction model [68]

#	Reaction
1	Water → Water_vapor
2	OSB → 0.72 OSB_Res1 + 0.28 OSB_Gas1
3	OSB_Res1 → 0.45 OSB_Res2 + 0.55 OSB_Gas2
4	OSB_Res2 → 0.77 OSB_Res3 + 0.23 OSB_Gas3
5	OSB_Res3 → 0.77 OSB_Res4 + 0.23 OSB_Gas4

Table A38. OSB reaction kinetics and heats of reaction. Endothermic is marked as positive [68]

#	A [s^{-1} or m^3 kg^{-1} s^{-1}]	E [J mol^{-1}]	H [J kg^{-1}]
1	1.55×10^4	4.35×10^4	2.78×10^6
2	1.56×10^7	1.04×10^5	6.82×10^3
3	2.65×10^{12}	1.74×10^5	1.37×10^5
4	8.93×10^3	8.37×10^4	-2.90×10^5
5	4.40×10^{-1}	3.86×10^4	-2.32×10^5

Table A39. OSB component properties [69]

Component	ρ [kg m^{-3}]	ε	κ [m^2 kg^{-1}]	k [W m^{-1} K^{-1}]	c [J kg^{-1} K^{-1}]
Water	n/a	0.81	1000	0.13	5200 - 6.7 T + 0.011 T^2
OSB	652	0.81	1000	0.13	-159 + 4.53 T
OSB_Res1	468	0.78	1000	0.06	197 + 3.40 T
OSB_Res2	184	0.76	1000	0.42	553 + 2.27 T
OSB_Res3	142	0.73	1000	0.39	909+ 1.13 T
OSB_Res4	108	0.70	1000	0.53	1270

Table A40. OSB gaseous heats of combustion [68]

Component	Δh_c [kJ g^{-1}]
Water_vapor	0
OSB_Gas1	12.5
OSB_Gas2	15.2
OSB_Gas3	11.5
OSB_Gas4	7.5

A2 Cone calorimetry: additional analysis

A2.1 Instantaneous heats of combustion

Mass loss rate (MLR) data was calculated from the mass measurements using a second order central difference scheme. For HIPS, PMMA, and POM, the MLR data were found to coincide very well with the heat release rate (HRR) data, as shown in Fig. A1. The instantaneous heats of combustion were then calculated for each of these materials by dividing the average HRR by the average MLR, the results of which are also shown in Fig. A1. The instantaneous heats of combustion were found to be relatively constant after ignition for HIPS, PMM, and POM. For the other materials studied in cone calorimeter tests, PBT/GF and PBT/GF/DEPAL, these materials were expected to have a non-constant heat of combustion since they produce multiple species of varying heats of combustion. Instantaneous heats of combustion were calculated for these materials in the same manner and as shown in Fig. A2, were found not to be constant.

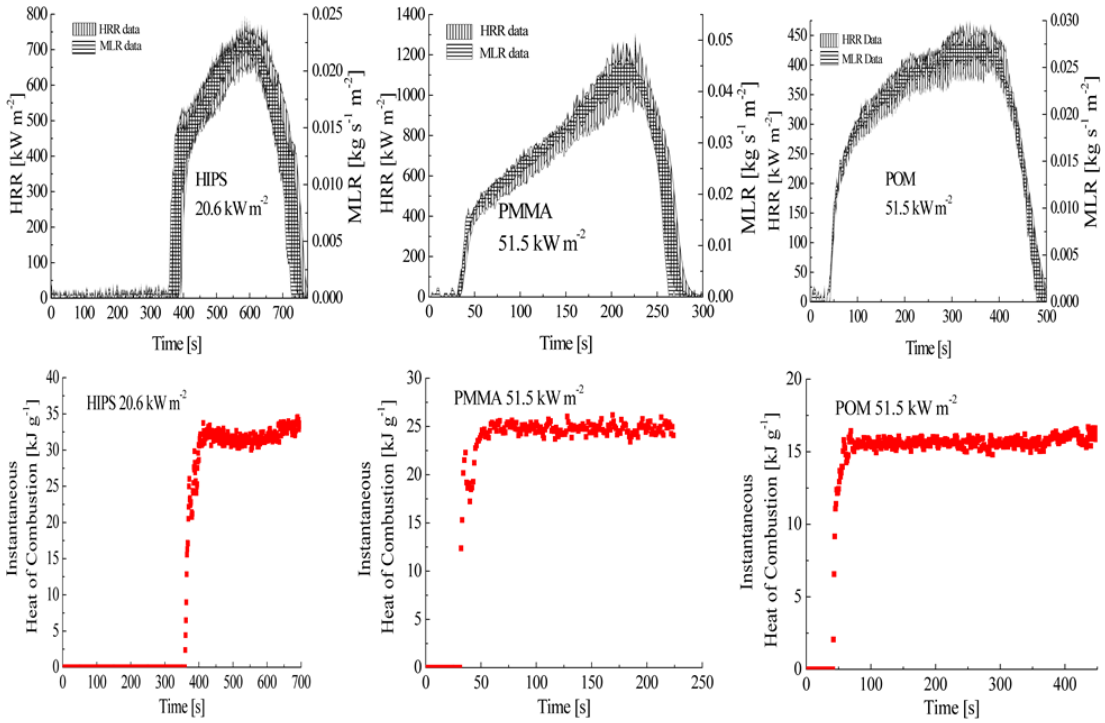

Fig. A1. Experimental HRR and MLR measurement results for HIPS, PMMA, and POM showing a high degree of overlap (top plot). Calculated instantaneous heats of combustion showing constant behavior (bottom plot)

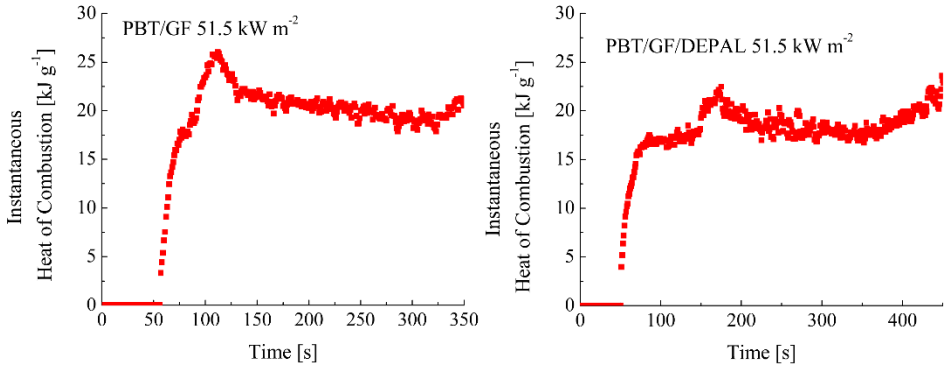

Fig. A2. Calculated instantaneous heats of combustion illustrating how it is not constant for PBT/GF and PBT/GF/DEPAL, as expected given that they produce multiple species with varying heats of combustion as measured in MCC [89].

A3 UL-94V: additional analysis

A3.1 Selection of intensity threshold for image segmentation

The intensity threshold used to define the presence of the PMMA flame was determined by examining segmented images for several intensity thresholds and comparing them with the original video. The intensity threshold was chosen to be as high as possible (to be more conservative) while still identifying ignition properly. As shown in Fig. A3, an intensity of 36/255 fails to identify ignition but an intensity of 34/255 or lower does identify ignition properly. Fig. A4 shows how the lower intensities (30/255 and 32/255) begin to overestimate the vertical length of the flame at later stages. Thus, an intensity of 34/255 was the threshold selected for the image analysis. Additionally, to assess the impact of the intensity threshold on the uncertainty of the measured flame lengths, a sensitivity analysis was performed by comparing the flame lengths determined using a significantly lower intensity (20/255) and a significantly higher intensity (48/255). This range was selected because intensities outside of this range appeared to either grossly overestimate the size of the flame at later stages or fail to detect early flame development. Differences between the IR flame length computed using I=34/255 and the lower and higher intensities were 6%, on

average. A 6% uncertainty was subsequently included in the uncertainty of the IR flame length measurements (in pixels).

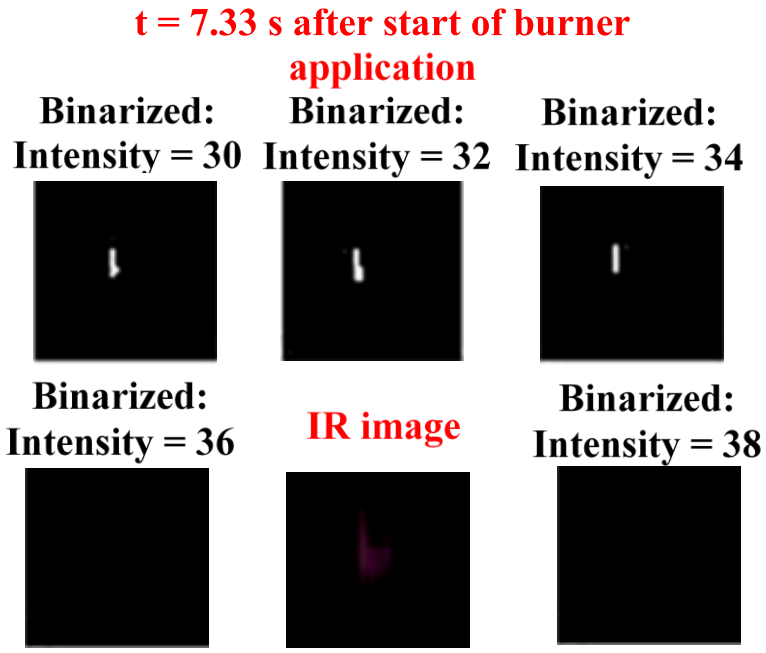

Fig. A3. Comparison of the IR image and binarized images for different intensity thresholds for PMMA flame at ignition. The PMMA flame is barely visible.

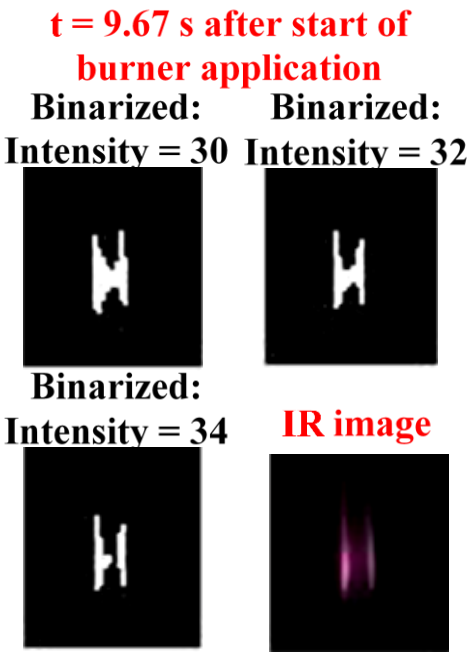

Fig. A4. Comparison of the IR image and binarized images for different intensity thresholds for PMMA flame after ignition.

A3.2 Radiation correction for thermocouple readings

At high temperatures, radiation loss by the thermocouple bead is significant and the bead temperature can no longer be assumed to be equal to the temperature of the measured gas-phase flame. Thus, this work corrected the thermocouple measurements using the method outlined by Shaddix [117]. Beginning with a heat transfer balance about the thermocouple bead yields Equation (A1) where h is the convective coefficient for the gas flow about the thermocouple bead [W m^{-2} K^{-1}] , T_{bead} is the temperature of the thermocouple bead [K], T_{gas} is the flame temperature [K], and T_{∞} is the

surroundings (ambient) temperature [K]. σ is the Stefan-Boltzmann constant (5.67×10^{-8} W m^{-2} K^{-4}) and ε is the bead emissivity.

$$h\left(T_{gas} - T_{bead}\right) = \varepsilon\sigma(T_{bead}^4 - T_\infty^4) \quad \text{(A1)}$$

Rewriting the convective coefficient in terms of Nusselt number and re-arranging for the desired T_{gas}, results in Equation (A2).

$$T_{gas} = \varepsilon\sigma\frac{d}{k\,Nu}(T_{bead}^4 - T_\infty^4) + T_{bead} \quad \text{(A2)}$$

Based upon the recommendations presented by Shaddix [117], this work used the Collis-Williams correlation for convective flow about a cylinder [118] to determine Nu, which is given in Equation (A3). The terms of Equation (A3) are the following: $Re = Ud/\nu$, where U is the flow velocity [m s^{-1}], d is the diameter of the thermocouple wire [m], ν is the kinematic velocity [m^2 s^{-1}], and T_m is a mean temperature [K] of T_{gas} and T_∞.

$$Nu = (0.24 + 0.56Re^{0.45})(T_m/T_\infty)^{0.17} \quad \text{valid for } 0.02 < \text{Re} < 44 \quad \text{(A3)}$$

Gas properties were assumed to be that of air and were found by interpolation of tabulated values [85] using the assumed T_{gas}. From kinematics, U was estimated as $U = \sqrt{2ay}$ where y is the distance from the top of the burner to the measurement point [m] and a is the acceleration due to buoyancy [m s^{-2}]. a was estimated using an expression for acceleration due to buoyancy of a slot burner given as: $a =$

$0.6\ g\ (T_{gas}/T_{\infty} - 1)$ [119]. Emissivity was based on an expression for the emissivity of pure platinum [120] given by: $\varepsilon = 1.507 \times 10^{-4}\ T[K] - 1.596 \times 10^{-8}\ T[K]^2$. This expression was chosen since it has a wide temperature range of validity and it has been used previously to correct R-type thermocouple measurements [100]. Since k and Nu are functions of T_{gas}, T_{gas} must be determined by iteration. The approach is to guess T_{gas}, interpolate for the gas properties, calculate Re, calculate Nu, and then calculate T_{gas} using Equation (A2) and compare the calculated value with the initial guess. If the values are within 0.001 K, stop. Otherwise, use the calculated T_{gas} as the next initial guess and repeat the process. T_{bead} is a good initial guess for T_{gas}. ε is strictly a function of T_{bead} so it does not have to be found by iteration. Error in corrected gas temperature was found by error propagation and was estimated to be 2% overall, comparable to previously reported values for high temperature flames [99,100]. Catalytic effects and conduction losses were assumed negligible.

A3.3 Uncertainty analysis for IR flame length measurement

The experimental IR flame length, $y_{eff,tip}$, can be understood as $y_{eff,tip} = C \times P_{avg}$where C is the conversion for the tests [cm pixel^{-1}] and P_{avg} is the average IR flame length [pixels] determined from the images of repeated tests. For reference, the resolution of the average conversion was C = 2.06 × 10^{-2} ± 3 × 10^{-4} cm pixel^{-1}. Based

on propagation of uncertainty, the uncertainty in the experimental IR flame length is given by: $u_{y_{eff,tip}} = \sqrt{\left(\frac{dy_{eff,tip}}{dC}u_C\right)^2 + \left(\frac{dy_{eff,tip}}{dP}u_P\right)^2}$ which simplifies to $\sqrt{\left(P_{avg}u_C\right)^2 + (Cu_P)^2}$ where u_c and u_p are the uncertainties of the conversion and the pixel length, respectively. u_c was estimated as two standard deviations of the mean of multiple conversions (3×10^{-4} cm pixel^{-1}). u_p was estimated as two standard deviations of the pixel length of the three tests plus an additional 6% due to the uncertainty of the intensity threshold. u_p was calculated separately for each set of sample geometry (insulated and non-insulated). The combined uncertainty was about 18%, on average, for experiments with the insulated sample and 8%, on average, for the non-insulated samples.

A3.4 Sensitivity study of assumed flame temperature on UL-94V simulation results

To determine the impact of flame temperature on UL-94V model performance, simulations of HIPS were redone using its adiabatic flame temperature of 2460 K. HIPS was selected because its adiabatic flame temperature had the largest deviation from that of PMMA while also igniting in the simulation; PEI has a greater deviation in flame temperature (1985 K) but does not ignite in the simulation, making it unsuitable. Overall, changing the adiabatic flame temperature did not significantly change results;

there is a high degree of overlap between the simulation using the adiabatic temperature of PMMA and the one using the adiabatic temperature of HIPS, as shown by Fig. A5. Thus, assuming a generalized flame temperature of 2330 K is reasonable.

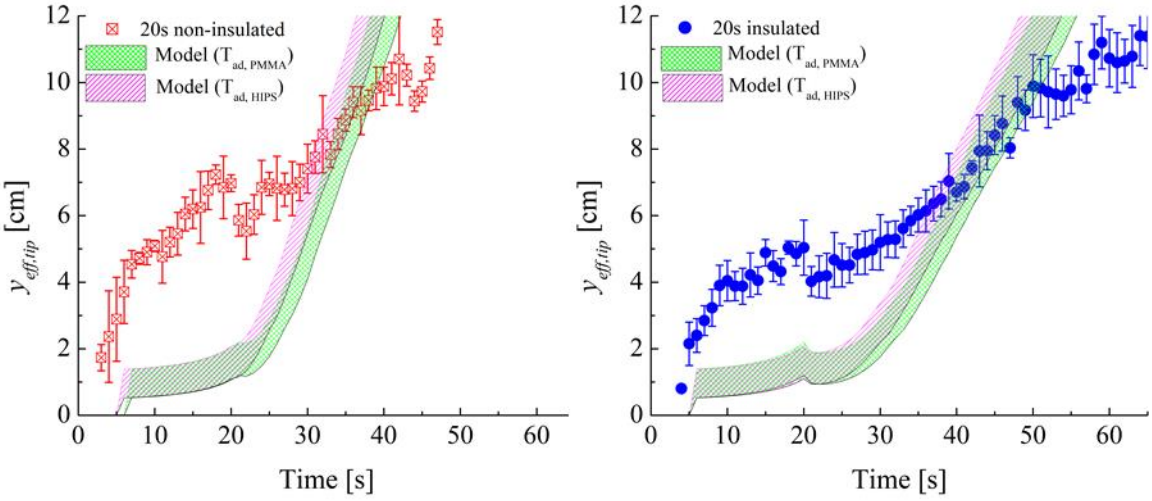

Fig A5. Comparison of simulated flame spread dynamics, using the default PMMA flame temperature and a material-specific adiabatic flame temperature, and experimental results. The shaded area of the model accounts for the uncertainty in y_{tip}^{*} used to relate the simulated y_f to $y_{eff,tip}$.

A4 Oxidative study: additional analysis

A4.1 Brief description of automated fitting algorithm and iteration procedure for determination of oxidative kinetics from TGA data.

Analysis of the powder TGA tests to determine volumetric kinetics used the algorithm developed by Fiola [108,109]. The algorithm relies on the approximate solution for constant heating, single-step first-order thermal decomposition at peak

mass loss rate, derived by Lyon et al. [121]. The solution is re-arranged to estimate activation energy E [J mol^{-1}] and A[s^{-1}] which are given in Equations A4 and A5 where e is the natural number, T_{peak} [K] and MLR_{peak} [mg s^{-1}] are the temperature of peak mass loss rate and the magnitude of the peak, m_0 [mg] is the initial sample mass, $\frac{dT}{dt}$ is the heating rate [K s^{-1}], and θ is the yield of solid residue.

$$E = \frac{eRT_{peak}^2 MLR_{peak}}{(1-\theta)\frac{dT}{dt}m_0} \quad \text{(A4)}$$

$$A = \frac{eMLR_{peak}}{(1-\theta)m_0}\exp(\frac{E}{RT_{peak}}) \quad \text{(A5)}$$

Rather than iterate E and A directly, which can be cumbersome since they can compensate for one another, E and A are calculated using Equations A4 and A5 while varying the assumed T_{peak} and MLR_{peak}. Effectively, the algorithm uses unique pairs of E and A. After E and A are calculated, the TGA test is simulated using these values. Simulated mass and mass loss rate are then compared with experimental data to evaluate the quality of the prediction. This quality was quantified via a goodness-of-fit criterion, GoF, defined by Equation A6. Essentially it is a weighted combination of the square root of mean square error of MLR and mass predictions normalized by the maximum values. This process is repeated for several variations in T_{peak} and MLR_{peak} (144 per reaction). The E and A which give the best GoF are then saved.

$$GoF = 1 - \left(\frac{0.6}{Exp\ MLR_{max}} \sqrt{\frac{\sum_i^N (Exp\ MLR_i - Model\ MLR_i)^2}{N}} + \right.$$

$$\left. \frac{0.4}{Exp\ m_{max}} \sqrt{\frac{\sum_i^N (Exp\ m_i - Model\ m_i)^2}{N}} \right) \qquad \text{(A6)}$$

For the inverse analysis of the surface reaction kinetics, a different approach is required since Equations A4 and A5 are no longer applicable. Instead, the kinetic parameters were C and D were iterated directly. Fortunately, only one expression had to be parameterized, so a more direct approach is possible without too much computational time. It begins with the user supplying a range of C and D values. The program starts with the first guess for C and D, simulates the TGA test, and then calculates GoF. A similar GoF expression was used except mass flux, MF, was used instead of MLR and the fit of mass data was not considered as shown in Equation A7.

$$GoF_{surface} = 1 - \left(\frac{1}{Exp\ MF_{max}} \sqrt{\frac{\sum_i^N (Exp\ MF_i - Model\ MF_i)^2}{N}} \right) \qquad \text{(A7)}$$

C is fixed and D is then increased, re-simulated until no further improvement in GoF. The program then increases C and once again loops through D. Eventually C and D are determined to the nearest 1000 that give the best GoF.

A4.2 Confirmation of CAPA II IR temperature measurement by copper plate

As shown in Fig A6, the IR camera can accurately capture the back surface temperature data as verified by thermocouple measurements of a painted copper plate.

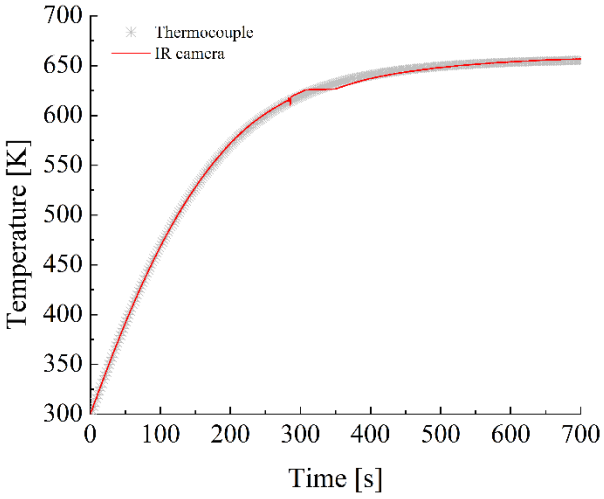

Fig. A6. Validation of back surface temperature measurement using a copper plate with embedded thermocouples.

A4.3 Radiative and convective boundary conditions for CAPA II simulation

The radiative and convective boundary conditions in CAPA II test comprise radiation from the conical heater, radiative and convective exchange between the top of the sample and the walls of the chamber, and radiative and convective exchange between the bottom surface and the surroundings. Radiative and convective exchange are calculated directly by ThermaKin2Ds when the convective coefficient and environmental temperature profile are prescribed. Extensive work was performed by

Swann et al. to characterize these conditions for a wide range of heater settings [61,115]. CFD simulations were used to inversely determine convective coefficients of 7.2 and 4.0 W m^{-2} K^{-1} for the top and bottom surfaces, respectively. Temperature measurements were used to develop an expression for the top and bottom environmental temperatures. For the top environmental temperature, $T_{e,top}$, is given by Equation A8 where T_1, T_2, T_3, and T_4 are empirical constants that are a function of heat flux.

$$T_{e,top} = T_1 \exp(t/T_2) + T_3 \exp(t/T_4) + 290 \qquad \text{(A8)}$$

These empirical constants have been plotted against heat flux as shown in Fig. A7 so that they can be readily calculated for other heating conditions as was done for this work.

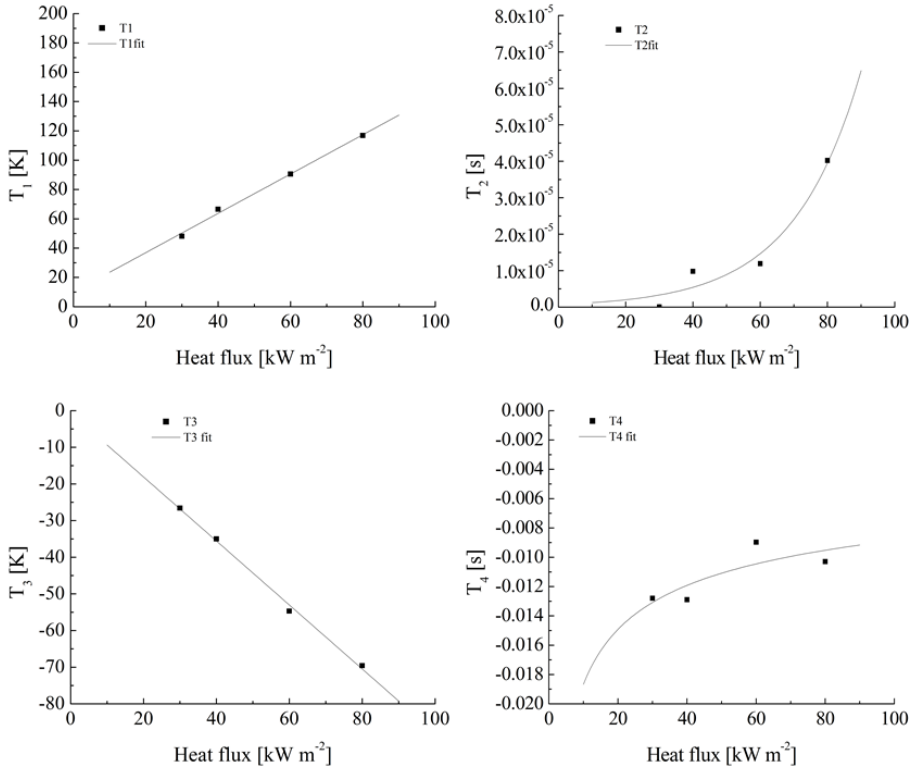

Fig. A7 Comparison of $T_{e,top}$ parameters versus heat flux and the resulting fits.

The bottom environmental temperature, $T_{e,bottom}$, is much simpler. It is a linear piecewise function with a linear increase in temperature that eventually becomes a steady value. Fiola [109] found the steady value to be 308 K once 800 s have elapsed for testing black PMMA under 25 kW m^{-2}. This same expression was used for this work and agreed reasonably with this work's measurements. For the 15 kW m^{-2} test, bottom environmental temperatures were found to reach a steady value of 303 K after 1500 s have elapsed. The data and fit are shown in Fig. A8.

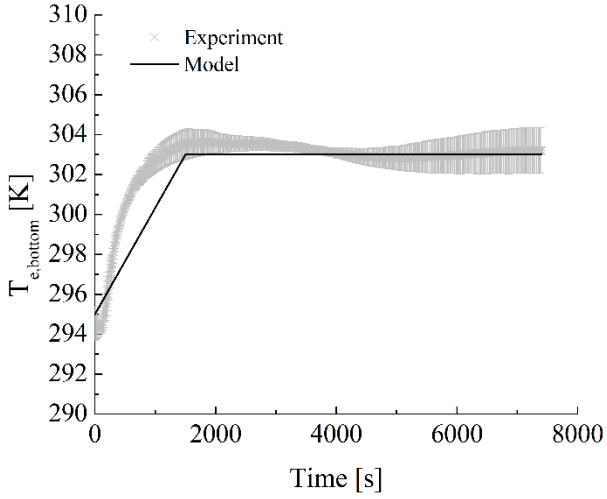

Fig. A8 Fitting of bottom environmental temperature, $T_{e,bottom}$, and model expression.

Bibliography

[1] B. Evarts, Fire loss in the United States during 2018, Quincy, MA, 2019.

[2] V. Babrauskas, Development of the cone calorimeter—A bench-scale heat release rate apparatus based on oxygen consumption, Fire Mater. 8 (1984) 81–95. https://doi.org/10.1002/fam.810080206.

[3] V. Babrauskas, D.R. Peacock, Heat release rate: the single most important parameter in fire hazard, Fire Saf. J. 18 (1992) 255–272.

[4] L.Y. Cooper, A concept for estimating available safe egress time in fires, Fire Saf. J. 5 (1983) 135–144. https://doi.org/10.1016/0379-7112(83)90006-1.

[5] B.T. Rhodes, J.G. Quintiere, Burning rate and flame heat flux for PMMA in a cone calorimeter, Fire Saf. J. 26 (1996) 221–240. https://doi.org/10.1016/S0379-7112(96)00025-2.

[6] J. Luche, T. Rogaume, F. Richard, E. Guillaume, Characterization of thermal properties and analysis of combustion behavior of PMMA in a cone calorimeter, Fire Saf. J. 46 (2011) 451–461. https://doi.org/10.1016/j.firesaf.2011.07.005.

[7] M.I. Nelson, J. Brindley, A. McIntosh, The dependence of critical heat flux on fuel and additive properties: a critical mass flux model, Fire Saf. J. 24 (1995) 107–130. https://doi.org/10.1016/0379-7112(95)00013-J.

[8] F. Kempel, B. Schartel, G.T. Linteris, S.I. Stoliarov, R.E. Lyon, R.N. Walters, A. Hofmann, Prediction of the mass loss rate of polymer materials: Impact of residue formation, Combust. Flame. 159 (2012) 2974–2984. https://doi.org/10.1016/j.combustflame.2012.03.012.

[9] C. Lautenberger, G. Rein, C. Fernandez-Pello, The application of a genetic algorithm to estimate material properties for fire modeling from bench-scale fire test data, Fire Saf. J. 41 (2006) 204–214. https://doi.org/10.1016/j.firesaf.2005.12.004.

[10] ASTM International, ASTM E2058-19 Standard Test Methods for Measurement of Flammability of Materials in Cleanrooms Using a Fire Propagation Apparatus (FPA), Annu. B. ASTM Stand. (2019). https://doi.org/10.1520/E2058-19.2.

[11] ASTM International, ASTM D2863-13: Standard Test Method for Measuring the Minimum Oxygen Concentration to Support Candle-Like Combustion of Plastics (Oxygen Index), Annu. B. ASTM Stand. (2013) 1–14. https://doi.org/10.1520/D2863-12.1.

[12] ASTM International, ASTM D3801-19. Standard Test Method for Measuring the Comparative Burning Characteristics of Solid Plastics in a Vertical Position,

Annu. B. ASTM Stand. (2019) 1-. https://doi.org/10.1520/D3801-10.2.
[13] O. Korobeinichev, M. Gonchikzhapov, A. Tereshchenko, I. Gerasimov, A. Shmakov, A. Paletsky, A. Karpov, An experimental study of horizontal flame spread over PMMA surface in still air, Combust. Flame. 188 (2018) 388–398. https://doi.org/10.1016/J.COMBUSTFLAME.2017.10.008.
[14] T.J. Ohlemiller, Modeling of smoldering combustion propagation, Prog. Energy Combust. Sci. 11 (1985) 277–310. https://doi.org/10.1016/0360-1285(85)90004-8.
[15] S. Hong, J. Yang, S. Ahn, Y. Mun, G. Lee, Flame retardancy performance of various UL94 classified materials exposed to external ignition sources, Fire Mater. 28 (2004) 25–31. https://doi.org/10.1002/fam.840.
[16] R.E. Lyon, M.L. Janssens, Polymer Flammability, 2005. https://doi.org/10.1002/pol.1980.170180319.
[17] E.D. Weil, N.G. Patel, M.M. Said, M.M. Hirschler, S. Shakir, Oxygen index: Correlations to other fire tests, Fire Mater. 16 (1992) 159–167. https://doi.org/10.1002/fam.810160402.
[18] B. Schartel, U. Braun, Comprehensive fire behaviour assessment of polymeric materials based on cone calorimeter investigations, E-Polymers. 3 (2003). https://doi.org/10.1515/epoly.2003.3.1.177.
[19] M. Bundy, T. Ohlemiller, M. Bundy, T. Ohlemiller, Bench-Scale Flammability Measures for Electronic Equipment Bench-Scale Flammability Measures for Electronic Equipment, (2003).
[20] A.B. Morgan, M. Bundy, Cone calorimeter analysis of UL-94 V-rated plastics, Fire Mater. 31 (2007) 257–283. https://doi.org/10.1002/fam.
[21] I. Naeem, J.G. Quintiere, Flame heat fluxes in pmma pool fires, J. Fire Prot. Eng. 6 (1994) 153–162.
[22] D. Hopkins, J.G. Quintiere, Material fire properties and predictions for thermoplastics, Fire Saf. J. 26 (1996) 241–268. https://doi.org/10.1016/S0379-7112(96)00033-1.
[23] S.I. Stoliarov, S. Crowley, R.E. Lyon, G.T. Linteris, Prediction of the burning rates of non-charring polymers, Combust. Flame. 156 (2009) 1068–1083. https://doi.org/10.1016/j.combustflame.2008.11.010.
[24] S.I. Stoliarov, I.T. Leventon, R.E. Lyon, Two-dimensional model of burning for pyrolyzable solids, Fire Mater. 38 (2014) 391–408. https://doi.org/10.1002/fam.
[25] S.I. Stoliarov, R.E. Lyon, Report - Thermo-kinetic model of burning for pyrolyzing materials, DOT/FAA/AR-TN08/17, 2008.
[26] S.I. Stoliarov, S. Crowley, R.N. Walters, R.E. Lyon, Prediction of the burning

rates of charring polymers, Combust. Flame. 157 (2010) 2024–2034. https://doi.org/10.1016/j.combustflame.2010.03.011.
[27] P.A. Beaulieu, N.A. Dembsey, Effect of oxygen on flame heat flux in horizontal and vertical orientations, Fire Saf. J. 43 (2008) 410–428. https://doi.org/10.1016/j.firesaf.2007.11.008.
[28] A.Y. Snegirev, V.A. Talalov, V. V. Stepanov, J.N. Harris, A new model to predict pyrolysis, ignition and burning of flammable materials in fire tests, Fire Saf. J. 59 (2013) 132–150. https://doi.org/10.1016/j.firesaf.2013.03.012.
[29] J.A. Quintiere, R.N. Walters, S. Crowley, Flammability Properties of Aircraft Carbon-Fiber Structural Composite, Tech. Rep. 7 (2007) 8–72.
[30] G. Linteris, L. Gewuerz, K. McGrattan, G. Forney, Modeling solid sample burning, Fire Saf. Sci. (2005) 625–636. https://doi.org/10.3801/IAFSS.FSS.8-625.
[31] R. Mcdermott, Sixth Edition Fire Dynamics Simulator Technical Reference Guide Volume 1 : Mathematical Model 6.3, 1 (2015).
[32] A. Kacem, M. Mense, Y. Pizzo, G. Boyer, S. Suard, P. Boulet, G. Parent, B. Porterie, A fully coupled fluid/solid model for open air combustion of horizontally-oriented PMMA samples, Combust. Flame. 170 (2016) 135–147. https://doi.org/10.1016/j.combustflame.2016.04.009.
[33] S. Suard, C. Lapuerta, F. Babik, L. Rigollet, Verification and validation of a CFD model for simulations of large-scale compartment fires, Nucl. Eng. Des. 241 (2011) 3645–3657. https://doi.org/10.1016/j.nucengdes.2011.08.012.
[34] G. Boyer, Fully coupled CFD simulation of the pyrolysis of non-charring polymers: A predictive approach, Fire Saf. J. 91 (2017) 208–217. https://doi.org/10.1016/j.firesaf.2017.03.070.
[35] A. Galgano, C. Di Blasi, C. Branca, Numerical evaluation of the flame to solid heat flux during poly(methyl methacrylate) combustion, Fire Mater. 42 (2018) 403–412. https://doi.org/10.1002/fam.2505.
[36] C. Di Blasi, A. Galgano, Influences of properties and heating characteristics on the thermal decomposition of polymer/carbon nanotube nanocomposites, Fire Saf. J. 59 (2013) 166–177. https://doi.org/10.1016/j.firesaf.2013.04.006.
[37] E.T. Auth, USING A BURNING RATE EMULATOR (BRE) TO EMULATE CONDENSED FUELS AND STUDY POOL FIRE BEHAVIOR IN 1G, Master's thesis, University of Maryland, College Park, Department of Fire Protection Engineering, 2019.
[38] B.P. Downey, AN INVESTIGATION OF THE UL-94V PLASTICS FLAMMABILITY TEST, Master's thesis, University of Maryland, College

Park, Department of Fire Protection Engineering, 2009.
[39] J.G. Quintiere, B.P. Downey, R.E. Lyon, An Investigation of the Vertical Bunsen Burner Test for Flammability of Plastics, (2012) 12. https://doi.org/10.1002/0471721557.ch11.
[40] Y. Wang, J. Zhang, J. Jow, K. Su, Analysis and modeling of ignitability of polymers in the UL-94 vertical burning test condition, J. Fire Sci. 27 (2009) 561–581. https://doi.org/10.1177/0734904109099999.
[41] Y. Wang, F. Zhang, C. Jiao, Y. Jin, J. Zhang, Convective heat transfer of the bunsen flame in the UL94 vertical burning test for polymers, J. Fire Sci. 28 (2010) 337–356. https://doi.org/10.1177/0734904109351484.
[42] Y. Wang, J. Zhang, Influences of specimen size and heating mode on the ignitability of polymeric materials in typical small-scale fire test conditions, Fire Mater. 36 (2012) 231–240. https://doi.org/10.1002/fam.
[43] Y. Wang, J. Jow, K. Su, J. Zhang, Development of the unsteady upward fire model to simulate polymer burning under UL94 vertical test conditions, Fire Saf. J. 54 (2012) 1–13. https://doi.org/10.1016/j.firesaf.2012.08.001.
[44] ASTM International, ASTM D5207-14. Confirmation of 20–mm (50–W) and 125–mm (500–W) Test Flames for Small-Scale Burning Tests on Plastic Materials, Annu. B. ASTM Stand. (2014). https://doi.org/10.1520/D5207-09.2.
[45] Y. Wang, J. Jow, K. Su, J. Zhang, Dripping behavior of burning polymers under UL94 vertical test conditions, J. Fire Sci. 30 (2012) 477–501. https://doi.org/10.1177/0734904112446125.
[46] Y. Wang, F. Zhang, X. Chen, Y. Jin, J. Zhang, Burning and dripping behaviors of polymers under the UL94 vertical burning test conditions Yong, Fire Mater. 34 (2010) 203–215. https://doi.org/10.1002/fam.
[47] Y. Wang, J. Zhang, Thermal stabilities of drops of burning thermoplastics under the UL 94 vertical test conditions, J. Hazard. Mater. 246–247 (2013) 103–109. https://doi.org/10.1016/j.jhazmat.2012.12.020.
[48] Y. Wang, W. Kang, X. Zhang, C. Chen, P. Sun, F. Zhang, S. Li, Development of a pendant experiment using melt indexer for correlation with the large-size dripping in the UL-94 test, Fire Mater. 42 (2018) 436–446. https://doi.org/10.1002/fam.2510.
[49] F. Kempel, B. Schartel, J.M. Marti, K.M. Butler, R. Rossi, S.R. Idelsohn, E. Onate, A. Hofmann, Modelling the vertical UL 94 test: competition and collaboration between melt dripping, gasification and combustion, Fire Mater. 39 (2015) 570–584. https://doi.org/10.1002/fam.2257.
[50] T. Kashiwagi, T. Hirata, J.E. Brown, Thermal and Oxidative Degradation of

Poly(methyl methacrylate): Molecular Weight, Macromolecules. 18 (1985) 131–138. https://doi.org/10.1021/ma00144a003.
[51] T. Kashiwagi, J.E. Brown, A. Inaba, K. Hatada, T. Kitayama, E. Masuda, Effects of Weak Linkages on the Thermal and Oxidative Degradation of Poly(methyl methacrylates), Macromolecules. 19 (1986) 2160–2168. https://doi.org/10.1021/ma00162a010.
[52] T. Hirata, T. Kashiwagi, J.E. Brown, Thermal and Oxidative Degradation of Poly(methyl methacrylate): Weight Loss, Macromolecules. 18 (1985) 1410–1418. https://doi.org/10.1021/ma00149a010.
[53] T. Kashiwagi, Thermal and Oxidative Degradation of Polymers, 2001. https://doi.org/10.6028/jres.070A.043.
[54] S.M. Dakka, TG/DTA/MS of Poly(Methyl Methacrylate), J. Therm. Anal. Calorim. 74 (2004) 729–734. https://doi.org/10.1023/b:jtan.0000011005.54630.cd.
[55] O. Senneca, R. Chirone, P. Salatino, Oxidative pyrolysis of solid fuels, J. Anal. Appl. Pyrolysis. 71 (2004) 959–970. https://doi.org/10.1016/J.JAAP.2003.12.006.
[56] W.R. Zeng, S.F. Li, W.K. Chow, of Fire Sciences Review on Chemical Reactions of Burning, J. Fire Sci. 20 (2011). https://doi.org/10.1106/073490402031482.
[57] J. D. Peterson, V. Sergey, W.C. A., Kinetics of the Thermal and Thermo-Oxidative Degradation of Polystyrene, Polyethylene and Poly(propylene), Macromol. Chem. Phys. 202 (2001) 775–784.https://doi.org/10.1002/1521-3935(20010301)202:6
[58] V. Kholodovych, W.J. Welsh, Thermal-Oxidative Stability and Degradation of Polymers, Phys. Prop. Polym. Handb. (2007) 927–938. https://doi.org/10.1007/978-0-387-69002-5_54.
[59] J. Li, A MULTISCALE APPROACH TO PARAMETERIZATION OF BURNING MODELS FOR POLYMERIC MATERIALS, Dissertation, University of Maryland, College Park, Department of Mechanical Engineering, 2014.
[60] Y. Ding, A GENERALIZED METHODOLOGY TO DEVELOP PYROLYSIS MODELS FOR POLYMERIC MATERIALS CONTAINING REACTIVE FLAME RETARDANTS: RELATIONSHIP BETWEEN MATERIAL COMPOSITION AND FLAMMABILITY BEHAVIOR, Dissertation, University of Maryland, College Park, Department of Mechanical Engineering, 2018.

[61] J.D. Swann, A COMPREHENSIVE CHARACTERIZATION OF PYROLYSIS AND COMBUSTION OF INTUMESCENT AND CHARRING POLYMERS USING TWO-DIMENSIONAL MODELING: A RELATIONSHIP BETWEEN THERMAL TRANSPORT AND THE PHYSICAL STRUCTURE OF THE INTUMESCENT CHAR, Dissertation, University of Maryland, College Park, Department of Mechanical Engineering, 2019.

[62] J.D. Swann, Y. Ding, S.I. Stoliarov, Comparative analysis of pyrolysis and combustion of bisphenol A polycarbonate and poly(ether ether ketone) using two-dimensional modeling: A relation between thermal transport and the physical structure of the intumescent char, Combust. Flame. 212 (2020) 469–485. https://doi.org/10.1016/j.combustflame.2019.11.017.

[63] J.D. Swann, Y. Ding, S.I. Stoliarov, Characterization of pyrolysis and combustion of rigid poly(vinyl chloride) using two-dimensional modeling, Int. J. Heat Mass Transf. 132 (2019) 347–361. https://doi.org/10.1016/J.IJHEATMASSTRANSFER.2018.12.011.

[64] J. Li, J. Gong, S.I. Stoliarov, Gasification experiments for pyrolysis model parameterization and validation, Int. J. Heat Mass Transf. 77 (2014) 738–744. https://doi.org/10.1016/j.ijheatmasstransfer.2014.06.003.

[65] R.E. Lyon, R.N. Walters, S.I. Stoliarov, N. Safronava, Principles and Practice of Microscale Combustion Calorimetry, 2013.

[66] U. Braun, B. Schartel, Flame retardancy mechanisms of aluminium phosphinate in combination with melamine cyanurate in glass-fibre-reinforced poly(1,4-butylene terephthalate), Macromol. Mater. Eng. 293 (2008) 206–217. https://doi.org/10.1002/mame.200700330.

[67] Y. Ding, S.I. Stoliarov, R.H. Kraemer, Pyrolysis model development for a polymeric material containing multiple flame retardants: Relationship between heat release rate and material composition, Combust. Flame. (2019). https://doi.org/10.1016/j.combustflame.2019.01.003.

[68] J. Gong, H. Zhu, H. Zhou, S.I. Stoliarov, Development of a pyrolysis model for oriented strand board. Part I: Kinetics and thermodynamics of the thermal decomposition, J. Fire Sci. 39 (2021) 190–204. https://doi.org/10.1177/0734904120982887.

[69] J. Gong, H. Zhou, H. Zhu, C.G. McCoy, S.I. Stoliarov, Development of a pyrolysis model for oriented strand board. Part II: thermal transport parameterization and bench-scale validation, J. Fire Sci. Accepted (2021).

[70] ASTM International, ASTM E1354-17 Standard Test Method for Heat and Visible Smoke Release Rates for Materials and Products Using an Oxygen Consumption Calorimeter, Annu. B. ASTM Stand. 44 (2017) 2861–2869. https://doi.org/10.1520/E1354-16A.1.8.
[71] J.L. Tilles, QUANTIFICATION OF FLAME HEAT FEEDBACK IN CONE CALORIMETRY TESTS, Master's thesis, University of Maryland, College Park, Department of Fire Protection Engineering, 2017.
[72] Morgan Advanced Materials, Product Data Book, (2018) 41. https://www.morganthermalceramics.com/media/7699/morgan-advanced-materials_thermal-ceramics-product-data-book-e-version_2.pdf (accessed July 9, 2017).
[73] M.B. McKinnon, DEVELOPMENT OF A MODEL FOR FLAMING COMBUSTION OF DOUBLE-WALL CORRUGATED CARDBOARD, Master's thesis, University of Maryland, Department of Fire Protection Engineering, 2012.
[74] L. Zhao, N.A. Dembsey, Measurement uncertainty analysis for calorimetry apparatuses, Fire Mater. 32 (2008) 1–26. https://doi.org/10.1002/fam.
[75] I.T. Leventon, K.T. Korver, S.I. Stoliarov, A generalized model of flame to surface heat feedback for laminar wall flames, Combust. Flame. 179 (2017) 338–353. https://doi.org/10.1016/j.combustflame.2017.02.007.
[76] M. Janssens, J. Huczek, A. Faw, Effect of specimen size on test results obtained in the cone calorimeter, Proc. 19th Annu. Conf. Recent Adv. Flame Retard. Polym. Mater. (2008) 343–353.
[77] B. Schartel, M. Bartholmai, U. Knoll, Some comments on the use of cone calorimeter data, Polym. Degrad. Stab. 88 (2005) 540–547. https://doi.org/10.1016/j.polymdegradstab.2004.12.016.
[78] K.C. Smyth, M.J. Houston, R.C. Dorfman, W.G. Mallard, R.J. Santoro, Smyth Methane Flame Characterization.pdf, Combust. Flame. 62 (1985).
[79] G.A. Marxman, Combustion in the turbulent boundary layer on a vaporizing surface, Symp. Combust. 10 (1965) 1337–1349. https://doi.org/10.1016/S0082-0784(65)80268-5.
[80] T. Ahmad, G.M. Faeth, Investigation of the Laminar Overfire Region Along Upright Surfaces., J. Heat Transfer. 100 (1978) 112–119. https://doi.org/10.1115/1.3450483.
[81] I.T. Leventon, PREDICTION OF UPWARD FLAME SPREAD OVER POLYMERS, Dissertation, University of Maryland, College Park, Department of Mechanical Engineering, 2015.

[82] I.T. Leventon, J. Li, S.I. Stoliarov, A flame spread simulation based on a comprehensive solid pyrolysis model coupled with a detailed empirical flame structure representation, Combust. Flame. 162 (2015) 3884–3895. https://doi.org/10.1016/j.combustflame.2015.07.025.
[83] I.T. Leventon, S.I. Stoliarov, Evolution of flame to surface heat flux during upward flame spread on poly(methyl methacrylate), Proc. Combust. Inst. 34 (2013) 2523–2530. https://doi.org/10.1016/j.proci.2012.06.051.
[84] W. Rosenow, J. Hartnett, Y. Cho, Handbook of Heat Transfer, in: 3rd ed., McGraw-Hill, New York, 1998: pp. 4.8-4.12, 4.16.
[85] T.L. Bergman, A.D. Lavine, F.P. Incropera, D.P. Dewitt, Fundamentals of Heat and Mass Transfer, John Wiley & Sons, Hoboken, 2011.
[86] B. Moghtaderi, B.Z. Dlugogorski, E.M. Kennedy, D.F. Fletcher, Effects of the Structural Properties of Solid Fuels on Their Re-ignition Characteristics, Fire Mater. 22 (1998) 155–165. https://doi.org/10.1002/(SICI)1099-1018(1998070)22:4<155::AID-FAM651>3.0.CO;2-F.
[87] R.E. Lyon, J.G. Quintiere, Criteria for piloted ignition of combustible solids, Combust. Flame. 151 (2007) 551–559. https://doi.org/10.1016/J.COMBUSTFLAME.2007.07.020.
[88] F.V. Lundström, P.B. Sunderland, J.G. Quintiere, P. van Hees, J.L. de Ris, Study of ignition and extinction of small-scale fires in experiments with an emulating gas burner, Fire Saf. J. 87 (2017) 18–24. https://doi.org/10.1016/j.firesaf.2016.11.003.
[89] Y. Ding, S.I. Stoliarov, R.H. Kraemer, Development of a semiglobal reaction mechanism for the thermal decomposition of a polymer containing reactive flame retardants: Application to glass-fiber-reinforced polybutylene terephthalate blended with aluminum diethyl phosphinate and melamine polypho, Polymers (Basel). 10 (2018) 1–14. https://doi.org/10.3390/polym10101137.
[90] H.R. Rakesh Ranga, O.P. Korobeinichev, A. Harish, V. Raghavan, A. Kumar, I.E. Gerasimov, M.B. Gonchikzhapov, A.G. Tereshchenko, S.A. Trubachev, A.G. Shmakov, Investigation of the structure and spread rate of flames over PMMA slabs, Appl. Therm. Eng. 130 (2018) 477–491. https://doi.org/10.1016/J.APPLTHERMALENG.2017.11.041.
[91] F. Raffan-Montoya, X. Ding, S.I. Stoliarov, R.H. Kraemer, Measurement of heat release in laminar diffusion flames fueled by controlled pyrolysis of milligram-sized solid samples: Impact of bromine- and phosphorus-based flame retardants, Combust. Flame. 162 (2015) 4660–4670.

https://doi.org/10.1016/J.COMBUSTFLAME.2015.09.031.
[92] U. Braun, H. Bahr, B. Schartel, Fire retardancy effect of aluminium phosphinate and melamine polyphosphate in glass fibre reinforced polyamide 6, E-Polymers. (2010) 1–14. https://doi.org/10.1515/epoly.2010.10.1.443.
[93] J.G. Quintiere, Fundamentals of Fire Phenomena, John Wiley & Sons, West Sussex, 2006.
[94] F. Goulay, P.E. Schrader, H.A. Michelsen, Effect of the wavelength dependence of the emissivity on inferred soot temperatures measured by spectrally resolved laser-induced incandescence, Appl. Phys. B Lasers Opt. 100 (2010) 655–663. https://doi.org/10.1007/s00340-010-4119-2.
[95] ASTM International, Standard Specification for Laboratory Burner Used for Small-Scale Burning Tests on, Annu. B. ASTM Stand. 08 (2015) 4–6. https://doi.org/10.1520/D5025-05.2.
[96] Y. Ding, M.B. McKinnon, S.I. Stoliarov, G. Fontaine, S. Bourbigot, Determination of kinetics and thermodynamics of thermal decomposition for polymers containing reactive flame retardants: Application to poly(lactic acid) blended with melamine and ammonium polyphosphate, Polym. Degrad. Stab. (2016). https://doi.org/10.1016/j.polymdegradstab.2016.05.014.
[97] K.C. Tsai, D. Drysdale, Flame height correlation and upward flame spread modelling, Fire Mater. 26 (2002) 279–287. https://doi.org/10.1002/fam.809.
[98] J. Quintiere, M. Harkleroad, Y. Hasemi, Wall flames and implications for upward flame spread, 1986. https://doi.org/10.1080/00102208608923893.
[99] J. Nakos, Uncertainty analysis of thermocouple measurements used in normal and abnormal thermal environment experiments at Sandia's Radiant Heat Facility and Lurance Canyon Burn Site, Sandia Natl. Lab. (2004). http://infoserve.sandia.gov/sand_doc/2004/041023.pdf.
[100] A.V. Singh, A FUNDAMENTAL STUDY OF BOUNDARY LAYER DIFFUSION FLAMES, Dissertation, University of Maryland, College Park, Department of Mechanical Engineering, 2015.
[101] K. Saito, F.A. Williams, A.S. Gordon, Structure of laminar coflow methane-air diffusion flames, J. Heat Transfer. 108 (1986) 640–648. https://doi.org/10.1115/1.3246984.
[102] B.K. Kandola, D. Price, G.J. Milnes, A. Da Silva, Development of a novel experimental technique for quantitative study of melt dripping of themoplastic polymers, Polym. Degrad. Stab. 98 (2013) 52–63. https://doi.org/10.1016/J.POLYMDEGRADSTAB.2012.10.028.
[103] W.A. Rosser, H. Wise, J. Miller, Mechanism of combustion inhibition by

compounds containing halogen, Symp. Combust. 7 (1958) 175–182. https://doi.org/10.1016/S0082-0784(58)80039-9.
[104] P. Gokulakrishnan, A.D. Lawrence, An experimental study of the inhibiting effect of chlorine in a fluidized bed combustor, Combust. Flame. 116 (1999) 640–652. https://doi.org/10.1016/S0010-2180(98)00057-1.
[105] S. Julien, C.M.H. Brereton, C.J. Lim, J.R. Grace, E.J. Anthony, The effect of halides on emissions from circulating fluidized bed combustion of fossil fuels, Fuel. 75 (1996) 1655–1663. https://doi.org/10.1016/S0016-2361(96)00135-4.
[106] M. Olek, J. Baron, W. Zukowski, Thermal decomposition of selected chlorinated hydrocarbons during gas combustion in fluidized bed, Chem. Cent. J. 7 (2013) 1–11. https://doi.org/10.1186/1752-153X-7-2.
[107] W.D. Chang, S.B. Karra, S.M. Senkan, A computational study of chlorine inhibition of CO flames, Combust. Flame. 69 (1987) 113–122. https://doi.org/10.1016/0010-2180(87)90024-1.
[108] G.J. Fiola, D.M. Chaudhari, S.I. Stoliarov, Comparison of Pyrolysis Properties of Extruded and Cast Poly (methyl methacrylate), Fire Saf. J. (2020) 103083. https://doi.org/10.1016/j.firesaf.2020.103083.
[109] G. Fiola, IMPROVING INVERSE ANALYSIS OF PYROLYSIS MODEL PARAMETERIZATION USING HILL CLIMBING ALGORITHMS, Master's thesis, University of Maryland, College Park, Department of Fire Protection Engineering, 2019.
[110] D.M. Chaudhari, G.J. Fiola, S.I. Stoliarov, Experimental analysis and modeling of Buoyancy-driven flame spread on cast poly(methyl methacrylate) in corner configuration, Polym. Degrad. Stab. 183 (2021) 109433. https://doi.org/10.1016/j.polymdegradstab.2020.109433.
[111] S. Vyazovkin, C.A. Wight, Kinetics in Solids, Annu. Rev. Phys. Chem. 48 (1997) 125–149. https://doi.org/10.1146/annurev.physchem.48.1.125.
[112] A.K. Galwey, M.E. Brown, Arrhenius parameters and compensation behaviour in solid-state decompositions, Thermochim. Acta. 300 (1997) 107–115. https://doi.org/10.1016/S0040-6031(96)03120-6.
[113] J.D. Peterson, S. Vyazovkin, C.A. Wight, Kinetic Study of Stabilizing Effect of Oxygen on Thermal Degradation of Poly(methyl methacrylate), J. Phys. Chem. B. 103 (1999) 8087–8092. https://doi.org/10.1021/jp991582d.
[114] J.P. Holman, Heat Transfer, 9th ed., McGraw-Hill, New York, 2002.
[115] J.D. Swann, Y. Ding, M.B. McKinnon, S.I. Stoliarov, Controlled atmosphere pyrolysis apparatus II (CAPA II): A new tool for analysis of pyrolysis of charring and intumescent polymers, Fire Saf. J. 91 (2017) 130–139.

https://doi.org/10.1016/j.firesaf.2017.03.038.
[116] C.G. McCoy, J.L. Tilles, S.I. Stoliarov, Empirical Model of flame heat feedback for simulation of cone calorimetry, Fire Saf. J. 103 (2019) 38–48. https://doi.org/10.1016/J.FIRESAF.2018.11.006.
[117] C.R. Shaddix, Correcting thermocouple measurements for radiation loss: A critical review, Proc. 33rd Natl. Heat Transf. Conf. (1999) HTD99-282. http://stacks.iop.org/0957-0233/17/i=4/a=008?key=crossref.c1c3cfeacea9050e5890fc9d71a73053.
[118] D.C. Collis, M.J. Williams, Two-dimensional convection from heated wires at low Reynolds numbers (D.C.Collis, M.J.Williams,1959).pdf, J. Fluid Mech. 6 (1959) 357–384.
[119] S.R. Turns, An Introduction to Combustion: Concepts and Applications, in: An Introd. to Combust. Concepts Appl., 3rd ed., McGraw-Hill, New York, 2012: pp. 338–339.
[120] L.M. Jakob, Heat Transfer: Vol. 1, Wiley, 1967.
[121] R.E. Lyon, R.N. Walters, S.I. Stoliarov, Thermal analysis of flammability, J. Therm. Anal. Calorim. 89 (2007) 441–448. https://doi.org/10.1007/s10973-006-8257-z.